2015

Scanning Probe Investigations of Nanopatterned and Thermo-responsive Polypeptoids and the Design of a Sample Stage for Force Modulation Microscopy

Lu Lu
Louisiana State University and Agricultural and Mechanical College, llu6@lsu.edu

SCANNING PROBE INVESTIGATIONS OF NANOPATTERNED AND THERMO-RESPONSIVE POLYPEPTOIDS AND THE DESIGN OF A SAMPLE STAGE FOR FORCE MODULATION MICROSCOPY

A Dissertation

Submitted to the Graduate Faculty of the
Louisiana State University and
Agricultural and Mechanical College
in partial fulfillment of the
requirements for the degree of
Doctor of Philosophy

in

The Department of Chemistry

by
Lu Lu
B.S., University of Science and Technology of China, 2010
August 2015

ACKNOWLEDGEMENTS

I would like to express my thanks to my two advisors, Dr. Jayne C. Garno and Dr. Donghui Zhang, for their guidance and support during my Ph.D career at Louisiana State University. I want to thank my committee members Dr. Bin Chen, Dr. Francisco Hung, and Dr. Graca Vicente for reviewing my dissertation and providing valuable feedback.

I would like to thank Dr. Song Xu from Keysight Technologies for collaboration and helpful discussion.

I also thank both past and current members of the Garno and Zhang groups, for the great times we had together for the past five years.

Lastly, I want to express my deepest appreciation to my parents, my sister and my husband for their support and love.

TABLE OF CONTENTS

ACKNOWLEDGEMENTS ii

LIST OF ABBREVIATIONS vi

ABSTRACT viii

CHAPTER 1. INTRODUCTION 1
1.1 Nanoscale Surface Studies with Atomic Force Microscopy 1
1.2 Surface Patterning of Polypeptoids Using Particle Lithography 1
1.3 *In Situ* Studies of the Thermo-Responsiveness of Polypeptoid Nanopillars 2
1.4 Review of Previous Studies with Force Modulation Microscopy 3
1.5 A Force Modulation Sample Stage for Scan-by-Tip AFM 3
1.6 Stage-Driven Force Modulation Microscopy versus Tip-Driven Indirect Magnetic Modulation 4
1.7 Conclusions and Future Prospectus 4

CHAPTER 2. EXPERIMENTAL DESIGNS WITH SCANNING PROBE MICROSCOPY 5
2.1 Background and Imaging Principle of Atomic Force Microscopy 5
2.2 Contact-mode and Lateral Force Imaging 6
2.3 AFM Force Spectroscopy 9
2.4 Tapping-mode AFM and Phase Imaging 10
2.5 Force Modulation Microscopy 13
2.6 *In Situ* Temperature Studies Using AFM 16
2.7 AFM imaging Modes Used in the Dissertation 16

CHAPTER 3. DIRECTED GROWTH OF POLYMER NANOPILLARS USING SURFACE-INITIATED RING-OPENING POLYMERIZATION OF *N*-ALLYL *N*-CARBOXYANHYDRIDE 18
3.1 Introduction 18
3.2 Experimental Section 21
3.2.1 Materials and Reagents 21
3.2.2 Atomic Force Microscopy 21
3.2.3 Preparation of Nanopores within an OTS Film 21
3.2.4 Preparation of APTES Nanodots 22
3.2.5 Three Steps Synthesis of Allyl-NCA 22
3.2.6 Polymerization of Allyl-NCA. 24
3.3 Results and Discussion 24
3.4 Conclusion 32

CHAPTER 4. THERMO-RESPONSIVE BEHAVIOR OF LINEAR COPOLYPEPTOID NANOSTRUCTURES INVESTIGATED WITH ATOMIC FORCE MICROSCOPY 33
4.1 Introduction 33
4.2 Experimental Section 35
4.2.1 Preparation of Nanopatterned UTS Sites 35
4.2.2 Synthesis of Linear poly[(*N*-ethyl glycine)$_{32}$-*r*-(*N*-butyl glycine)$_{17}$] Copolymer 35

4.2.3 Preparation Nanopatterned Poly[(*N*-ethyl glycine)$_{32}$-*r*-(*N*-butyl glycine)$_{17}$] by Surface Thiol-ene Click Reaction 36
4.2.4 Thermoresponsive Study of Nanopatterned Copolypeptoids using *in situ* AFM 36
4.3 Result and Discussion 37
4.4 Conclusion 43

CHAPTER 5. A REVIEW ON FORCE MODULATION MICROSCOPY AND THE CAPABILITY OF NANOMECHANICAL MAPPING OF SURFACE ELASTIC AND VISCOELASTIC PROPERTIES 44
5.1 History of Force Modulation Microscopy (FMM) 44
5.2 Instrument Set-up of FMM 45
5.3 Advantages of FMM 47
5.4 Studying Self-assembled Monolayers (SAMs) Using FMM 49
5.5 Investigating Polymeric Materials Using FMM 53
5.6 Probing Biological and Inorganic Samples Using FMM 57
5.7 Conclusions 59

CHAPTER 6. SAMPLE STAGE DESIGNED FOR FORCE MODULATION MICROSCOPY USING A TIP-MOUNTED AFM SCANNER 60
6.1 Introduction 60
6.2 Experimental Section 61
6.2.1 Materials and Reagents 61
6.2.2 Atomic Force Microscopy 62
6.3 Results and Discussion 62
6.3.1 Design of the FMM Sample Stage 62
6.3.2 Characterization of Nanopatterns within an OTS Film using the FMM Sample Stage. 64
6.3.3 FMM Characterization of Nanorings of PEG-silane 67
6.3.4 Characterization of a Cyclic Gel Sample with FMM 69
6.4 Conclusions 72

CHAPTER 7: DIRECT COMPARISON OF SAMPLE ACTUATION VERSUS TIP VIBRATION CONFIGURATION FOR FORCE MODULATION AFM 73
7.1 Introduction 73
7.2 Experiment Section 74
7.2.1 Materials and Reagents 74
7.2.2 Atomic Force Microscopy 75
7.2.3 Preparation of CMPS Nanorings 75
7.2.4 Characterization of CMPS Nanorings with Stage-driven FMM. 76
7.2.5 Characterization of CMPS Nanorings with Tip-driven IMM 77
7.3 Results 77
7.3.1 Nanorings of CMPS Studied with FMM and IMM with and without Sample/Tip Modulation 77
7.3.2 Nanorings of CMPS Studied with FMM at Selected Driving Frequencies 80
7.3.3 Nanorings of CMPS Studied with IMM at Selected Driving Frequencies 80
7.3.4 High Resolution Stage-driven FMM and Tip-driven IMM Images of CMPS Nanorings 83

7.3.5 Frequency Sweeps of FMM at Selected Regions of the Sample Surface 85
7.3.6 Frequency Sweeps of IMM at Selected Regions of the Sample Surface 86
7.3.7 Dynamic Stage-driven FMM and Tip-driven IMM Studies..... 87
7.3.8 Side-by-side Comparison of FMM and IMM at the Same Driving Frequencies. 89
7.4 Discussion 91
7.5 Conclusion..... 92

CHAPTER 8. CONCLUSIONS AND FUTURE PROSPECTUS 93

REFERENCES 95

APPENDIX A: PROCEDURE FOR FORCE MODULATION MICROSCOPY (FMM) USING NEWLY-DESIGNED SAMPLE STAGE..... 114

APPENDIX B: PROCEDURE FOR TEMPERATURE STUDIES USING THE HEATING STAGE WITH KEYSIGHT 5500 OR 5420..... 117

APPENDIX C: SUPPLEMENTAL INFORMATION FOR THERMO-RESPONSIVE BEHAVIOR OF LINEAR COPOLYPEPTOID NANOSTRUCTURES INVESTIGATED WITH ATOMIC FORCE MICROSCOPY 119

APPENDIX D: SUPPLEMENTAL INFORMATION FOR SAMPLE STAGE DESIGNED FOR FORCE MODULATION MICROSCOPY USING A TIP-MOUNTED AFM SCANNER 124

APPENDIX E: SUPPLEMENTAL INFORMATION FOR DIRECT COMPARISON OF SAMPLE ACTUATION VERSUS TIP VIBRATION CONFIGURATION FOR FORCE MODULATION AFM..... 127

APPENDIX F: IMAGING POLYSTYRENE LATEX MESOSPHERES USING AFM 133

APPENDIX F: PERMISSIONS 134

VITA 138

LIST OF ABBREVIATIONS

ABBREVIATION	NAME
AFM	Atomic force microscopy
OTS	Octadecyltrichlorosilane
APTES	(3-Aminopropyl)triethoxysilane
P(NEG_{32}-*r*-NBG_{17})	Poly[(*N*-ethyl glycine)$_{32}$-*r*-(*N*-butyl glycine)$_{17}$]
UTS	10-Undecenyltrichlorosilane
FMM	Force modulation microscopy
FM-AFM	Force modulation atomic force microscopy
CMPS	4-(Chloromethyl)phenyltrichlorosilane
IMM	Indirect magnetic modulation
TMMH	1,1,1-Tris(mercaptomethyl)heptadecane
SAMs	Self-assembled monolayers
Allyl-NCA	*N*-allyl *N*-carboxyanhydride
PBLG	Poly (γ-benzyl-*L*-glutamate)
PMLG	Poly(γ-methyl *L*-glutamate)
PLGA	Poly(*L*-glutamic acid)
PLL	Poly(*L*-lysine)
PEG-silane	2-[Methoxy(polyethyleneoxy)propyl] trichlorosilane
CD	Circular dichroism
SI-ATRP	Surface-initiated atom transfer radical polymerization
PNIPAAm	Poly(*N*-isopropyl acrylamide)

LCST	Lower critical solution temperature
CuAAC	Copper (I) catalyzed azide-alkyne cycloaddition
LB	Langmuir-Blodgett
FOETS	(Perfluorooctyl)ethyl]trichlorosilane
DMPC	Dimyristoylphosphatidylcholine
QP	Quercetin palmitate
OTE	Octadecyltriethoxysilane
DPDA	Diamino-diethyl-ene glycol-pentacosadiynoic acid
PS	Polystyrene
PVME	Poly(vinyl methyl ether)
PP	Polypropylene
EP	Ethylene propylene
PEO	Polyethyleneoxide
PDMS	Poly(dimethylsiloxane)
P2VP	Poly-2-vinylpyridin
PtBMA	Polytertbutylmethacrylate
c-PNMG$_{100}$-*b*-PNDG$_{10}$	Poly(*N*-methyl glycine)$_{100}$-*b*-poly(*N*-decyl glycine)$_{10}$
SPM	Scanning probe microscopy

ABSTRACT

Protocols for patterning nanostructures of polymers were developed to enable scanning probe microscopy (SPM) studies of surface properties at the molecular level. A chemically selective surface for patterning polymers was generated by combining particle lithography with organosilane immersion. Poly(*N*-allyl glycine), a biocompatible and backbone degradable polypeptoid, was grown on Si(111) at confined amine sites using surface-initiated polymerization (also known as the "graft from" approach). A thermo-responsive random copolypeptoid, poly[(*N*-ethyl glycine)$_{32}$-*r*-(*N*-butyl glycine$_{17}$)], was pre-synthesized and attached onto a patterned organosilane surface using a thiol-ene click reaction ("graft to" approach). The phase transitions of the copolypeptoid nanostructures in an aqueous environment was studied using *in situ* atomic force microscopy (AFM). A heated stage was used to heat the nanopatterned sample in liquid media.

Force modulation microscopy (FMM), one of over 50 possible modes of SPM, is used to acquire mechanical properties of samples concurrent with topographic information. The history, instrument set-up, advantages, and applications with self-assembled monolayers, polymers, biological and inorganic samples are reviewed in this dissertation. The sample is placed directly on an xyz scanner for the most common FMM configuration. Most commercial SPM systems are designed to have the tip mounted on the piezotube scanner. To facilitate FMM with tip-mounted scanners, a sample stage was designed and constructed of machined polycarbonate. A piezoactuator in the sample stage was used to drive the vibration of the sample in the z-direction at selected frequency and amplitude. The sample stage was evaluated by studying three samples with increasing complexity. This sample-driven FMM was compared with indirect magnetic modulation (IMM), an alternate way to accomplish force modulation studies by modulating the nosecone assembly. A test platform of patterned nanoring samples was evaluated to systematically

compare FMM and IMM. Both methods can be used to sensitively acquire high resolution images of sample elasticity. However, the newly designed sample stage for FMM is easier to operate compared with IMM.

CHAPTER 1. INTRODUCTION

Protocols have been developed in this dissertation for studies of polymerization reaction mechanisms at the molecular level using a surface test platform of patterned polymer nanopillars. Several imaging modes of atomic force microscopy (AFM) were selected or developed to investigate systems of interest. A prototype sample stage accessory for AFM was designed and evaluated to enable advanced measurements with force modulation microscopy.

1.1 Nanoscale Surface Studies with Atomic Force Microscopy

Since the invention of AFM in 1986,[1] new studies have been advanced for surface analysis in fields such as biology,[2-4] polymers,[5-7] molecular electronics[8] and medical diagnostics.[9-10] The resolution of AFM imaging is not limited by the wavelength of light. With an ultra-sharp probe, the topographic resolution of AFM can achieve 0.1 nm for the x and y directions and 0.01 nm for the z direction.[11-13] More than 50 AFM modes have been developed for imaging and for measuring forces. The background and imaging principle of scanning probe microscopy and the AFM modes used for this dissertation are summarized in Chapter 2, including contact-mode, lateral force imaging, tapping-mode, phase imaging, force modulation microscopy, and indirect magnetic modulation. Characterizations using AFM force spectroscopy and *in situ* temperature studies with a heating stage will also be described.

1.2 Surface Patterning of Polypeptoids Using Particle Lithography

Arrays of polymer nanostructures were prepared on Si(111) using a stepwise chemistry route combined with particle lithography. In the first step, nanopores were prepared within a thin film of a self-assembled monolayer of octadecyltrichlorosilane (OTS). The film of OTS served as a surface resist and the areas of nanopores provided sites for further reactions. The initiator, (3-aminopropyl)triethoxysilane (APTES) was grown selectively inside the nanopores to define surface sites for polymerization reaction to proceed. Surface-initiated ring-opening polymerization

of *N*-allyl *N*-carboxyanhydride with APTES formed polymer pillars on the nanopatterns of APTES, which terminated with amine functional groups. The surface changes for each step were monitored using AFM. Slight variations in the height of the poly(*N*-allyl glycine) pillars were observed which scale correspondingly to the initial dimensions of nanopores. The distance between polymer nanopillars is controlled by the size of mesoparticle masks. This platform has potential application in biotechnology as smart coatings, biosensors or bioseparations based on the biocompatibility, backbone biodegradability and processability of poly(*N*-allyl glycine). In Chapter 3, the strategy of surface patterning of polypeptoids at the nanoscale and the surface characterizations of each step will be presented.

1.3 *In Situ* Studies of the Thermo-Responsiveness of Polypeptoid Nanopillars

Nanoscale surface test platforms were used to investigate the phase transitions of thermo-responsive copolymer nanostructures with AFM. A clear aqueous solution of the random copolymer poly[(*N*-ethyl glycine)$_{32}$-*r*-(*N*-butyl glycine)$_{17}$], abbreviated as P(NEG$_{32}$-*r*-NBG$_{17}$), becomes turbid upon heating, and upon cooling returns to a clear appearance. The clarity of the P(NEG$_{32}$-*r*-NBG$_{17}$) solution indicates a response to temperature that is attributable to reversible polymeric phase transitions. For studies with AFM, nanopores on Si(111) within a film of octadecyltrichlorosilane (OTS) were prepared using particle lithography combined with steps of solution immersion. A second silane, 10-undecenyltrichlorosilane (UTS), was backfilled into the exposed nanopores to form ultra-small surface reactive sites for site-selective polymer deposition and growth. The random copolymer P(NEG$_{32}$-*r*-NBG$_{17}$) was anchored to reactive sites of UTS nanodots to produce patterned polymer pillars. The morphology and surface arrangement of polymer nanopillars were characterized at each step using high resolution AFM. Studies of thermo-responsive properties were developed to accomplish dynamic protocols in liquid media. A temperature stage was used to heat the sample during time-lapse AFM imaging. To the best of our

knowledge this is the first report using scanning probe studies to characterize the thermo-responsive properties of patterned polymer pillars as detailed in Chapter 4. Significant advantages are gained by localizing and patterning polymer pillars on surfaces to enable direct visualization of surface changes via AFM studies of thermo-responsive properties.

1.4 Review of Previous Studies with Force Modulation Microscopy

A review of force modulation microscopy (FMM) and the capabilities for nanomechanical mapping of surface elastic and viscoelastic properties is presented in Chapter 5. Force modulation microscopy was invented in 1991 by Maivald and Hansma et al.[14] With FMM, local mechanical properties of a sample can be acquired along with topographic information. Vibration is applied to the z axis at the tip-sample contact during contact-mode imaging. A contemporary review of instrumental configurations for FMM and applications with self-assembled monolayers, polymers, inorganic materials and biological samples is presented.

1.5 A Force Modulation Sample Stage for Scan-by-Tip AFM

Among the modes of scanning probe microscopy that have been developed, FMM is commonly used to acquire mechanical properties of samples along with topographic information. The FMM mode is particularly useful for investigations with polymer samples and organic thin films. We have designed and tested a sample stage for FMM constructed of machined polycarbonate. The generic design enables FMM measurements for instrument configurations with a tip-mounted AFM scanner. A piezoactuator is embedded within the sample stage to drive the sample to vibrate in the z-direction according to selected parameters of alternating current. The invention of the sample stage and applications using three samples is presented in Chapter 6.[15]

1.6 Stage-Driven Force Modulation Microscopy versus Tip-Driven Indirect Magnetic Modulation

We have designed and tested a sample stage for force modulation microscopy (FMM) that is applicable for AFM instruments that are configured with a tip-mounted scanner configuration. A piezoactuator within the stage is used to precisely modulate the sample for FMM characterizations. Another AFM mode developed for tip-mounted scanners known as indirect magnetic modulation (IMM), was previously reported by our group.[16] For IMM, an AC electromagnetic field is applied to the nosecone tip holder assembly from a solenoid underneath the sample. The entire tip holder assembly is driven to vibrate to produce modulation of the tip-sample contact. In Chapter 7, a test platform of 4-(chloromethyl)phenyltrichlorosilane (CMPS) nanoring patterns were prepared with particle lithography combined with heated vapor deposition. The test structures provide a model surface to compare the two AFM imaging modes: FMM and IMM. A series of frequencies were used for FMM and IMM to investigate the frequency-dependent properties of the sample. Frequency sweeps at selected regions of the sample were obtained to evaluate the local differences in elastic response for the nanostructures.

1.7 Conclusions and Future Prospectus

Protocols based on particle lithography have been developed to prepare spatial selective surfaces of polypeptoids. The thermo-responsive properties of nanopatterned polypeptoids was studied using dynamic protocols and liquid imaging media. A prototype sample stage was built and tested for force modulation microcopy. In Chapter 8, the main results of this dissertation are presented along with a discussion of future directions.

CHAPTER 2. EXPERIMENTAL DESIGNS WITH SCANNING PROBE MICROSCOPY

Protocols were developed in this dissertation for characterizing nanostructures of organic thin films and polymers using selected modes of scanning probe microscopy (SPM). A key strategy was to create unique surface test platforms of exquisitely uniform nanopatterns or organosilanes and polymers. Several imaging modes were selected or developed for the investigations of this dissertation. A prototype sample stage for force modulation microscopy (FMM) was designed and evaluated to enable advanced measurements with tip-mounted AFM scanner configurations.

2.1 Background and Imaging Principle of Atomic Force Microscopy

Atomic force microscopy (AFM) was invented in 1986 by Binnig, Quate, and Gerber and has become a powerful tool for surface analysis.[1] New capabilities for acquiring surface morphology with molecular and atomic resolution can be routinely achieved with AFM when using a sharp probe. By monitoring the interactions between the probe and samples, surfaces properties such as friction, viscoelasticity, conductivity, and magnetism can be recorded with digital images.[17-20]

An advantage of AFM is that the images can be acquired in air, vacuum and liquid environments, which enables dynamic studies of *in situ* time-lapse reactions.[21-22] Samples for AFM characterization do not need to be coated with a conductive metal layer for imaging in vacuum as with electron microscopy. The sample must be relatively flat (usually z scale less than 1 μm for best resolution) to be suitable for AFM studies. Diverse samples can be characterized with AFM, such as self-assembled monolayers,[23-24] polymers,[25-26] nanoparticles,[27-28] proteins,[29-30] cells,[31-32] and DNA.[33-34] The resolution achieved with AFM reaches 0.1 nm for the x and y directions using an ultra-sharp probe and 0.01 nm for the z direction.[11-13]

Commonly used AFM tips are made of silicon or silicon nitride, which are attached to either a V-shaped or rectangular cantilever. The backside of the cantilevers are coated with

reflective materials such as gold. A diode laser is positioned onto the back of a cantilever and reflected to the center of a position-sensitive four-quadrant photodiode detector. Changes of the cantilever deflection and oscillation amplitude are monitored by the photodetector and are maintained at an assigned setpoint through an electronic feedback loop. Images of surfaces are constructed by recording the topography and tip-sample interaction as a function of tip position. A topograph of the sample can be acquired with AFM. Additional information such as frictional, viscoelastic, magnetic and conducting properties can be simultaneously acquired with topographs.

More than 50 AFM modes have been developed during the past 30 years and the imaging modes can be categorized by how the AFM tip is operated relative to the sample: contact, non-contact and intermittent-contact. For contact-mode AFM, the tip is placed in continuous contact with surface. For non-contact-mode, the tip is maintained at a discrete distance from the sample to measure forces (e.g. electrostatic, van der Waal's, magnetic) within a specific distance from the surface. With intermittent-contact-mode, also known as tapping-mode AFM, the tip is driven to oscillate at or near its resonant frequency and "taps" the surface during scans. Contact-mode and tapping-mode are the most common modes of AFM, and are used in this dissertation. Other modes to be introduced in this Chapter are AFM force spectroscopy, force modulation microscopy, and *in situ* temperature studies using AFM.

2.2 Contact-mode and Lateral Force Imaging

Contact-mode is widely used in the field of surface analysis. The first contact-mode image was published in 1986 when Binnig et al. invented AFM, showing line traces on a ceramic (Al_2O_3) sample.[1] Atomic resolution of a graphite surface was achieved in 1987 by Binnig et al. shortly after the invention of AFM.[13]

During contact-mode imaging, a sharp probe is scanned in a raster pattern across the surface using a piezoelectric scanner (Figure 2.1). The probe is attached to the end of the cantilever

and has a radius of ~10 nm. The deflection changes of the cantilever due to the changes in tip-sample interaction are monitored with a photodetector. The force between the tip and sample is maintained at a constant setting by a feedback loop, which can be precisely controlled by applying voltage to the scanner. Changes in cantilever deflection due to sample topography will lead to vertical movement of the laser spot on the photodetector. Changes in torsional twisting of the cantilever due to sample frictional force will influence lateral placement of the laser spot on the photodetector. The photodetector is used to sensitively track the movement of the laser spot and translate the electrical signal to digital AFM images as shown in Figure 2.1.

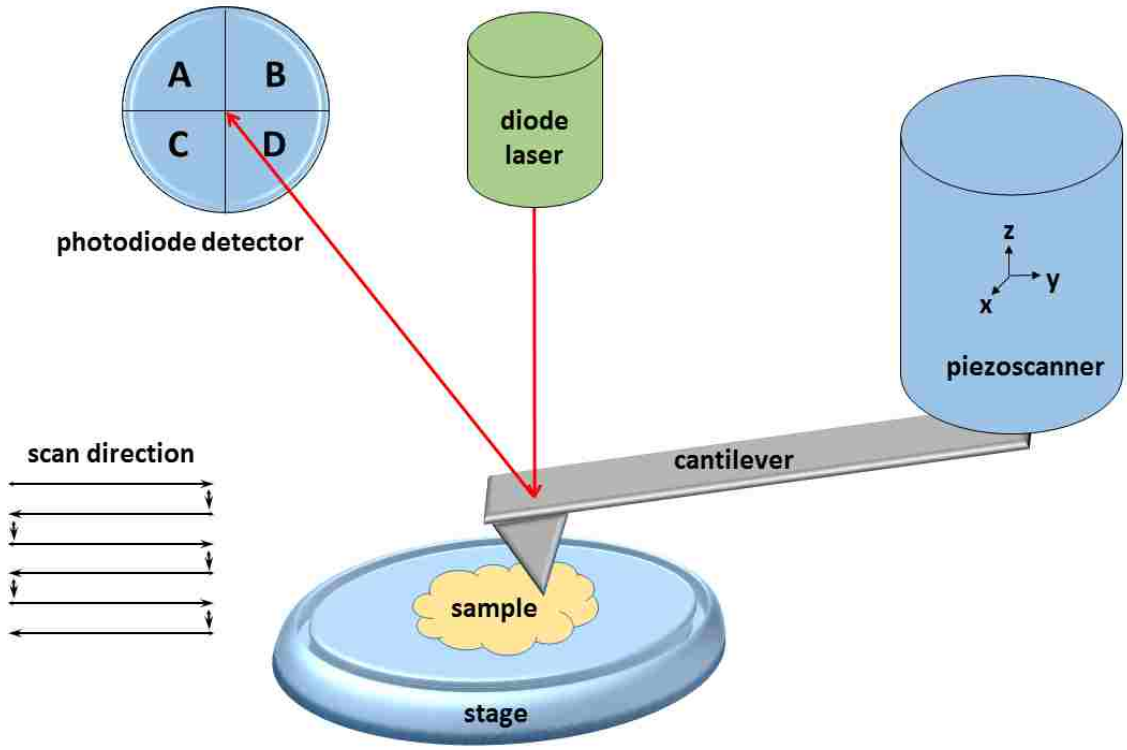

Figure 2.1 Operating principle of contact-mode AFM.

Three types of AFM images can be generated concurrently with contact-mode AFM: topography, deflection and lateral force images. Topography images are height traces of the surface and give a 3D profile of the surface morphology. The topography frames are generated

from plotting the scanner z piezo voltage adjustments of the feedback loop. Deflection images show the error signal associated with the feedback loop. The deflection signal (error signal) is small when parameters during imaging are optimized, therefore the deflection images are usually not reported in the literature. As the tip is scanned across and interacts with the sample, frictional force will cause lateral twisting of the tip. The lateral movement of the laser spot on the photodetector is used to generate lateral force images. The lateral force images are used to distinguish the differences in chemistry at the interface.

An example of contact-mode imaging is shown in Figure 2.2. Gold terraces and step edges under a monolayer of 1,1,1-tris(mercaptomethyl)heptadecane (TMMH) are apparent in the topography frame (Figure 2.2a). Nanopores with a depth of ~0.6 nm can vaguely be distinguished in the topograph, however, in either the trace or retrace of the lateral force images, differences between the methyl terminal group of TMMH and the circular spots of bare gold substrate are clearly revealed. Interestingly, the contrast is reversed between the trace and retrace images. The nanopores are shown as bright spots with a darker color for the TMMH layer in the trace image

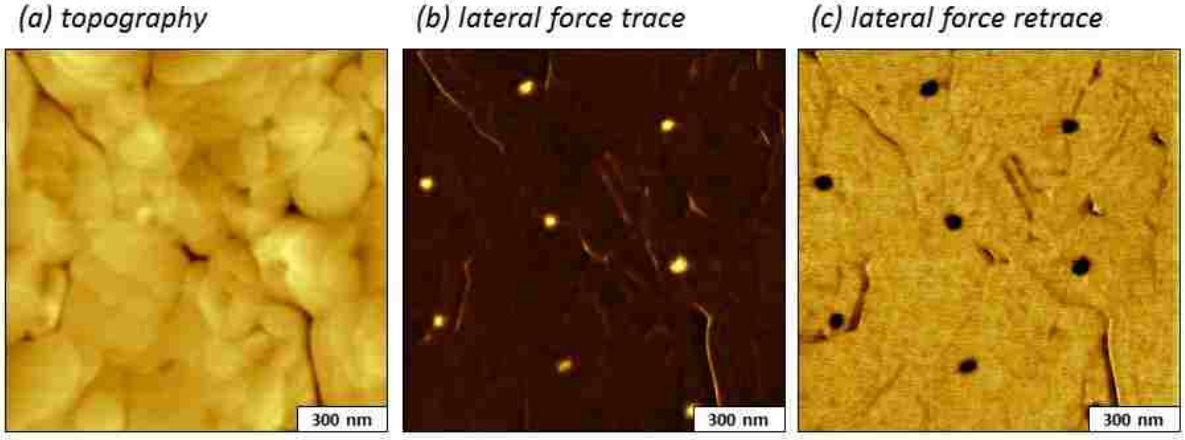

Figure 2.2 Nanopores within a thin film of 1,1,1-tris(mercaptomethyl)heptadecane on Au(111) are viewed in the topograph (a), lateral force trace (b), and lateral force retrace (c) images acquired using contact-mode AFM.

(Figure 2.2b); whereas the nanopores are dark with brighter areas for TMMH in the retrace image (Figure 2.2c). As the tip scans the surface in opposite directions the probe interacts with the surface differently to produce a reversion in contrast between trace and retrace images of lateral force channel.[35]

2.3 AFM Force Spectroscopy

Quantitative measurements of interactions between the tip and sample can be achieved with AFM force spectroscopy to generate force-distance curves. [36-39] Force spectroscopy has been applied for probing the kinetics of chemical reactions on surfaces,[40] for studies of the glass-to-rubber transition of amorphous polymers, the elastic-plastic properties as a function of temperature,[41-42] adhesion,[43] and time-dependent elastic response of polymers.[44] A force-distance curve is a plot of cantilever deflection as a function of tip position in the z direction of an approach-retract cycle. Forces between the tip and sample can be calculated by Hooke's Law (Equation 2.1).

$$F = -kx \qquad \text{Equation } 2.1$$

For this relation, F is the force applied to the tip from the sample, k is the spring constant of the cantilever, and the x is the cantilever deflection.

Based on Hooke's Law, the force sensed by the probe is proportional with the tip displacement, which can also be viewed in the example of a force-distance curve (Figure 2.3) acquired in air for nanopatterns of octadecyltrichlorosilane on Si(111). In region I, the tip is far away from the sample and no force is present between the tip and sample, thus there is no cantilever deflection. As the tip is brought closer to the surface, attractive forces (such as Van der Waals or electrostatic forces) cause the tip to "snap into contact" with the sample (region II). In region III, the tip is placed in contact with the sample in the repulsive force region. The increase in force causes the tip to bend. When reaching the set maximum force (maximum bending), the retract cycle begins (region IV). Adhesion in region V maintains contact of the tip and sample. When the

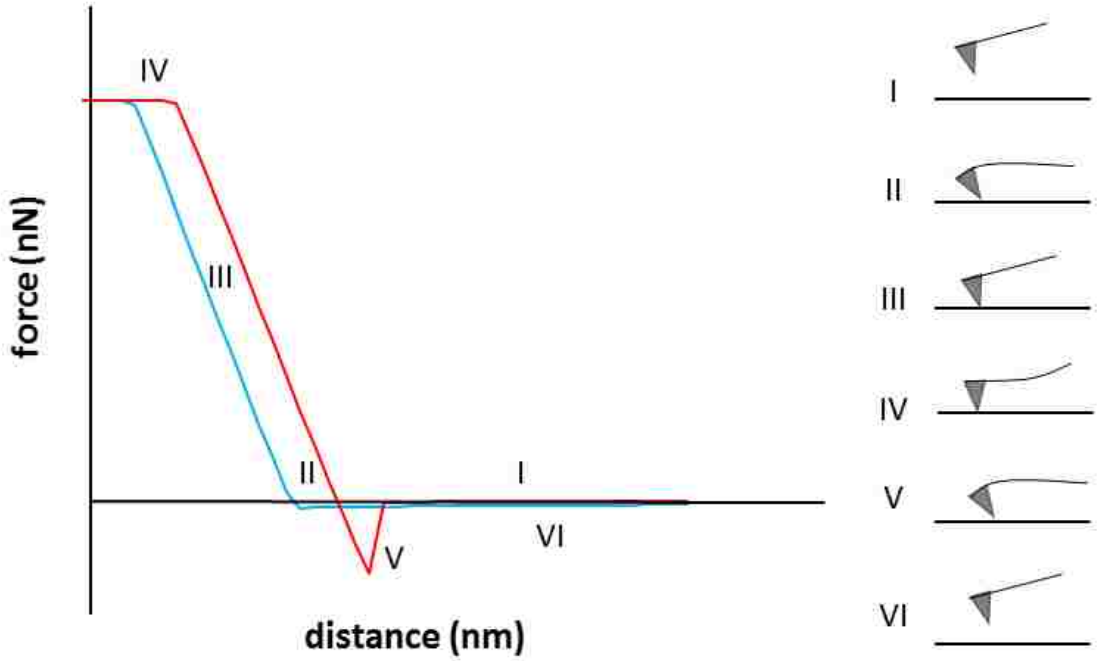

Figure 2.3 Force-distance curves acquired in air with Si_3N_4 tip for a sample of nanopore patterns on Si(111): approach (blue) and retract (red) cycle.

distance between the tip and sample is large enough, the tip will "snap out of contact" and return to zero deflection (region VI).

2.4 Tapping-mode AFM and Phase Imaging

Lateral, adhesive and shear forces may displace loosely bound molecules or damage soft samples on surfaces such as nanoparticles,[45] polymers,[7, 46-48] and proteins.[49-50] Tapping-mode AFM was developed to minimize damage to the sample caused by shear forces.[51-53] During tapping-mode imaging the AFM probe is operated to gently "tap" the surface. The probe is driven to oscillate by a piezoceramic element at or near the resonance frequency (150-400 kHz). Tapping-mode tips are stiffer than probes used for contact-mode imaging, with spring constants in the range of 10-50 N/m. The oscillation amplitude of the tips for tapping-mode is around 50-100 nm, which is adequate to overcome adhesion between the tip and sample. The tip is mounted on a scanner (Figure 2.4). To induce vibration of the tip, AC voltage is applied to a piezoactuator inside the tip

holder assembly. The amplitude of free oscillation in air will be dampened when the tip encounters the sample. A feedback loop maintains a constant amplitude at a designated setpoint value. The difference between the output or measured amplitude with the amplitude setpoint value is the error signal for tapping-mode imaging. The error signal is used to calculate how much voltage is needed to maintain a constant amplitude within the feedback loop. Changes in the voltage to maintain a constant amplitude are translated to generate digital topography images.

Phase images provide additional information and can be acquired concurrently with tapping-mode topography frames. Differences in the phase angle between the driving AC input signal and the output tip vibration, also called the phase lag (Figure 2.4), are measured by a lock-in amplifier and translated into phase images. Information of local adhesion, viscoelasticity and contact area slope between tip and sample can be sensitively mapped with phase images.[54-55]

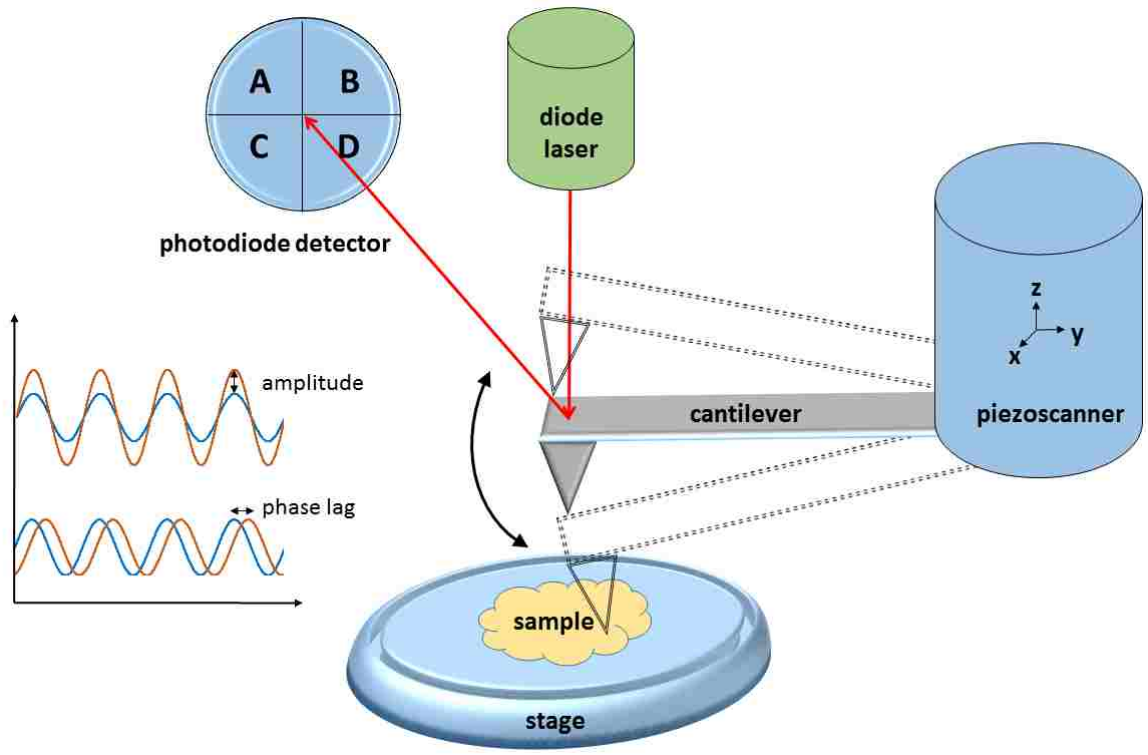

Figure 2.4 Operating principle of tapping-mode AFM.

An example of tapping-mode topography and phase images is shown in Figure 2.5 for a sample of patterned nanorings of *N*-(6-aminohexyl)aminopropyltrimethoxysilane prepared using particle lithography with chemical vapor deposition.[56] The surface morphology and a height profile of the nanoring sample are presented in the topography channel, where brighter contrast indicates the taller structures on surface (surface z scale: 5.7 nm). The difference in color contrast among the ring, the center areas of the ring, and the surrounding matrix areas shown in the phase images indicate changes in elastic response for different regions of the sample. The small particles between the rings can be clearly resolved in the phase image.

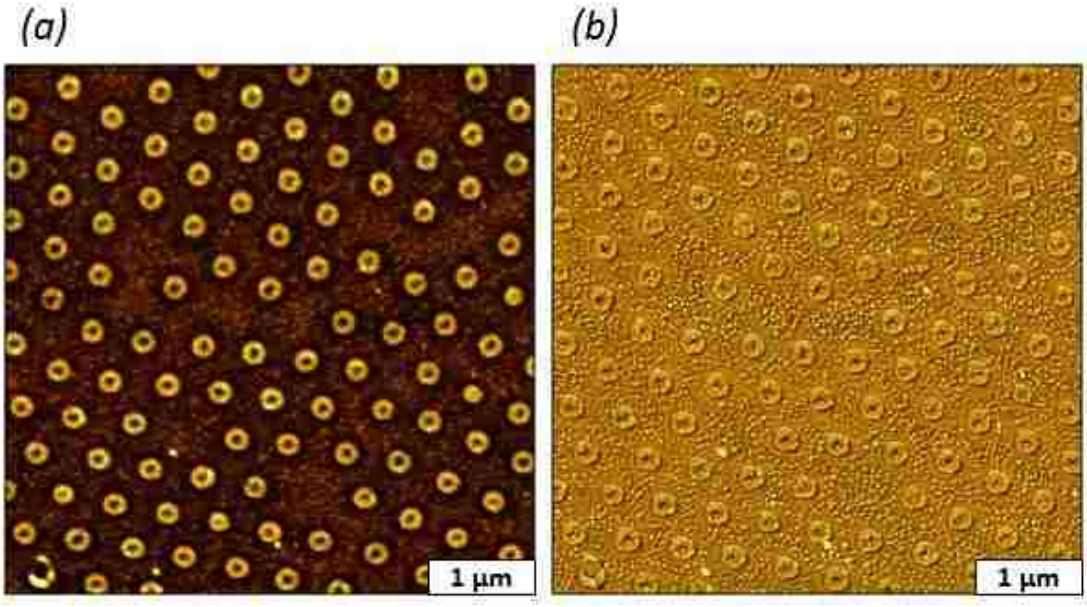

Figure 2.5 Nanorings of *N*-(6-aminohexyl)aminopropyltrimethoxysilane imaged with tapping-mode AFM. (a) Topography and (b) phase images.

Tapping-mode is particularly suitable for polymer samples which have viscoelastic properties. Phase images can elucidate fine details of the sample that topography cannot provide, especially for phase separated system such as polymer blends of polystyrene and polybutadiene,[57] lamellae structure of block copolymer polystyrene-*b*-polymethylmethacrylate,[58] and segmented

polyether polyurethane.[59] An example of tapping-mode imaging of polymeric materials is presented in Figure 2.6 for a bottlebrush copolypeptoid, norbornenyl-terminated poly(*N*-ethyl glycine)$_{36}$-*r*-poly(*N*-butyl glycine)$_{12}$ copolymers. The sizes and shapes of the bottlebrush polymer were studied with tapping-mode AFM. Discrete nanosized particles are viewed in the topograph and corresponding phase image. The differences in the shapes are attributed to the orientation and twisting of the polymer backbone or aggregation of several polymer molecules. The individual domains within one particle can be visualized in phase image, which cannot be clearly seen in topography channel.

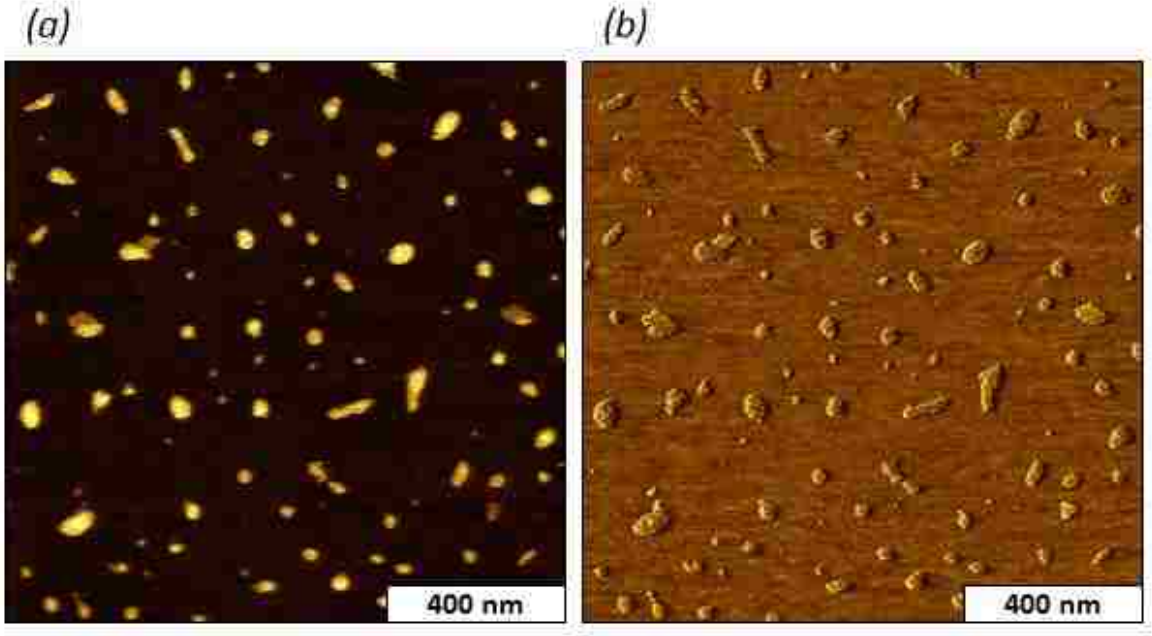

Figure 2.6 Example of composition mapping of bottlebrush polypeptoid norbornenyl-terminated poly(*N*-ethyl glycine)$_{36}$-*r*-poly(*N*-butyl glycine)$_{12}$ copolymers prepared on a mica substrate imaged with tapping-mode. (a) Topograph with z scale of 2.0 nm and (b) phase image.

2.5 Force Modulation Microscopy

Force modulation microcopy (FMM) was invented in 1991 by Maivald and Hansma et al.[14] The FMM mode is used to measure the dynamic response of samples while applying modulated pressure to surfaces during contact-mode imaging. Measurements of elasticity and viscoelasticity

can be acquired with FMM. Materials that have been studied with FMM include patterned self-assembled monolayers (SAMs),[60] polymer blends and resins,[61-64] protein-lipid aggregates,[65] wood cells and fibroblasts,[66-68] bacteria,[69] porous silicon,[70] as well as optical thin film materials.[71] Quantitative measurements such as Young's modulus[72-74] and the elasticity[75-76] of samples can be evaluated using FMM.

For force modulation microscopy, the tip is operated in contact-mode, which means the tip is operated in continuous contact with the surface during scanning. Either the sample or tip is driven to vibrate with pressure applied at the area of tip-sample contact. Most commonly FMM has been done using an instrument configuration with the sample placed directly on top of an xyz scanner and actuation of the z piezoelement causes the sample to vibrate for tip displacements of a few nm in the z-direction.[62, 77-82] For a scan-by-tip AFM configuration, an FMM sample stage was invented by our group in collaboration with Dr. Song Xu and Sonimoto Laboratory to facilitate FMM measurements. Machined polycarbonate was used to construct the sample stage. Current can be applied through a coxial cable connection to the piezoactuator within the stage to generate z axis vibration. Details of the FMM sample stage will be presented in Chapter 6.

Other than stage-driven FMM, tip-vibration FMM has been developed and applied. For example, a cantilever holder equipped with bimorph piezoelements was used to accomplish force modulation, which can actuate the tip as it is pressed against the sample.[63, 83-84] A magnetic field has been used to drive the vibration of a tip or tip-holder assembly to accomplish force modulation imaging.[76, 85-88] One way to use magnetically actuated system, named indirect magnetic modulation (IMM), was introduced by our group.[86] For IMM, an AC current is applied to a MAC mode sample stage and an electromagnetic field is generated from a solenoid underneath the MAC stage. A tip-holder assembly or nosecone containing ferromagnetic material is induced to vibrate

with the flux of the electromagnetic field. The AFM is operated in contact-mode, therefore, information of height, elasticity and adhesion are simultaneously acquired. The vibration frequency and amplitude can be tuned to obtain the highly sensitive images.[89] Comparison of FMM using the newly designed sample stage and IMM will be presented in Chapter 7.

An example of indirect magnetic modulation imaging is shown in Figure 2.7. Patterned nanorings of 2-[methoxy(polyethyleneoxy)propyl]trichlorosilane (PEG-silane) prepared using particle lithography combined with silane vapor deposition were imaged with IMM at frequency 266 kHz. Identical information can be obtained from IMM and contact-mode topographs, which are height profiles of the surface (surface z scale: 1.5 nm). The nanorings protrude from the surface shown in the Figure 2.7a. The amplitude channel represents the softness and hardness of the sample, showing brightest contrast for the center of the ring and darkest for the ring. The center of the ring is the hard silicon substrate and the ring is a softer PEG multilayer. When presses a soft surface, the amplitude of the tip is dampened.

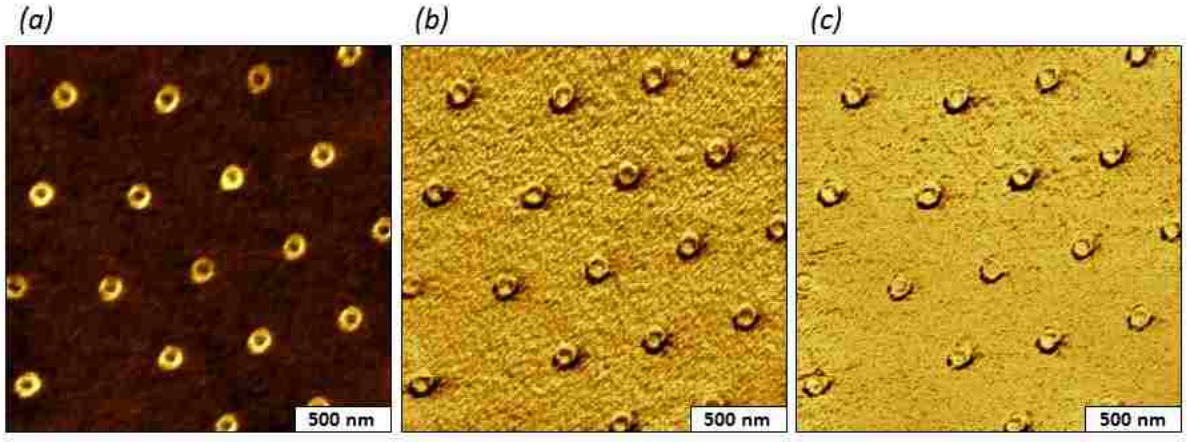

Figure 2.7 Nanorings of 2-[methoxy(polyethyleneoxy)propyl]trichlorosilane imaged with indirect magnetic modulation at vibration frequency of 266 kHz. (a) Topography, (b) amplitude, and (c) phase images.

2.6 *In Situ* Temperature Studies Using AFM

Dynamic studies with time-lapse AFM experiments using a heating stage have been reported.[90] The crystallization and melting of poly(ethylene oxides) and polyethylene,[91-92] the crystal-mesophase transition of poly(di-n-hexylsilane) and poly(di-n-butylsilane),[93] the phase transition behavior of single thermo-responsive hydrogel particles: poly(*N*-isopropylacrylamide-co-acrylic acid),[94] the phase transition of a nanocomposite,[86] and diblock copolymer domains in directed self-assembly have been investigated *in situ* using AFM.

An example of a sample stage with temperature control is shown in Figure 2.8. This is the stage used in Chapter 4 for an *in situ* study of thermos-responsive polypeptoids. The yellow metal piece in the center of stage (Figure 2.8a) is used to heat the sample. The metal pin on the back of the stage (Figure 2.8b) is used to connect the stage with the control box (Figure 2.8c). The stage can be heated up to 250 C with accuracy up to ±0.025 C with low thermal drift.

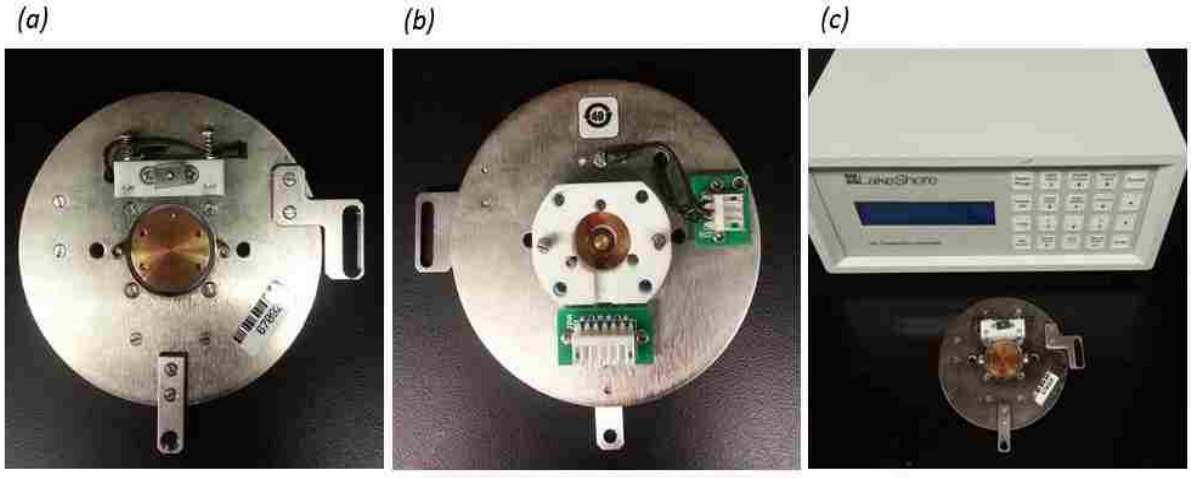

Figure 2.8 Photographs of the heated stage and control box. (a) Front side of the heated sample stage. (b) Backside of the heating sample stage. (c) Control box and the heated stage.

2.7 AFM imaging Modes Used in the Dissertation

An overview of the imaging modes used in this dissertation is outlined in Table 2.1. The imaging modes were selected based on the surface properties of samples. Force modulation

microscopy using the designed sample stage versus indirect magnetic modulation are compared in Chapter 7.

Table 2.1 Modes of SPM used in Dissertation Research Experiments

Chapter	Sample description	Contact-mode and lateral force imaging	Tapping-mode and phase imaging	*In situ* temperature study	Force modulation using new stage	Indirect magnetic modulation
3	Poly (*N*-allyl glycine) "grafted from" Si(111)	X	X			
4	Copolypeptoids "grafted to" Si(111)	X		X		
6	Organosilane nanopatterns and polymeric gels				X	
7	Nanorings of organosilanes				X	X

CHAPTER 3. DIRECTED GROWTH OF POLYMER NANOPILLARS USING SURFACE-INITIATED RING-OPENING POLYMERIZATION OF *N*-ALLYL *N*-CARBOXYANHYDRIDE

3.1 Introduction

Peptide-functionalized thin films have been applied as stimuli responsive materials,[95] anti-fouling agents[96-97] and as inorganic/peptide hybrids.[98] Poly(α-peptoid)s, a class of pseudo-peptidic polymers, feature a polyglycine backbone with substitution on the nitrogen atoms.[99-100] The biocompatibility, backbone degradability and processability of poly(α-peptoid)s make these polymers useful for applications such as smart coatings, biosensors and bioseparations.[99] There are relatively few publications reporting studies of polypeptoid thin films[101] or reports focusing on nanopatterns of polypeptoid brushes on surfaces. Surface structures of peptides have previously been reported to accomplish micron-scale patterning using photolithography[102-103] and micro-contact printing.[104-105] We report results for combining particle lithography with surface-initiated ring-opening polymerization of *N*-allyl *N*-carboxyanhydride (allyl-NCA) to prepare polymer pillars of poly(*N*-allyl glycine).

To prepare polypeptide/peptoid brushes, there are two commonly used methods, "graft to" and "graft from".[106-107] The "graft to" approach involves a reaction between surface reactive moieties and the end-groups of pre-synthesized polypeptide/peptoid. The method is experimentally simple however it is difficult to achieve high grafting densities because of the steric crowding. The "graft from" method, also known as the "surface-initiated" approach, occurs through a ring-opening polymerization of α-amino acid *N*-carboxyanhydride (NCAs) with initiators attached to surfaces. Control of the functionality, density and thickness of polymer nanopillars with molecular precision using the "graft from" approach can be readily achieved.[106]

Amine-functionalized substrates in either solution or vapor phase were used to prepare thin films of polypeptide brushes using surface-initiated polymerization (the "graft from" method).[108-

[114] The "graft from" and "graft to" approaches for grafting poly (*γ*-benzyl-*L*-glutamate) (PBLG) film on silicon oxide surface was reported in 1996.[109] To obtain better control of PBLG film thickness, a protocol with vapor deposition polymerization was developed which involved a reaction between the vapor species of *γ*-benzyl-*L*-glutamate and a primary amine modified silicon substrate.[110] The vapor deposition method was improved so that the *α*-helical PBLG films were fabricated in less than 1 h with tunable thickness from a few nanometers to hundreds of nanometers.[115] Mechanistic studies of surface-initiated vapor deposition polymerization of PBLG were reported by Zheng *et al*.[116] The helix orientation of PBLG and poly(*γ*-methyl *L*-glutamate) (PMLG) were studied using FT-IR transmission spectroscopy.[117-119] The surface-grafting of AB-block copolypeptides, PBLG-*b*-PMLG, was also introduced.[119] Synthesis of surface-tethered poly(*L*-glutamic acid) (PLGA) and poly(*L*-lysine) (PLL) and the conformational transition (*α*-helix, *β*-sheet, and random coil) for the responsiveness to the external stimuli of pH, surfactant and ions were investigated using circular dichroism (CD).[120-122] Well-defined homo- and block-polypeptides were prepared by transition metal-mediated polymerization of NCAs, demonstrated by Deming *et al*.[123-125] Polystyrene particles functionalized with PBLG were obtained by ring-opening polymerization of NCAs by nickel amido-amidate complexes.[126] Thiol-clickable and block copolypeptide brushes were synthesized via a nickel-mediated surface-initiated polymerization resulting in an effective approach to functionalize polypeptide surfaces.[107]

Particle lithography, is a facile and versatile fabrication technique applicable for generating nanostructures with regular nanoscale geometries with high reproducibility.[127] Solutions of monodisperse mesospheres self-assemble into close-packed arrangements on surfaces during evaporation of solvents. The periodic mask that is formed on surfaces can be used for nano- or micron- scale fabrication.[127-131] The advantages of particle lithography include the generic use of

basic lab equipment and experimental steps, and the capability for tuning the dimensions of surface structures according to the diameters of mesospheres.[128]

Using particle lithography, porous polymer films were prepared using materials, such as polycaprolactone,[132] poly(*N*-isopropylacrylamide),[133] polyethersulfone,[134-135] and polythiophene.[136-137] The first surface-initiated and site-specific Suzuki polycondensation to quickly and selectively graft polyfluorene from functionalized, sub-micron surface patterns at room temperature was developed by Beryozkina et al.[138] A range of robust and simple patterning strategies using microsphere arrays as a surface mask were combined with surface-initiated atom transfer radical polymerization to fabricate patterned triangular, ring-shaped, dot-like, or hole-like poly(*N*-isopropylacrylamide) brush microstructures.[139-140] Surface-imprinted polymer films for protein recognition were prepared by immobilizing avidin on monodisperse polystyrene beads, then depositing the beads onto gold-coated quartz crystal, followed by electropolymerization of 3,4-ethylenedioxythiophene and finally dissolving away the beads.[141] A binary compositionally patterned surface containing poly(carbazole) and poly(*N*-isopropylacrylamide) was prepared via colloidal-template assisted electropolymerization followed by growing the polymer brushes using SI-ATRP.[142]

Particle lithography and organosilane chemistry were used to prepare nanopores within a thin film of octadecyltrichlorosilane (OTS).[143-144] Uncovered sites of Si(111) were backfilled with (3-aminopropyl)triethoxysilane (APTES) as a means to direct the growth of *N*-allyl *N*-carboxyanhydride (allyl-NCA).[145] Each step during the preparation of the surface platform was characterized by atomic force microscopy (AFM), which has been previously used for studying surface-grafted polymer nanopillars.[146-151] The polypeptoid nanopillars have reactive side chains, since allyl-NCA with a pendent allyl group was chosen as the monomer. The polymer can be

further functionalized by thiol-ene click reaction for constructing complex surface structures.[152-154]

3.2 Experimental Section

3.2.1 Materials and Reagents

Reagents were used as received without further purification. Octadecyltrichlorosilane (OTS) was purchased from Gelest (Morrisville, PA). Anhydrous toluene, bicyclohexyl, (3-Aminopropyl)triethoxysilane (APTES), dichloroacetic acid, chloroform, sulfuric acid (ACS reagent 95%) and hydrogen peroxide (30%) were obtained from Sigma-Aldrich. Pieces of single-sided polished Si(111) doped with boron (Ted Pella, Inc., Redding, CA) were used as substrates. Monodisperse silica mesospheres with diameter 0.49 ± 0.02 μm were acquired from Duke, Inc. (Fremont, CA). The deionized water used for experiments was from a Direct-Q3 system (18 MΩ, Millipore, Bedford, MA).

3.2.2 Atomic Force Microscopy

Samples were characterized using either a model 5500 or 5420 atomic force microscope (Agilent Technologies, Chandler, AZ). Nonconductive V-shaped cantilevers made of silicon nitride with force constants ranging from 0.01-0.60 N/m were used for contact-mode imaging (Bruker Probes, Camarillo, CA). Silicon nitride cantilevers with an average force constant of 48 N/m and a resonance frequency of 190 kHz were used for tapping-mode imaging (Vista probes, Phoenix, AZ). Images were processed using Gwyddion open source software which is supported by the Czech Metrology Institute.[155]

3.2.3 Preparation of Nanopores within an OTS Film

Particle lithography was used to generate organosilane nanopore patterns on Si(111) surfaces.[143] The silicon substrates were cleaned by immersion in piranha solution for 2 h. Piranha solution, which is a mixture of sulfuric acid and hydrogen peroxide at a ratio of 3:1 (v/v), is highly

corrosive and should be handled cautiously. Substrates were rinsed copiously with deionized water and dried under argon. Monodisperse silica mesospheres were washed three times by centrifugation to remove trace charge stabilizers or surfactants. The pellet of silica mesospheres was resuspended in water by vortex mixing, and a drop (10 μL) was deposited on a clean substrate. The sample was dried in air for 2 h to produce surface masks for further chemical steps. As water evaporated during the drying step, capillary forces pull the mesospheres together to form crystalline layers on flat surface. Next, the substrate was placed in an oven at 140 C for 24 h to temporarily anneal the mesospheres to the surface. After cooling, the sample was immersed in a 0.1% solution of OTS (v/v) in toluene for 5 h. Next the sample was rinsed with water and ethanol. To remove the mesoparticles, the substrate was sonicated for 15 min in ethanol and water successively. The sample was dried under argon for AFM characterization.

3.2.4 Preparation of APTES Nanodots

The substrate (polished Si wafer) with OTS nanopores was cleaned by sonication in ethanol for 10 min to remove contaminants, then dried under argon. Uncovered bare areas of the Si substrates were backfilled with initiator by immersion in an APTES solution (0.02% v/v solution of APTES in bicyclohexyl for 3 h). Next, the samples were rinsed with acetone, water and ethanol, followed by 15 min sonication in ethanol and in water. The samples were dried under argon and characterized with AFM.

3.2.5 Three Steps Synthesis of Allyl-NCA

Synthesis of 2-(Allylamino)acetic Acid Hydro-chloride: Allylamine (15 mL, 0.2 mol) and glycoxylic acid (30 g, 0.4 mol) were both dissolved in CH_2Cl_2 and stirred at room temperature for a period of 24 h. The solvent was removed and 1 N HCl aqueous solution (300 mL) was added to the flask (Scheme 3.1). The mixture was refluxed overnight at 110 C. The solvent was evaporated to yield brown viscous oil. Recrystallization in cold methanol and THF afforded white crystals

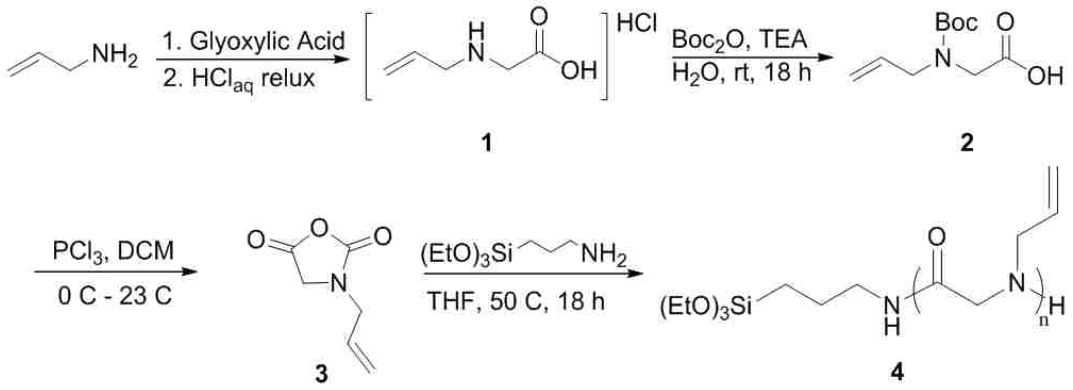

Scheme 3.1 Synthetic procedure for allyl-NCA

(11.53 g, 38% yield). ^{1}H NMR (δ in MeOD, ppm): 5.7 (m, =C*H*-); 5.3 (t, =C*H*$_2$); 3.7 (s, -C*H*$_2$-); 3.5 (d, =CHC*H*$_2$-). ^{13}C{^{1}H} NMR (δ in $CDCl_3$, ppm) 166.3 (C=O); 129.8 (-*C*H=CH$_2$); 121.0 (-CH=*C*H$_2$); 48.9 (-CH$_2$-); 46.4 (-*C*H$_2$-).

2-(Allyl(tert-butoxycarbonyl)amino)acetic Acid (2): 1 (11.53 g, 0.076 mol) and di-tert butoxide (41.40 g, 0.191 mol) were dissolved in distilled water (250 mL). The solution was stirred, and then triethylamine (53.10 mL, 0.382 mol) was added via syringe. The reaction was stirred overnight at room temperature. The solution was washed with hexanes to remove excess di-tert-butoxide (100 mL) and then the aqueous portion was made acidic using 1N HCl (roughly 150 mL). The aqueous portion was washed twice with ethyl acetate (100 mL) then the combined organic layers were washed once with brine (70 mL). The organic layer was dried with $MgSO_4$, filtered and then the solvent was removed under vacuum to yield a pale yellow oil (16.2 g, 0.075 mol, 99% yield). ^{1}H NMR (δ in $CDCl_3$, ppm): 10.4 (bs, -O*H*); 5.7 (m, =C*H*-); 5.3 (t, =C*H*$_2$); 3.7 (s, -C*H*$_2$-); 3.5 (d, =CHC*H*$_2$-); 1.4 (s, -(C*H*$_3$)$_3$). ^{13}C{^{1}H} NMR (δ in $CDCl_3$, ppm): 173.4 (-N*C*OO-); 167.1 (-*C*OOH); 131.1 (-*C*H=CH$_2$); 119.9 (-CH=*C*H$_2$); 78.9 (*C*(CH$_3$)$_3$); 49.8 (-*C*H$_2$N-); 47.6 (-*C*H$_2$CH=); 28.1 (-(*C*H$_3$)$_3$).

Synthesis of Allyl-NCA (3): **2** (16.2 g, 0.075 mol) was dissolved in anhydrous dichloromethane and while under an argon atmosphere, the solution was chilled to 0 C. PCl_3 (7.5 mL, 0.086 mol) was added to the solution via syringe. The solution was stirred at 0 C for one hour, after which the solution was kept at 25 C for 2 h. The solvent was then removed under vacuum and the flask was placed into a glove box. The residue was redissolved in anhydrous dichloromethane, and stirred with NaH for 10 min. The solution was filtered and the filtrate was concentrated, leaving clear oil. The oil was vacuum distilled at 60 C in the modified vacuum distillation apparatus. The final product was a clear liquid (5.94 g, 0.042 mol, 54%). ^{1}H NMR (δ in Tol-d_8, ppm): 5.2 (m, =C*H*); 4.8 (m, =CH_2); 3.4 (d, -CH_2-); 2.9 (s, =CHCH_2-). ^{13}C{^{1}H}c NMR (δ in Tol-d_8, ppm): 160.3 (-CH$_2$*C*(O)O); 147.0 (-O*C*(O)N-); 132.1 (-*C*H=CH$_2$); 113.7 (*C*H$_2$=CH-); 42.4 (=CH*C*H$_2$N-); 40.3 (C(O)*C*H$_2$N-).

3.2.6 Polymerization of Allyl-NCA.

Substrates with OTS and APTES nanopatterns were immersed for 24 h in 0.43 M allyl-NCA solution in THF at 50 C under N_2. Afterward, the substrates were rinsed with THF and then immersed for 2 days in a mixture of dichloroacetic acid and chloroform at a 1:4 (v/v) ratio to remove physically adsorbed molecules, followed by rinsing with chloroform, water and ethanol. The sample was then dried under argon.[117]

3.3 Results and Discussion

The strategy for spatially directing the polymerization of allyl-NCA is outlined in Figure 3.1. A close-packed arrangement of silica mesospheres on Si(111) served as a surface mask for defining the sites for depositing of OTS (Figure 3.1a). A masked substrate was immersed in a solution of OTS to enable molecules to self-assemble on areas of exposed Si surrounding the mesospheres (Figure 3.1b). Nanopores within the OTS thin film were produced after removal of silica mesospheres (Figure 3.1c). The initiator (APTES) was selectively grown inside the OTS

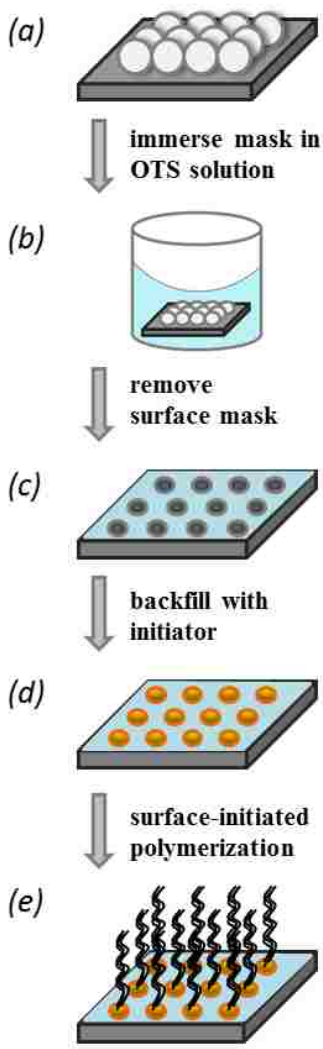

Figure 3.1 Steps for preparing poly(*N*-allyl glycine) nanopatterns. (a) An drop of an aqueous suspension of silica mesospheres was dried on a Si wafer and annealed to provide a surface mask. (b) The sample was immersed in a solution of OTS in toluene. (c) The mask of silica mesospheres was removed by sonication. (d) The uncovered areas within the nanopore were filled with initiator by immersing the sample in an APTES solution. (e) Columnar nanostructures were formed using surface-initiated ring-opening polymerization of *N*-allyl *N*-carboxyanhydride.

nanopores to form a chemically patterned surface (Figure 3.1d). The nanodots of APTES provided sites for spatially selective growth of polymer. Surface-initiated ring-opening polymerization of allyl-NCA took place at sites where the primary amine (APTES) was located (Figure 3.1e).

Preparation of Nanopores within a Film of OTS. Particle lithography was used to generate OTS nanopores described in step c of Figure 3.1 as the first step of sample preparation. Nanoscale views of the nanopores are shown in Figure 3.2 with successive zoom-in topography images acquired with contact-mode AFM. The nanopores within a matrix film of OTS form a periodic arrangement according to the locations of the mesospheres of the surface mask. The topographs (Figures 3.2a-c) display dark spots where the mesospheres were rinsed away to reveal the Si substrate. The wide-area topography frame of Figure 3.2a ($6.7 \times 6.7\ \mu m^2$) discloses the regular arrangement of 211 nanopores, which would scale to ~10^9 nanopores per cm^2. Approximately 97% of the surface is covered with OTS. Zoom-in views of the nanopores reveal slight differences in the shapes and sizes of the nanopores (Figures 3.2b and 3.2c). The imperfections are caused by factors such as the nanoscale variations in mesoparticle sizes and the roughness of the polished silicon wafers. The lateral dimensions of the nanopores measure 108 ± 29 nm. Bright spots indicate the shapes and locations of nanopores in the lateral force frame of Figure 3.2d. The slight differences in the sizes of surface sites will eventually propagate into size variations for polymer nanostructures. The nanopores do not appear to contain OTS according to the contrast of the lateral force frame (Figure 3.2d). In lateral force images, the color contrast is attributable to chemical differences for local areas of samples. The distance between two nanopores shown in Figure 3.2e measures ~500 nm, which matches the size of the silica mesospheres (490 ± 20 nm) used for the surface mask (Figure 3.2e). The depth of the nanopores measures 1.9 ± 0.1 nm, which is smaller than the reported height of a densely packed, upright monolayer of OTS (~2.6 nm).[156] The shorter height indicates that the molecules within the OTS film are not densely packed.

The nanopores within the OTS matrix were used as a foundation for further patterning steps to form polypeptoid nanostructures. Methyl terminal groups of OTS are presented at the interface

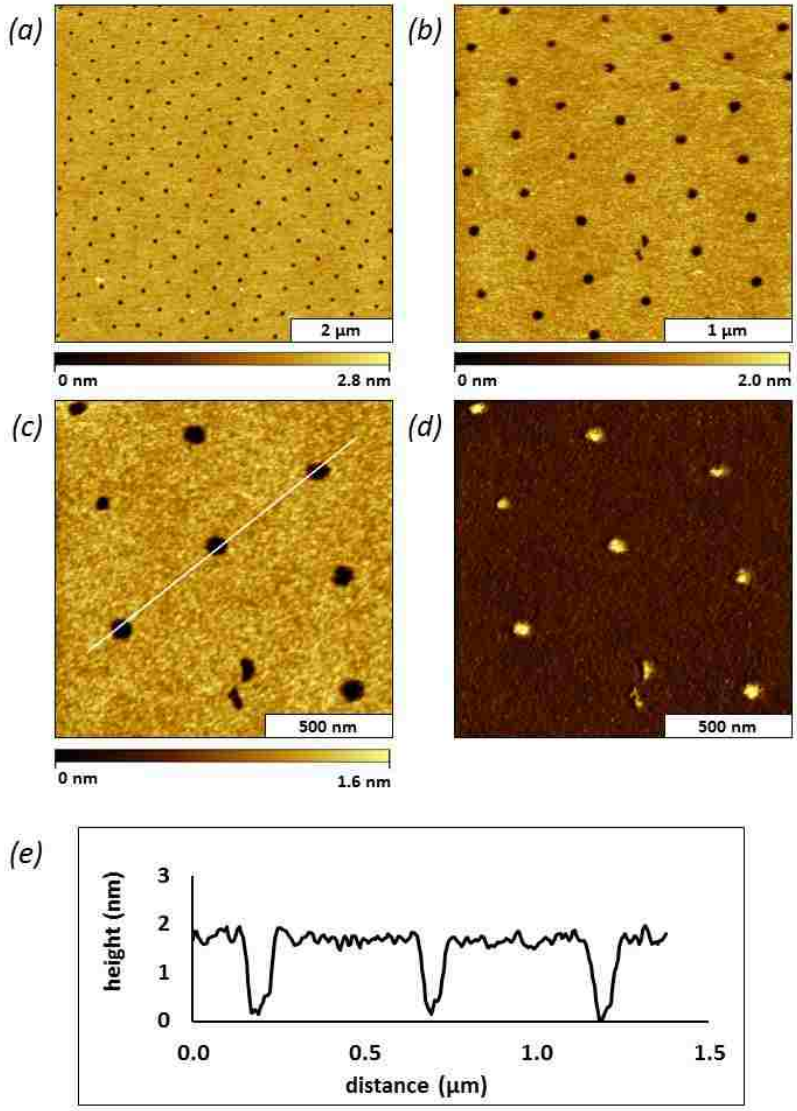

Figure 3.2 Nanopores within a film of OTS prepared using 500 nm silica mesospheres. (a) Contact-mode AFM topography image of nanopatterns prepared on Si(111). (b) Zoom-in view. (c) Magnified view of nanopores and (d) simultaneously acquired lateral force image. (e) Cursor profile for the line in c.

to furnish a resist layer that does not react with allyl-NCA for patterning of polypeptoid. The nanoscopic bare areas of the Si substrate within the nanopores provide hydroxyl groups to spatially define sites where amino-silane molecules will bind to grow polymer nanostructures.

Selective Filling of APTES Initiator into Nanopores. The initiator **(**APTES) molecules assembled into the uncovered areas of the Si substrate within OTS to form regular nanodot patterns, as shown in Figure 3.3. The bright spots are backfilled APTES nanodots and the darker areas in the background are the OTS matrix (topography frame, Figure 3.3a). The hexagonal arrangement

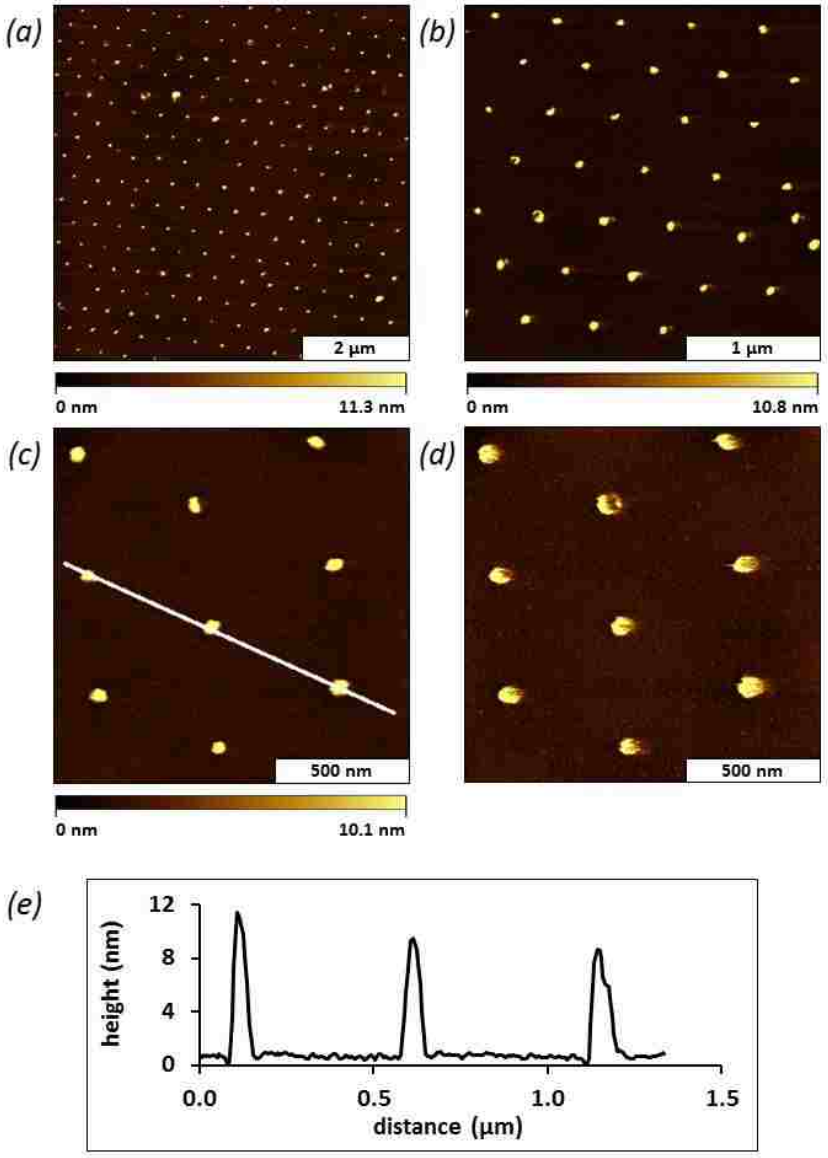

Figure 3.3 After selective filling of the nanopores with APTES, surface views with contact-mode AFM. (a) The nanodots of APTES are taller than the surrounding OTS resist in the topography images, 6.7 × 6.7 μm^2; (b) zoom-in topograph; (c) close-up view of eight nanodots with (d) corresponding lateral force image. (e) Height profile for three nanodots indicated in ***c***.

of APTES nanodots are apparent in Figures 3.3b and 3.3c. There are 38 nanodots in Figure 3.3b, which accordingly scales to ~10^9 nanodots per cm^2. The results indicate that OTS is an excellent resist since the growth of APTES was confined to areas inside the nanopores. The surface contains chemical patterns of methyl and amine terminal groups for further steps of site selective polymer growth. The differences in surface chemistry are distinctly apparent in the high-resolution lateral force image of Figure 3.3d. The height of the nanodots measured 10 ± 1.2 nm (including the depth of the nanopores), which corresponds to multilayers of APTES. The height of three selected APTES nanodots are shown in Figure 3.3e as an example measurement. The lateral dimension of the APTES nanodots measured 110 ± 25 nm, which matches the dimensions of the unfilled nanopores.

Polymerization of Allyl-NCA to Form Nanopillars. The primary amine functional groups on the nanodots of APTES were used to initiate polymerization of allyl-NCA to form columnar nanopillars. Although APTES formed multilayers, the initiation reaction should still take place since amine groups are present at the interface. Columnar nanopillars of poly(*N*-allyl glycine) are shown in Figure 3.4, imaged using tapping-mode AFM. The round bright spots are polypeptoids grown on APTES nanodots, and the darker areas are the surrounding matrix film of OTS. The periodicity of the nanopatterns is retained after polymerization as revealed in the wide-area topograph of Figure 3.4a. The image is representative of the entire sample, with ~97% surface coverage of OTS and ~3% coverage of poly(*N*-allyl glycine). Views of individual nanopillars disclose the slight differences in shapes and heights of the nanostructures (Figure 3.4b). A few adsorbates are present between poly(*N*-allyl glycine) pillars. The heights of two representative polymer nanopillars are shown in Figure 3.4c. The average height measured 16 nm which indicates that the degree of polymerization is approximately 14 (the height of the multilayer of APTES was

removed from the calculation). The tallest nanostructure is 35 nm, which shows the highest degree of polymerization assuming that the polymer backbone is fully stretched (~62). The shortest nanostructure is 10 nm, which is the same height as the APTES nanodots indicating that no polymerization took place at some sites (10% of the polymer nanodots). The lateral dimension of the polypeptoids measured 110 ± 13 nm, which closely matches the lateral dimensions of APTES nanodots. The heights suggest that poly(*N*-allyl glycine) growth is predominantly in the z direction,

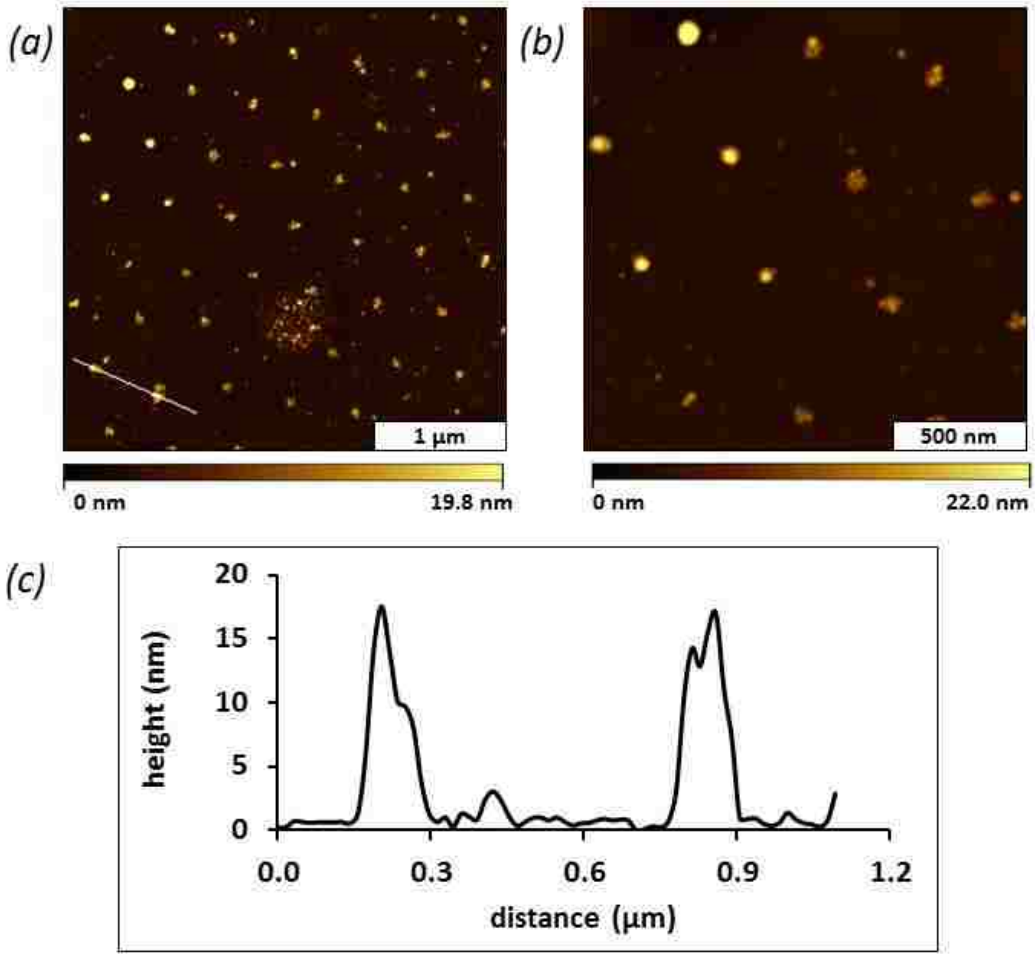

Figure 3.4 Surface-initiated ring-opening polymerization of *N*-allyl *N*-carboxyanhydride on sites with APTES nanodots. (a) Nanostructures are taller after steps of polymerization, shown in the topographs; (b) zoom-in view of polypeptoid pillars; (e) Cursor profile for two nanopillars in ***a***.

rather than growth of wider nanostructures. The distance between two polymer nanopillars measured ~500 nm, corresponding to the expected dimensions of the silica mask.

The APTES initiated ring-opening polymerization of allyl-NCA in solution is a living polymerization. When polymerization occurs on the surface, the reactivity of molecules is spatially restricted. Since the sizes of the nanopores are slightly different, the number of APTES molecules within a single nanopore varies, which influences the chain lengths of poly(*N*-allyl glycine). With increase of the nanopore size, the heights of the polymer nanopillars correspondingly increased. However the growth did not correspond to a linear relation. The drawback of using the "graft from" method leads to an increased difficulty in controlling both the initiation and propagation steps.

Three Key Steps of Preparing Patterned Poly(*N*-allyl glycine). The key steps to prepare patterned polymer nanopillars are shown in Figure 3.5. Nanopores within a film of OTS were prepared using particle lithography combined with silane immersion (Figure 3.5a). The APTES initiator was backfilled into exposed sites of OTS nanopores and formed nanodots (Figure 3.5b). Polymerization of allyl-NCA occurred selectively at sites where APTES nanodots were located (Figure 3.5c).

The changes in height between each step are apparent from the topography views (Figure 3.5). The depth of the nanopores measured 1.9 ± 0.1 nm, while the short nanodots formed after backfilling APTES have average height 10 ± 1.2 nm. The average length of the polymer chains measured 6 nm. The height of the APTES showed a substantial change during the 3 h immersion step, as compared with one day of growth for allyl-NCA. The difference in growth for organosilane molecules is attributable to the capability to readily polymerize with moisture in the system.[157-158] The polymerization step shows a few areas of nonselective growth in the surrounding OTS matrix, since small amounts of adsorbed polymer or monomer attached to the surface and could not be

fully rinsed away (Figure 3.5c). 2) Also, nanoscopic amounts of water on the surface will initiate the polymerization of allyl-NCA.

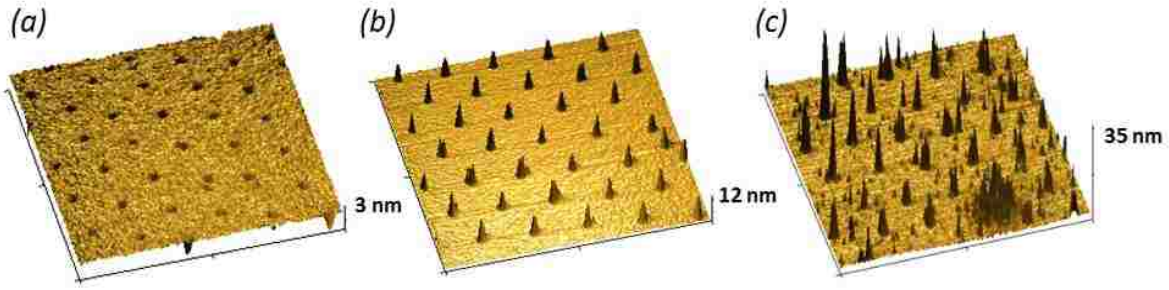

Figure 3.5 Key steps for making patterned poly(*N*-allyl glycine) nanopillars by surface-initiated ring-opening polymerization. ($2.7 \times 2.7\ \mu m^2$ topographs) (a) Nanopores within a film of OTS; (b) nanodots of APTES filled into the exposed sites of nanopores; (c) nanopillars of poly(*N*-allyl glycine).

3.4 Conclusion

The polymerization of allyl-NCA was studied within spatially confined, well-defined nanoscale sites. Nanoscale patterned poly(*N*-allyl glycine) pillars were prepared on Si(111) by surface-initiated ring-opening polymerization. Nanopores within a self-assembled monolayer of OTS were generated using particle lithography combined with steps of immersion in solution. Molecules of APTES were backfilled into nanopores within a template film of OTS, to form patterned nanodots as sites to initiate the polymerization of allyl-NCA. The clickable side chain of the polymer nanopillars can be functionalized for future applications. The biocompatibility, biodegradability of poly(*N*-allyl glycine), and control of the distance between polymer nanopillars make this surface platform potentially useful in biomedical and biosensor applications.

CHAPTER 4. THERMO-RESPONSIVE BEHAVIOR OF LINEAR COPOLYPEPTOID NANOSTRUCTURES INVESTIGATED WITH ATOMIC FORCE MICROSCOPY

4.1 Introduction

Thermo-responsive surfaces formed by polymeric materials have received recent attention due to the potential applications.[159] Among the polymeric materials, poly(*N*-isopropyl acrylamide), or PNIPAAm, is the most often studied system due to its lower critical solution temperature (LCST of 32 C), just below the human physiological temperature (37 C).[160-163] Temperature-responsive surfaces prepared with PNIPAAm have been investigated for applications in tissue culture and microfluidics,[164-165] display and sensor technology,[166] cell-seeding and co-culture.[167] Surface grafted PNIPAAm on regenerated cellulose membranes have thermally modulated permeability.[168] Responsive copolymer systems having PNIPAAm segment have been studied.[169-174] For example, poly(*N*-isopropylacrylamide-*co*-dopamine methacrylamide) was synthesized and attached to a Si wafer for cell sheet applications.[169] A gold nanoparticle with surface-linked poly(styrene-*b*-*N*-isopropylacrylamide) copolymer formed temperature-responsive core-shell micelles.[170] Other thermo-responsive polymers have been used to make stimuli-responsive surfaces, including poly[di(ethyleneglycol)methyl ether methacrylate],[175] poly[oligo(ethylene oxide)monomethyl ether methacrylate]-based star polymers,[176] gradient and block copolymers based on 2-(2-methoxyethoxy)ethyl methacrylate,[177] acetylated poly-*N*-[tris(hydroxymethyl)methyl] acrylamide,[178] as well as other systems.[179-181]

The two common methods to decorate surfaces with polymer are the "grafting from" and "grafting to" methods. The "grafting from" method, usually occurs through a surface-initiated polymerization of selected monomers. Using this method, the grafting density is nearly quantitative, but at the expense of control of the polymer brushes (which tend to have broader molecular weight distributions than polymer brushes from the "grafting to" method).[182] The

"grafting to" approach involves the coupling reaction between surface reactive moieties and the end-groups of functionalized polymer. Though this method having the advantages of controlling the brush polymer molecular weight, architecture and microstructure, high grafting densities are compromised due to steric crowding.

Many "grafting to" approaches use click reactions to prepare surface tethered polymer brushes because the reaction proceeds with high yields and no byproducts.[183-185] Among several types of click reactions, the copper (I) catalyzed azide-alkyne cycloaddition (CuAAC) is most widely used.[186-196] Three examples of CuAAC are ligand α-acetylene-poly(*tert*-butyl acrylate) with alkyne end group attached to azide functionalized γ-Fe_2O_3 nanoparticles,[197] temperature sensitive nanocomposites of immobilizing thermo-responsive PNIPAAm on Au nanoparticles,[198] and polystyrene/polyacrylamide functionalized silica nanoparticles with the combination of living radical/tandem polymerization and azide-alkyne click reaction.[199-200] Azide-alkyne and thiol-ene click reaction can be used at the same time, as demonstrated previously by others, to form binary polymer brushes on silica spheres, followed by removal of the inorganic silica core in hydrogen fluoride solution to obtain hollow polymer nanospheres.[201] The thiol-ene click reaction is a less commonly used click coupling reaction. However, this reaction is still a efficient, rapid and nearly quantitative method to tether polymers to surfaces.[202-204] A major advantage of thiol-ene chemistry is that this method leaves no trace metal residues in the system as compared with azide-alkyne reaction.[202-204] As demonstrated with poly(oligo(ethylene glycol)methyl ether methacrylate) coated titanium dioxide nanoparticles, the thiol-ene reaction can reduce particle aggregation and cellular uptake as well as diminish cytotoxicity.[205]

Thiol-functionalized linear random copolypeptoid poly[(*N*-ethyl glycine)$_{32}$-*r*-(*N*-butyl glycine$_{17}$)], or P(NEG$_{32}$-*r*-NBG$_{17}$), was synthesized in solution phase. Particle lithography and

thiol-ene click reaction were combined to pattern the copolypeptoids on a surface. The thermo-responsiveness of patterned copolypeptoids was studied using *in situ* atomic force microscopy (AFM). Unlike homogeneous film on surface, this work shows the thermo-responsiveness of the polymer nanopillars on surface are more pronounced and easier to detect. The *in situ* studies of the thermo-responsiveness of patterned polymer pillars at the nanoscale will be discussed for the first time.

4.2 Experimental Section

4.2.1 Preparation of Nanopatterned UTS Sites

Nanopores within a thin film of OTS on Si wafer were prepared with a previously reported method.[206] The diameter of the silica mesospheres used in the experiment is 0.49 ± 0.02 μm (Duke, Inc. Fremont, CA). The substrate with OTS nanopore patterns was characterized with AFM and the result is shown in Appendix Figure C1. The patterned bare areas of the Si substrate were backfilled with UTS by immersing substrate in UTS solution (0.1% v/v solution of UTS in bicyclohexyl) for 5 h. Next, the sample was rinsed with three solvents (water, THF and ethanol), followed by sonication in ethanol and sonication in water to remove excess amount of silane. The sample was characterized with contact-mode AFM in air.

4.2.2 Synthesis of Linear poly[(*N*-ethyl glycine)$_{32}$-*r*-(*N*-butyl glycine)$_{17}$] Copolymer

The copolymer was prepared based on previous report.[207] Inside the glovebox, *N*-ethyl *N*-carboxyanhydride (137.0 mg, 1.062 mmol) and *N*-butyl *N*-carboxyanhydride (55.6 mg, 0.354 mmol) were dissolved with 1.0 mL toluene in a vial. 4-aminothiophenol (3.5 mg, 0.0283 mmol) in 2.9 mL toluene was added to the monomer solution (Scheme 4.1). The vial was sealed under nitrogen and stirred at 50 C for 27 h. An aliquot of the reaction mixture was taken for conversion analysis. Excess cold hexane was added to the reaction solution to precipitate the polymer. White solid was collected by filtration, washed with hexanes, and dried under vacuum (86 mg, 44% yield).

Size exclusive chromatography (Mw = 14.5 kDa, PDI = 1.24). ^{1}H NMR (δ in CD_2Cl_2, ppm): 0.82-1.00 (bt, C*H*$_3$CH$_2$-, NBG), 1.05-1.21 (bt, C*H*$_3$CH$_2$-, NEG), 1.23-1.70 (bm, -C*H*$_2$C*H*$_2$CH$_3$), 3.13-3.64 (bm, - NC*H*$_2$CH$_3$, -NC*H*$_2$CH$_2$-), 3.88-4.43 (bm, -COC*H*$_2$-). (1H NMR spectrum in Appendix Figure C4).

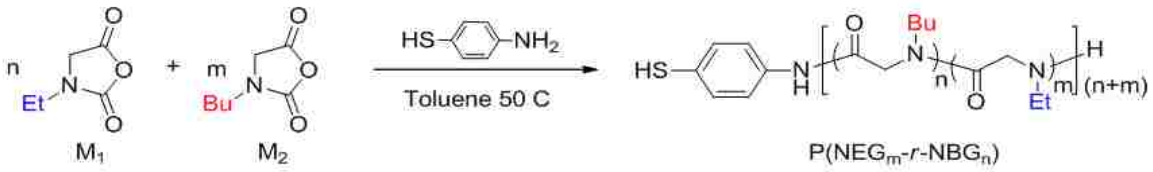

Scheme 4.1 Copolymerize *N*-ethyl *N*-carboxyanhydride and *N*-butyl *N*-carboxyanhydride with initiator 4-aminothiophenol.

4.2.3 Preparation Nanopatterned Poly[(*N*-ethyl glycine)$_{32}$-*r*-(*N*-butyl glycine)$_{17}$] by Surface Thiol-ene Click Reaction

Copolymer (10 mg) and photoinitiator Irgacure (10 mg) were added in 2 mL of THF. Si substrate with UTS patterns was immersed in the THF solution and placed under UV lamp (Xenon Arc Lamp) overnight (18 h). Substrate was then rinsed with THF and sonicated, first in THF and second in ethanol. The sample was characterized with AFM the contact-mode in water.

4.2.4 Thermoresponsive Study of Nanopatterned Copolypeptoids using *in situ* AFM

A sample stage with a water-filled liquid cell is used to hold sample of patterned copolypeptoids on Si wafer. A temperature controller is connected with the sample stage which can adjust the temperature of the sample plate, as well as the sample. The polymer nanopillar height and morphology changes of the copolypeptoids with the increase of temperature were tracked with *in situ* AFM.

4.3 Result and Discussion

The key steps of preparing nanopatterned random copolypeptoid P(NEG$_{32}$-*r*-NBG$_{17}$) on Si substrate are illustrated in Figure 4.1. First, periodically ordered nanopores within a thin film of octadecyltrichlorosilane (OTS) were prepared to provide nano-confined reactive sites through

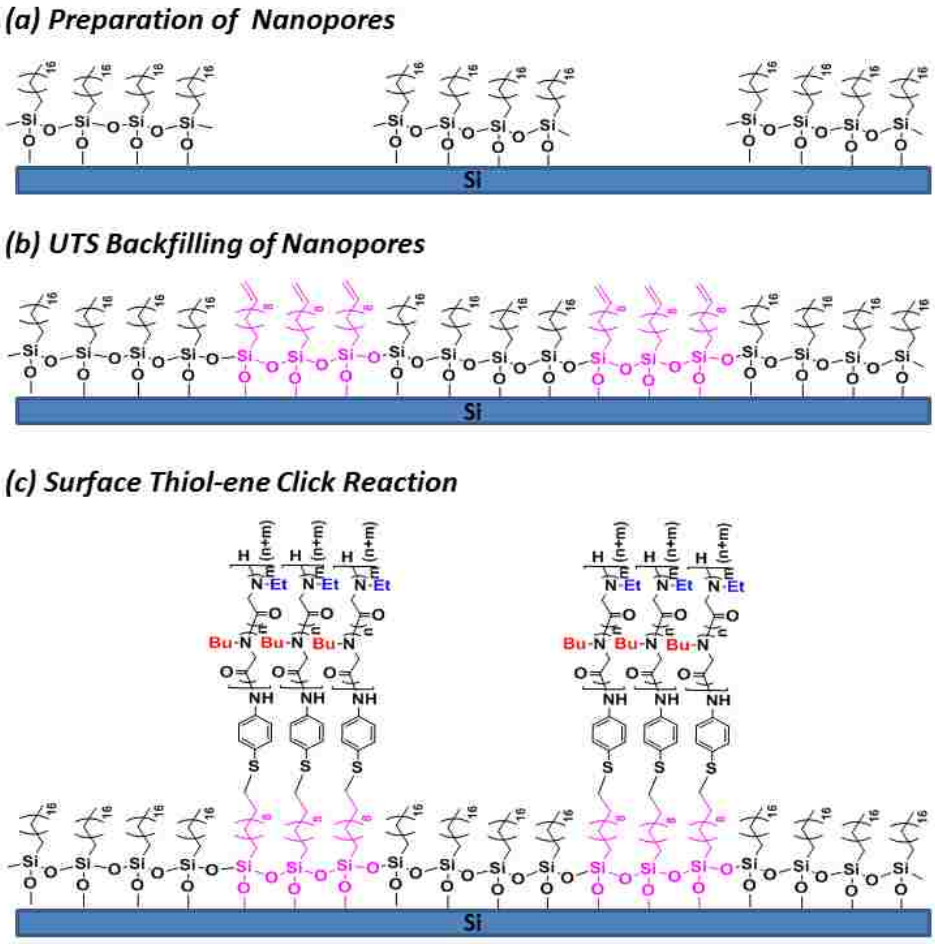

Figure 4.1 Steps for preparing nanopatterns of thermo-responsive copolypeptoids. (a) Nanopores within a film of OTS were prepared by particle lithography and silane immersion. (b) Backfilling of UTS into nanopores to form reactive sites for localizing random copolypeptoids. (c) Linear poly[(*N*-ethyl glycine)$_{32}$-*r*-(*N*-butyl glycine)$_{17}$] copolymers, P(NEG$_{32}$-*r*-NBG$_{17}$), immobilized at UTS sites through thiol-ene click reaction.

silane hydrolysis and condensation reaction with hydroxylated surface and subsequent removal of silica mesospheres (Figure 4.1a). Second, 10-undecenyltrichlorosilane (UTS) was backfilled into

the nanopores which are the locations of bare Si substrate (Figure 4.1b). Third, the chemically patterned surface was immersed in a tetrahydrofuran (THF) solution containing a thiol end-group functionalized P(NEG_{32}-*r*-NBG_{17}), a random copolypeptoid product of reaction shown in Scheme 4.1. The thiol-ene click reaction occurred between the vinyl group of UTS and thiol end group of polypeptoid upon the irradiation of UV light to form nanopatterned linear random copolypeptoids (Figure 4.1c).

Patterned nanopores within a film of OTS were prepared with particle lithography and silane immersion with a previous reported method in our group (Appendix Figure C1).[206] The thin film of OTS served as a polymer deposition resist. The second silane, UTS, filled the nanopore areas to form patterned reactive sites for polymer deposition (Figure 4.2). The hexagonal array of brighter dots (UTS sites) within a darker background (OTS thin film) is shown with a 7 × 7 μm^2 area topography view (Figure 4.2a). The 211 UTS nanopillars shown in the 7 × 7 μm^2 area can

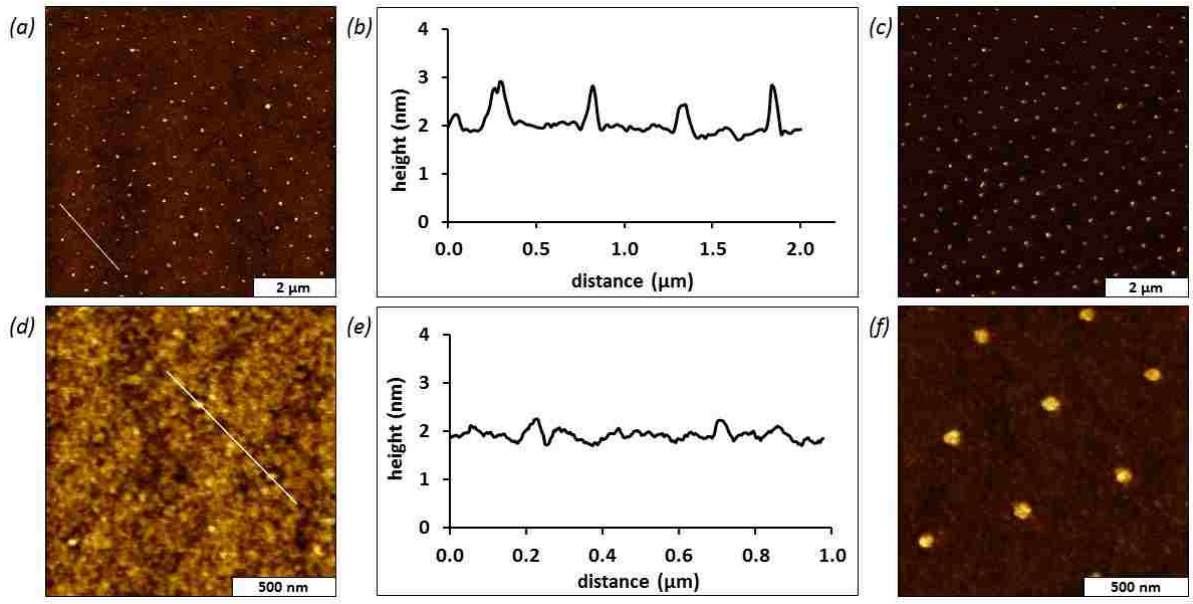

Figure 4.2 Selective backfilling of UTS into OTS nanopores. (a) 7 × 7 μm^2 topograph. (b) Cursor profile for the line in a. (c) Lateral force image of a. (d) Zoom-in view. (e) Cursor profile for the line in d. (f) Corresponding lateral force image of d.

scale up to ~10^8 nanopillars per cm^2, which demonstrates that particle lithography is high throughput method to generate nanopatterns. The nanopillars of UTS have an average height of 1.1 ± 0.6 nm. A cursor line over four selected UTS nanopillars reveals that the height distribution range is 0.7-1.2 nm and the distance between two adjacent UTS pillars is ~ 500 nm, which was determined by the size of the removed silica mesospheres (Figure 4.2b). The chemistry difference between methyl group of OTS and vinyl group of UTS is clearly distinguishable on the lateral force image (Figure 4.2c). A 1.4 × 1.4 μm^2 topograph cannot clearly differentiate the pattern because there is no noticeable height difference between the OTS background and the UTS nanopillars (Figures 4.2d and 4.2e). However, the chemistry difference between methyl and vinyl terminal groups is more discernible in the simultaneously acquired lateral force image, as the brighter areas indicate UTS sites and darker background indicates the OTS resist (Figure 4.2f).

The 2-D chemically patterned surface served as a good foundation for further polymer deposition. This foundation was amplified at the patterned reactive sites to a 3-D pattern by thiol-ene click reaction between the thiol end-groups of P(NEG_{32}-*r*-NBG_{17}) and the vinyl groups of UTS (Figure 4.3). The patterned P(NEG_{32}-*r*-NBG_{17}) nanopillars are shown in the wide view topograph with average height of 8.1 ± 2.7 nm (Figure 4.3a). The periodicity and morphology of the

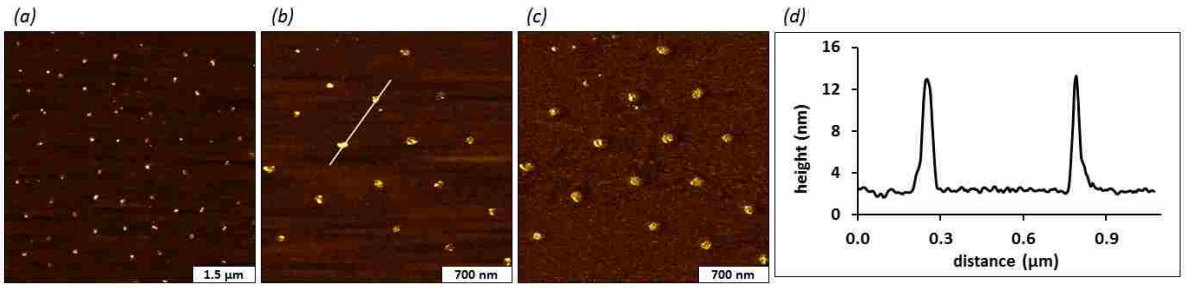

Figure 4.3 Copolypeptoids polymer nanopillars after thiol-ene click reaction. (a) 6 × 6 μm^2 topograph acquired by contact-mode AFM. (b) Close-up view. (c) Simultaneously acquired lateral force image of b. (d) Cursor profile for the line in b.

copolypeptoid nanopillars on surface are shown in the 2.5 × 2.5 μm^2 topography view (Figure 4.3b). The chemistry difference between polypeptoid nanopillars and OTS background can be clearly seen in the corresponding lateral force image (Figure 4.3c). Two selected polymer nanopillar areas (see cursor line in Figure 4.3b) have measured a height of ~11 nm and at a distance of ~540 nm (Figure 4.3d). The inhomogeneity of a single polypeptoid nanopillar site in the lateral force image indicates that there are many polymer brushes at one nanopore site with an upright orientation.

The thermo-responsiveness of the linear random copolypeptoid P(NEG_{32}-*r*-NBG_{17}) was investigated using *in situ* AFM in aqueous media after patterning of the polymer brushes on Si surface. As the temperature of the liquid media surrounding the Si substrate was ramped at 5 C increments, the height of the polypeptoid nanostructures appeared to change. The results at three selected temperatures (25 C, 45 C and 65 C) are shown in Figure 4.4 and more temperature studies are shown in Appendix C (Figure C2). The heights decrease of two particular polymer brush sites were monitored and indicated in the topographs (Figures 4.4a, c and e) and cursor profiles (Figures 4.4b, d, and f). At 25 C, the heights of the two nanostructures vary (Figure 4.4b), which is according to the original size of the nanoholes within OTS. The polymer brushes collapsed upon heating, as indicated by a nanopillar height decrease from more than 10 nm (25 C) to less than 3 nm (65 C).

The LCST behavior of the copolypeptoid was also studied with the turbidity assay using untethered copolymer in aqueous solution. The onset cloud point temperature (T_{cp}), the temperature measured at 90% transmittance, is 45 C for a solution of copolypeptoid (1 mg•mL^{-1} in water) (Appendix Figure C3). Changes in the composition of copolypeptoids can be used to adjust the cloud point temperature within the range of 20-60 C. In aqueous solution, the unbound

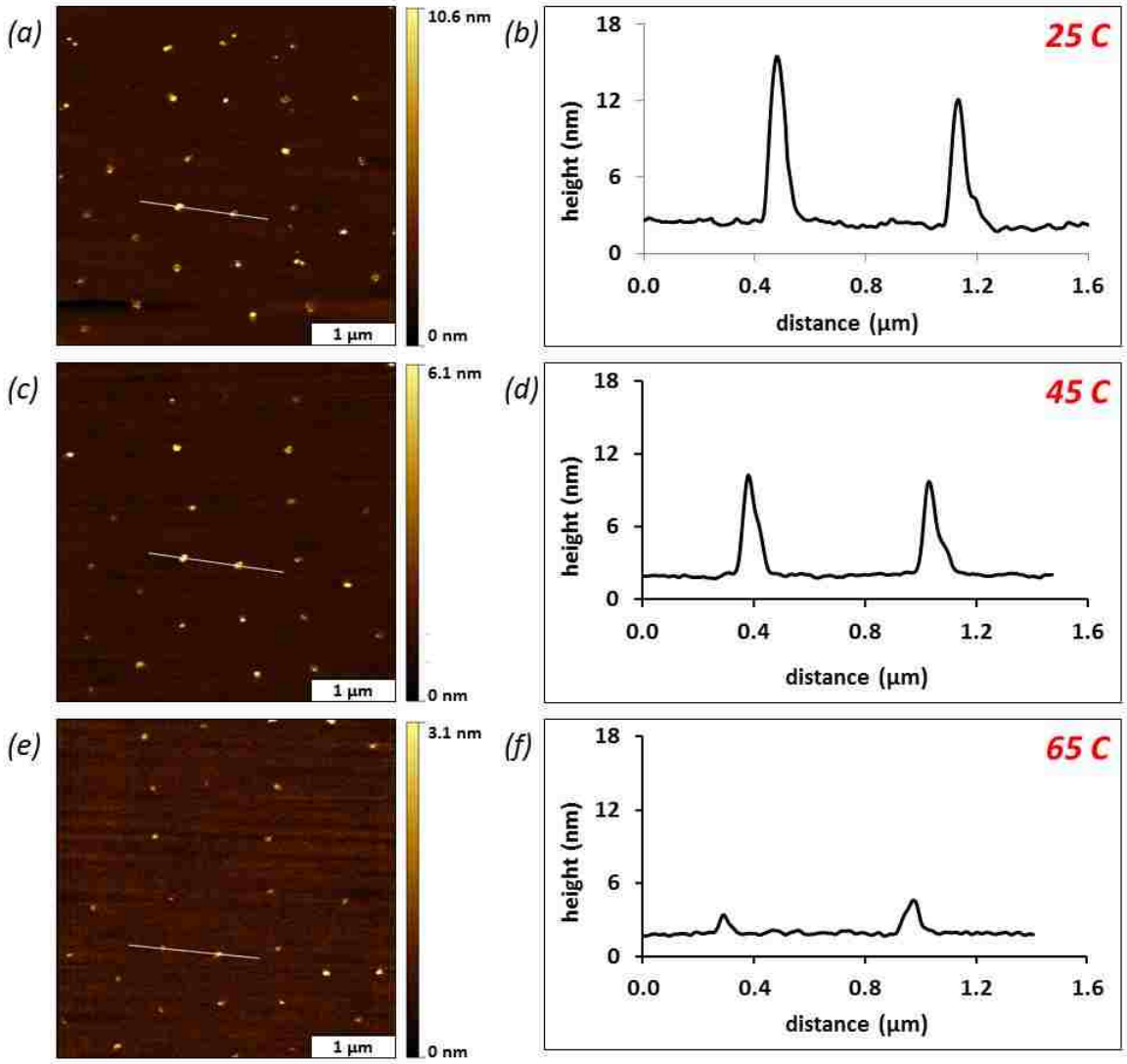

Figure 4.4 *In situ* thermo-responsive study of nanopatterned random copolypeptoids, P(NEG$_{32}$-*r*-NBG$_{17}$). All of the AFM images have scan size 4 × 4 µm^2. Two particular spots were tracked during the heating process. (a) Topograph acquired at 25 C. (b) Cursor profile for the line in a. (c) Topograph obtained at 45 C. (d) Height profile for the line in d. (e) Topography image acquired at 65 C. (f) Cursor profile for the line in g.

P(NEG$_{32}$-*r*-NBG$_{17}$) is solvated at room temperature, as evident by the 100% transmittance, and as the temperature is increased to the onset T_{cp}, the solution becomes turbid as the copolymers collapse and aggregate. This physical phenomenon (copolymer collapse/aggregation) can be clearly seen with the surface patterned copolypeptoids with *in situ* AFM imaging.

A proposed mechanism for the thermo-responsive properties of copolypeptoids nanostructures is illustrated in Figure 4.5. At ambient temperature, the water soluble polymer brushes are fully extended in aqueous media due to hydrogen bonding between polymer chains and water molecules (Figure 4.5a). Upon heating, the hydrogen bonding is interrupted, resulting in the collapse of the polymer brushes, which ultimately aggregate and condense on surface to form compact structures (Figure 4.5b). The effects of heating and cooling are reversible. If the polymer dissolves in aqueous solution, upon cooling, the polymers become hydrated, disrupting the aggregates, and generating a fully extended polymer chain. If the polymer is immobilized on a surface, turning from the collapsed form to the extended form appears to be a much slower process than unbound polymer (approximately 1 h is need in our experiment).

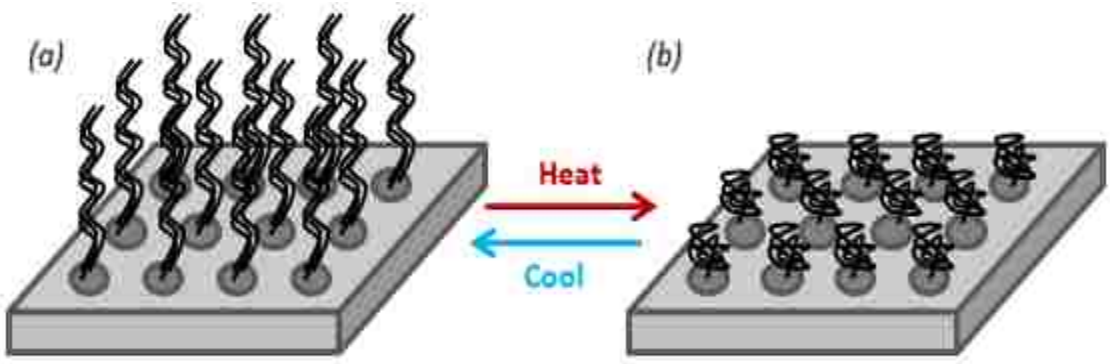

Figure 4.5. Proposed mechanism of the thermo-responsiveness of patterned copolypeptoids. (a) Free-standing polymer brushes in aqueous solution at room temperature. (b) Collapsed polymer brushes on surface at elevated temperature.

The thermo-responsiveness of eight polymer brush sites was tracked (Figure 4.6). With an increase in temperature, the heights of the eight polymer brush sites decrease. At the starting temperature (25 C), the polymer brushes have heights ranging from 8.1 nm to 16.2 nm. At the final temperature (80 C), nearly all of the polymer brush sites have height of 1-1.5 nm, which means

the length of the polymer brush in our experiment does not influence the trend of decreasing in height of the random copolypeptoid P(NEG_{32}-*r*-NBG_{17}) with increasing in temperature.

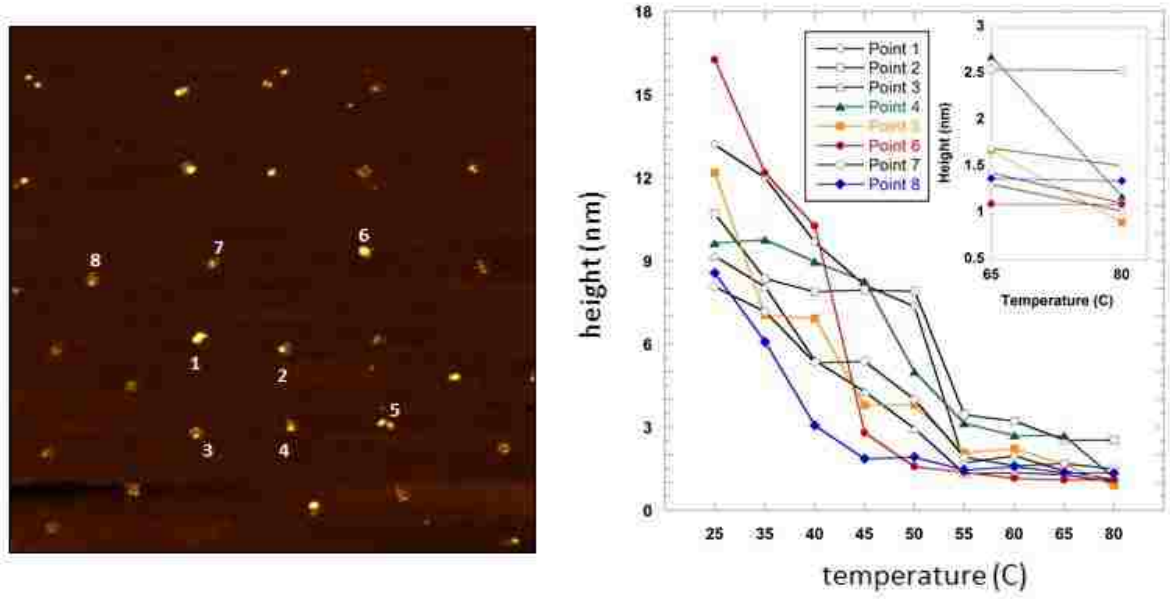

Figure 4.6 Temperature-dependent changes in height studied *in situ* with AFM. (left) Example topograph at 25 C. The heights of eight polymer brush sites were tracked. (right) Measurements for height decrease with rising temperature (C).

4.4 Conclusion

In conclusion, to the best of our knowledge, for the very first time, the thermo-responsiveness of patterned polymer brushes at the nanoscale was studied *in situ.* Thiol-ene click chemistry turned out an efficient way to attach functionalized linear polymer, in our case, the random copolypeptoid poly[(*N*-ethyl glycine)$_{32}$-*r*-(*N*-butyl glycine$_{17}$)], or P(NEG_{32}-*r*-NBG_{17}), to the substrates. The surface changes at nanoscale can be sensitively detected with AFM when increasing temperature to 35 C. However, the transmittance change only can be noticed after 45 C at eh onset cloud point temperature.

CHAPTER 5. A REVIEW ON FORCE MODULATION MICROSCOPY AND THE CAPABILITY OF NANOMECHANICAL MAPPING OF SURFACE ELASTIC AND VISCOELASTIC PROPERTIES

5.1 History of Force Modulation Microscopy (FMM)

Since its invention in 1986, atomic force microscopy (AFM) has been used in a broad range of fields for surface characterizations.[1] Force modulation microscopy (FMM), one of over 50 possible modes of AFM, was invented in 1991 by Maivald and Hansma et al. to study the carbon fiber and epoxy composite.[14]

With FMM, local mechanical properties of a sample surface can be acquired along with topography by imposing a z axis vibration between tip-sample contact during contact-mode imaging. Dynamic response of the sample to an increased or decreased load is monitored. In the first report of FMM, variations in the local elasticity were differentiated on a composite surface at the nanoscale.[14] The sample was placed on a piezoelectric translator and the AFM tip was raster scanned across the sample surface in contact-mode with constant force. At the same time, a z axis vibration of 25 nm was introduced to the sample through the z piezoelement. The frequency of the z axis vibration was tuned so that it did not interfere with the resonance frequencies of the feedback loop and minimized the coupling with the electronics. The cantilever deflection is larger on the harder regions compared with softer regions during FMM, because more pressing energy from the cantilever can be absorbed by the soft regions and more deformation was encountered by the soft regions. Clear contrast was acquired in the amplitude image and the elasticity modulus of carbon fibers and epoxy were estimated.

Due to the relative high forces (10^{-7}-10^{-6} N) applied during contact-mode AFM, images of soft materials suffer from insufficient contrast and quality. The author who did the earliest work of FMM realized that: since soft materials like biological samples are usually deposited on hard substrates for AFM work, the FMM increases the potential of imaging soft materials because of

the success of characterizing carbon fiber and epoxy composite. A large variety of soft materials were studied with FMM such as polymers and proteins over the past 20 years because the great advantage of using FMM to image soft materials on hard surfaces.[61-65, 73, 81, 208-211]

5.2 Instrument Set-up of FMM

There are four instrumental configurations for force modulation microscopy based on either tip or sample vibration in the z axis when the system is operated in contact-mode. The most common design is shown in Figure 5.1 where the sample is placed directly on top of an xyz scanner. Actuation of the z piezoelement of the scanner by applying sinusoidal voltage causes the sample to vibrate for tip displacements of a few nanometers in the z direction perpendicular to the scanning plane.[60, 62, 77-80, 82] A modulation of the vertical sample position leads to a modulation of the force between tip and sample. This force modulation results in an indentation of the sample depending on its elasticity. The modulation frequency is chosen to be 3-4 orders of magnitude larger than the scan frequency to avoid the cutoff frequency of the feedback loop (~0.5 kHz), the resonance

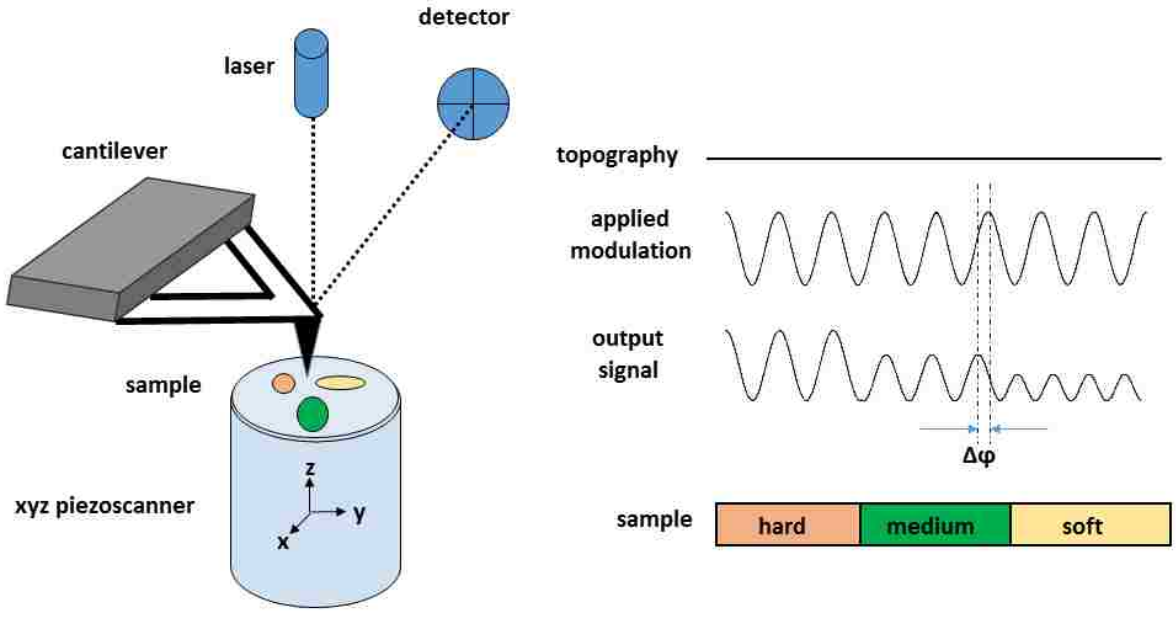

Figure 5.1 Instrument setup and operating principle of force modulation microscopy.

frequency of the piezoscanner (~8 kHz) and the cutoff frequency of the photodetector (~1 MHz).[62] Soft probes with spring constants less than 1 N/m are usually used in FMM studies because of the possibility of plastic deformation (wear) of the polymer surface.[84] The oscillation amplitude is kept small so that the topography image will not be degraded by vibration at tip-sample contact.

A flat surface with three regions of varying elastic moduli is shown as a proof-of-concept in Figure 5.1. From the FMM topograph, a flat surface without any contrast will be resolved. Comparing to the input sinusoidal wave signal, the output signal has an amplitude change and a phase angle shift which are detected by two lock-in amplifiers and translate to FMM amplitude and FMM phase images. Careful comparisons between FMM topographs with contact-mode topographs have been made and no significant differences were found.[83]

In the second instrument configuration for FMM, a cantilever holder equipped with bimorph piezoelements, which can actuate the tip as it is pressed against the sample, is used.[63, 74, 83-84] The bimorph piezos can oscillate the cantilever near resonance frequency during tapping-mode and depress the tip into the sample surface during FMM.[63] Therefore, two modes are enabled using the same set-up.

The third way to accomplish force modulation imaging is using a magnetic field to drive the vibration of a tip or tip-holder assembly.[85-88, 212] In Yamamoto's work, samples were mounted on a piezoelectric tube scanner, inside of which a coil for an electromagnet was fixed. A piece of samarium cobolt magnet was glued at the end of the backside of the cantilever.[85] In Pietrement's work, the solenoid was placed around the piezotube and a small spherical magnetic particle of LaNdFeB alloy was glued on the backside of the cantilever just above the tip.[213] Indirect magnetic modulation (IMM), invented by Li et al., is another instrument configuration for FMM.[86] The

entire tip assembly, containing ferromagnetic materials, is induced to vibrate with the flux of an external AC electromagntetic field, generated by a wire coil solenoid underneath the sample plate.

The fourth design is a scan-by-tip AFM configuration, the z axis vibration is applied to the sample. Troyon and Hazotte et al. placed a transducer underneath the sample, which is a 0.5 mm thick and 8 mm round disk.[76] Lu and Garno et al. embedded a piezoactuator inside a machined polycarbonate sample stage to generate the z axis vibration by applying AC current to the piezoelement.

5.3 Advantages of FMM

Force modulation can be used for identifying and mapping differences in stiffness or elasticity, evaluating materials' homogeneities,[85, 214] and studying variations in crystallinity,[6] polymer phase separation, surface arrangement and distribution.[80, 215-217] Mechanical properties of the surfaces are probed continuously over extended areas instead of at scattered individual points as in force-distance curves and load-indentation measurements.[83] Asif and Colton et al. combined nanoindentation and force modulation microscopy together to acquire nanoscale mechanical properties.[218-219] In force-distance curve measurement, the probe is not perfectly perpendicular to the sample due to the 10-15° tilt of the cantilever. Therefore, the load has a tangential component in the direction parallel to the cantilever arm, which induces error measurements.[213] To overcome the scanning angle problem in FMM, Overney and Fijihira et al. added an additional piezo plate between the piezoscanner and sample so the z modulation direction can be freely adjusted within 90° by tilting the piezo plane.[78]

Force modulation microscopy can also quantify information about sample surfaces such as Young's modulus and elasticity.[75-76, 79, 213] An example of calculating the spring constant of sample surface is given here.[79] For FMM when the sample is modulating in the z axis on top of a piezotube,

the cantilever deflection ΔZ_c caused by the sample modulation ΔZ_p was measured sensitively by a lock-in amplifier. Consequently, the sample is deformed by the amount

$$\Delta Z_{eff} = \Delta Z_p - \Delta Z_c \quad \text{(Equation 5.1)}$$

ΔZ_c will be smaller on softer and larger on harder surfaces. With a cantilever having spring constant K_c and a sample spring constant K_s, the variation of the force acting on the surface is given by

$$\Delta F = K_s (\Delta Z_p - \Delta Z_c) = K_c \Delta Z_c \quad \text{(Equation 5.2)}$$

Rearrangement of the Equation above will result in the spring constant of the sample

$$K_s = K_c \left(\frac{\Delta Z_p}{\Delta Z_c} - 1 \right)^{-1} \quad \text{(Equation 5.3)}$$

This K_s value directly gives information about surface elastic properties.

To determine the Young's modulus of the sample surface, the Hertz model is used to describe the deformation of the tip-sample contact.[75] If an elastic spherical tip is in contact with a flat, elastic sample, the penetration depth d of the tip into the sample is given by

$$d = \left(\frac{9W^2}{16E'^2 R} \right)^{1/3}, \quad \text{(Equation 5.4)}$$

where

$$\frac{1}{E'} = \frac{(1-\nu_t^2)}{E_t} + \frac{(1-\nu_s^2)}{E_s}, \quad \text{(Equation 5.5)}$$

W is load, R is tip radius, E is Young's modulus, ν is Poison's ratio, and the subscripts t and s stand for the tip and sample. Differentiating Equation 5.4 gives the load-displacement curve as a function of applied load

$$\frac{\partial W}{\partial d} = (6E'^2 RW)^{1/3} \quad \text{(Equation 5.6)}$$

If considering the static force, W_0, to cause a static sample penetration d_s^0, then the oscillation of the z piezo can be viewed as causing a small change, δW. to the applied static force resulting in a small change in the penetration, δd.

$$\frac{\delta W}{\delta d} = (6E'^2 R W_0)^{1/3} \quad \text{(Equation 5.7)}$$

$$\delta W = k_c\, d_c \quad \text{(Equation 5.8)}$$

$$\delta d = d_s = d_b - d_c \quad \text{(Equation 5.9)}$$

$$W_0 = k_c\, d_c{}^0 + W_a \quad \text{(Equation 5.10)}$$

where d_c is cantilever deflection, k_c is cantilever spring constant, d_s is sample penetration depth, d_b is the oscillation of the bimorph piezo, W_a is adhesion force, and the static force W_0 applied by the cantilever can be related to the mean deflection of the cantilever $d_c{}^0$. By applying Equations 8-10 to Equation 7 a quantitative measurement of Young's modulus is made:

$$E' = [6(\frac{d_b - d_c}{k_c\, d_c})^3 \mathrm{R}(k_c\, d_c{}^0 + W_a)]^{-1/2} \quad \text{(Equation 5.11)}$$

5.4 Studying Self-assembled Monolayers (SAMs) Using FMM

The surface elastic and viscoelastic properties of self-assembled monolayers (SAMs) are widely studied with FMM. Some FMM work in SAM systems are summarized in Table 5.1. Bi-functional surfaces of Langmuir-Blodgett (LB) film comprised of two kinds of molecules were used as samples to probe the elasticity and viscoelasticity using FMM. Most of the systems were investigated using the z piezoelement to generate the z axis vibration of the samples. Either qualitative comparison between two components' elasticities or quantitative information about the Young's modulus were acquired. Vibration amplitude of a few nanometers was used, which is much smaller than tapping-mode. The vibrational frequency was chosen to be much higher than imaging speed but avoid interference with the feedback loop. Commonly a cantilever with a small spring constant (<1 N/m) is used.

Table 5.1 Examples of SAM systems using FMM as a tool to study the surfaces.

Sample	Operating system	Information acquired	Driving amplitude	Driving frequency (kHz)	Cantilever spring constant	Ref
Langmuir Blodgett film of $C_{19}H_{39}COOH$ and $C_9F_{19}C_2H_4$-O-C_2H_4COOH	Sample mounted on xyz scanner	A higher Young's modulus on the hydrocarbon domains	2-5 nm	11-19	0.17 N/m	[220]
Langmuir Blodgett film of $C_{21}H_{43}COOH$ and $C_9F_{19}C_2H_4$-O-C_2H_4COOH	Sample mounted on xyz scanner	Difference in elasticity is 0.1 GPa	1 nm	4	0.25 N/m	[78]
Langmuir Blodgett film of $C_{21}H_{43}COOH$ and $C_9F_{19}C_2H_4$-O-C_2H_4COOH	Sample mounted on xyz scanner	Difference in elasticity is 0.1 ± 0.03 GPa	2-5 nm	11-19	0.17 N/m	[215]
Mixed monolayer of octadecyltrichlorosilane (OTS) and [2-(perfluorooctyl)ethyl] trichlorosilane (FOETS)	Sample mounted on xyz scanner	Crystalline OTS has a higher modulus than amorphous FOETS	0.89 nm	5	0.022 N/m	[80]
Patterned monolayer of alkanethiol	Nanoscope lll	C18 surface is stiffer than C7	1-100 mV	8	0.02-0.7 N/m	[221]
Octadecyltriethoxysilane monolayers	Sample mounted on xyz scanner	Measurements taken in liquid more accurately reflect the viscoelasticity	1-54 nm	12-45	0.1 N/m	[89]
Langmuir Blodgett film of L-α dimyristoylphosphatidylcholine (DMPC) and quercetin palmitate (QP)	Nanoscope multimode	QP domains are softer		8	20-100 N/m	[222]
Nanostructures of actadecanthiols inlaid in decanethiol SAMs	Sample mounted on xyz scanner	$E^* = 0.014 \ln(x) + 0.859$ x: size of the nanostructures			0.1 N/m	[223]
Patterned triethylene glycol mono-11-mercaptoundecyl ether (EG_3-thiol)	Modified Asylum MFP-3D	Young's modulus of the EG_3-thiol on gold is 30 GPa		20	0.7	[224]

An example of using FMM to study the dynamic viscoelastic response of phase separated SAM system is shown in Figure 5.2.[80] Octadecyltrichlorosilane (OTS) and [2-(perfluorooctyl)ethyl]trichlorosilane (FOETS) (50/50, mol/mol) mixture was spread on a water surface and transferred on Si using an upward drawing technique. The silanes were hydrolyzed on the water surface and the hydroxyl groups were polymerized to form Si-O-Si bridges between silanes. After transferring to the Si substrate, the silanes bound to the Si surface covalently to form a phase separated silane monolayer of OTS and FOETS.

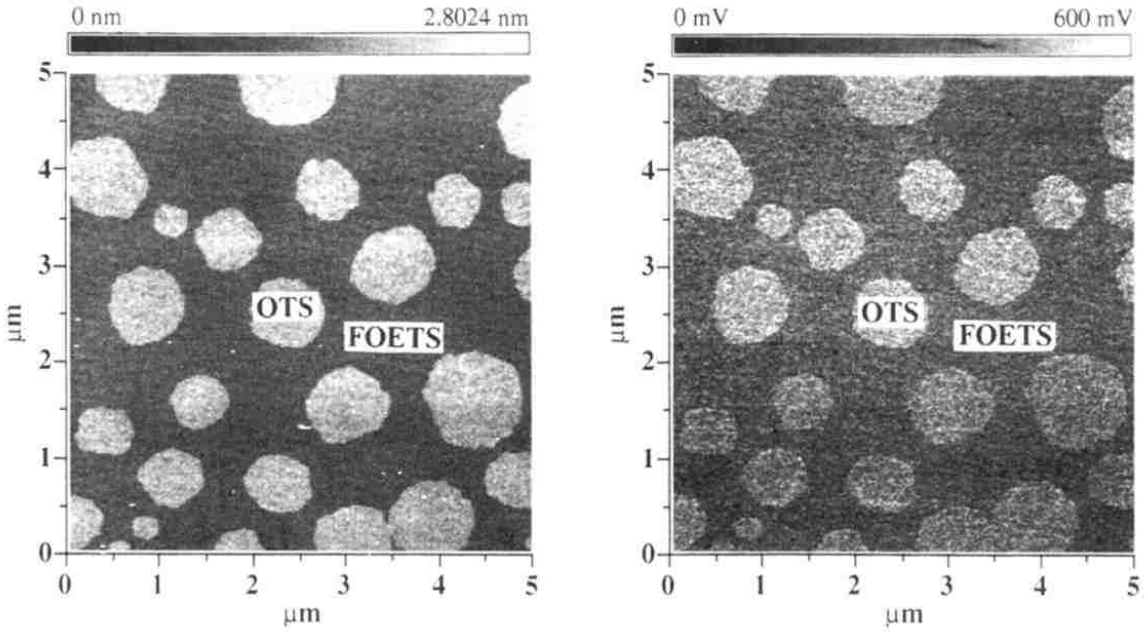

Figure 5.2 A mixed monolayer of OTS/FOETS (50/50, mol/mol) studied with FMM at frequency of 5 kHz and z axis modulation of 0.89 nm. (left) Topography and (right) elasticity images. Reprinted with permission.[80] Copyright 1994 American Chemical Society.

The sample shown in Figure 5.2 is mounted on an xyz piezoscanner. The modulation of the vertical sample position leads to an indentation of the tip against the sample depending on its viscoelasticity. The phase separated OTS and FOETS pattern can be viewed in the topography and elasticity images and were acquired using FMM at a driving frequency of 5 kHz and a vibration amplitude of 0.89 nm. Circular flat-topped OTS domains are surrounded by a flat FOETS matrix

with a height difference of 1.3 nm, which can be seen from the topography image. From the elasticity image, the bright areas correspond to the higher modulus region. Areas of OTS have bright contrast with high modulus because OTS SAM is in a crystalline state at 293 K.

In FMM amplitude and phase channels, contrast of images sometimes vary or flip with the changes of experiment conditions, such as vibration frequencies (Figure 5.3).[89] In this example, octadecyltriethoxysilane (OTE) SAM was prepared on mica. By increasing the imaging force in a 150×100 nm^2 scan area and removing away the OTE molecules, a nanoscopic mica area inlaid in the OTE SAM was fabricated. Force modulation images were taken from 10 to 50 kHz, at 1 kHz intervals. Six representative frequencies were chosen to show the frequency-dependent property of FMM. Even though the Young's modulus for mica is 130 GPa and less than 1 GPa for OTE, the mica region should appear darker in contrast for the amplitude channel because 2-4 layers water film is on top of mica under the experimental condition (room temperature and 50% humidity) as shown in Figures 5.3b, c and f. The water molecules formed a capillary neck when the tip was scanning and dampened the tip's z axis vibration in FMM. However, a contrast flip can be seen in Figures 3a, d and e. The authors found out that at conditions where the driving frequency overlaps with the resonance of tip-mica contact, a contrast flip was observed. However, the authors operated FMM in liquid media such as 2-butanol and they found out the contrast in amplitude and phase channels are more consistent. Measurements taken in liquid media accurately reflect the viscoelasticity of samples because adhesion forces between the tip and sample are minimized.

Contrast in FMM amplitude and phase images can be dominated by factors other than simple elasticity, such as the driving frequency,[225] imaging media,[89, 226] tip-sample contact area,[221] amplitude of oscillation,[227] and the shape and stiffness of the tip.[72, 217] Therefore, measurements from FMM can provide surface information about heterogeneities in stiffness rather than absolute

or relative values.[84, 228] However, it is possible to operate FMM in regions that the image contrast reflect the relative elasticities of different components by tuning the experimental conditions.

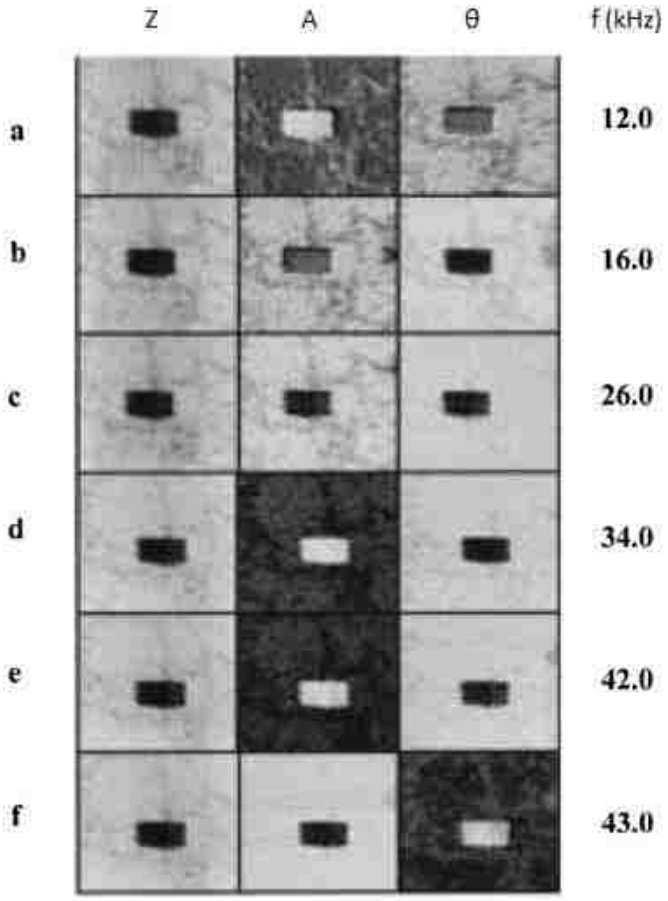

Figure 5.3 An octadecyltriethoxysilane monolayer with nanoshaved rectangular at center on mica investigated with FMM. Topography (Z), amplitude (A), and phase (θ) images from six driving frequencies were shown. The image sizes are all 500 nm^2 and the nanoshaved area has size 150 x 100 nm^2. The z axis modulation is 9 nm. Reprinted with permission.[89] Copyright 1999 American Chemical Society.

5.5 Investigating Polymeric Materials Using FMM

Polymeric composites, blends, individual chains and block copolymers were studied with FMM and some of the work has been summarized in Table 5.2. Samples, substrates, FMM set-ups, information acquired and experimental conditions are all discussed in detail.

Table 5.2 Examples of polymeric systems using FMM as a tool to study the surfaces.

Sample	Operating system	Information acquired	Driving amplitude	Driving frequency (kHz)	Cantilever spring constant	Ref
Epoxy and carbon fiber composite	Stylus bottom xyz scanner	Modulus 2.1 x 10^{11} Pa for carbon fiber and 7.0 x 10^{10} Pa for epoxy	25 nm	5	0.6 N/m	[14]
Polymeric diamino-diethyl-ene glycol-pentacosadiynoic acid (DPDA) monolayer	Sample mounted on xyz scanner	Polymeric DPDA film is softer than the substrate	6 nm	15.6	0.064 N/m	[77]
LB film of Poly(diamino-diethylene glycol-pentacosadiynoic)	Magnetic actuated z axis tip vibration	Spring constant of the film is 6 N/m	0.3 nm	5-44		[229]
Individual polystyrene molecules	Sample mounted on xyz scanner	Thiol-terminated polystyrene is softer than the dodecanethiol	0.1 nm	10	0.1 N/m	[79]
Phase separated polystyrene and poly(vinyl methyl ether) (PS/PVME) blend film	Sample mounted on xyz scanner	Mechanical tan $\delta = 0.25$ for PVME and 0.1 for PS	1.2 mV	5	0.022 N/m	[80]
Toughened polypropylene/(ethylene propylene) (PP/EP) copolymer resins	Sample mounted on xyz scanner	PP matrix is much stiffer than the EP modulus	1 nm	2	10 N/m	[61]
Polystyrene-polyethyleneoxide (PS/PEO) blend surfaces	Sample mounted on xyz scanner	PEO is 7% softer than PS	1 nm	5	0.75 N/m	[62]
Poly(dimethylsiloxane) (PDMS) film	Function generator	Viscosity 430 ± 40 cP	1 nm	10	40 N/m	[230]
Industrial polymer blends	Cantilever holder was equipped with bimorph piezo	Polypropylene is stiffer than ethylene propylene; Exxpro 90-10 is stiffer than Budene 1207	0.1-1.2 V	11	0.4-1 N/m	[63]
Polymer blend of poly-2-vinylpyridin (P2VP) and polytertbutylmethacrylate (PtBMA)	High frequency piezoelectric transducer	The adhesive force of PtBMA is larger than P2VP	3 V	233.1	0.75 N/m	[231]

A composite material consisting of carbon fibers embedded in an epoxy matrix was investigated using FMM (Figure 5.4).[6] A bimorph piezo set up, which was introduced earlier, was used. The height variation of the surface is 0-150 nm for the topography image, and 0-1 nm for the amplitude image. The contrast of the topography image is not as sharp as the amplitude image. More pronounced contrast between the hard carbon fiber (brighter: higher amplitude) and soft epoxy matrix (darker: lower amplitude) is shown in the oscillation amplitude image.

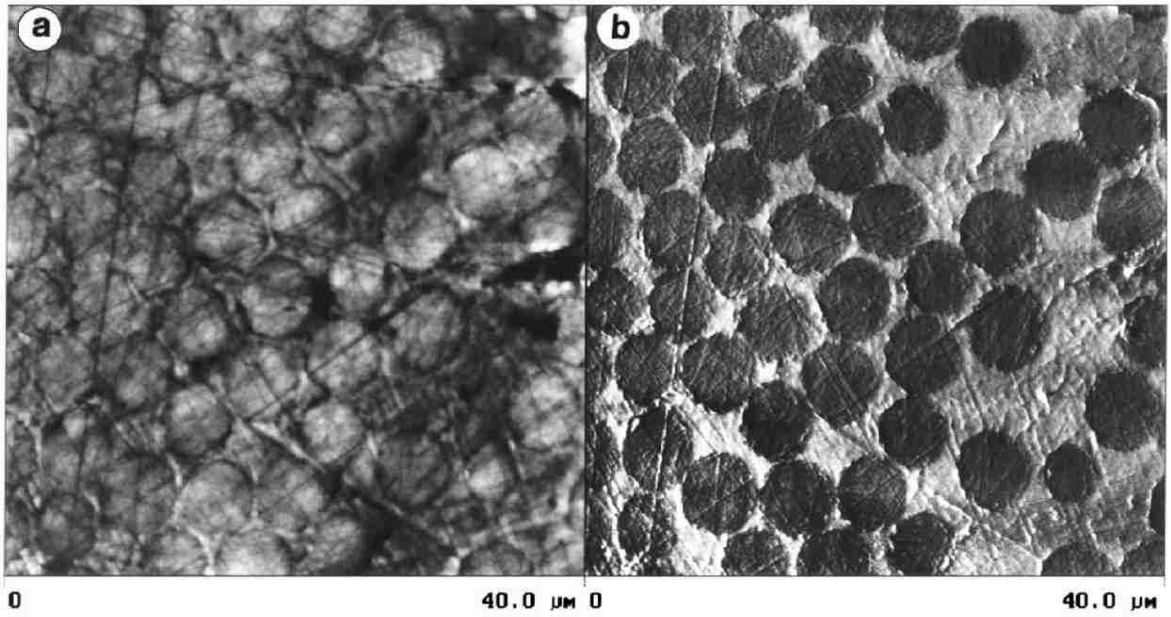

Figure 5.4 Composite materials of carbon fibers embedded in epoxy matrix imaged with FMM. (a) Topography and (b) amplitude images. Reprinted with permission.[6] Copyright 1997 Annual Reviews.

Free-standing gels containing entangled fibrils, which were formed by block copolymer poly(*N*-methyl glycine)$_{100}$-*b*-poly(*N*-decyl glycine)$_{10}$ or *c*-PNMG$_{100}$-*b*-PNDG$_{10}$ were investigated using FMM (Figure 5.5).[232] The height range is 0-157 nm in the topography image which is the reason that large polymer aggregates can be seen but not the fibrillar structures in the background. However, using FMM at driving frequency of 163.8 kHz, both polymer aggregate and fibrils are clearly resolved in the amplitude and phase channels. Since the fibers are crystalline-like materials

and tend to be harder than the surrounding gel, the fibers appear brighter in contrast in the amplitude channel.

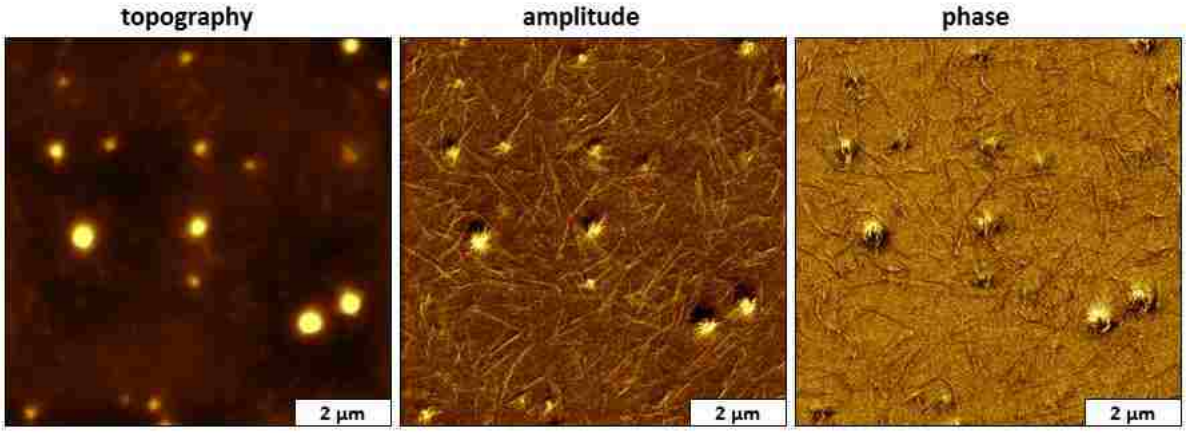

Figure 5.5 Polymeric gel containing fibers viewed from topography, amplitude and phase images acquired with FMM at vibration frequency of 163.8 kHz.

Another interesting FMM study on polymer blends with polystyrene (PS: molecular weight is 19600 g/mol) and polyethyleneoxide (PEO: molecular weight is 100000g/mol) is shown in Figure 5.6. The solution of PS and PEO blended with 1:1 weight ratio in benzene was spin coated on mica. The sample was annealed at 90 C for 24 h before FMM measurement. During FMM, the z axis oscillation of the sample was achieved by applying sinusoidal voltage to the vertical piezo scanner on which the sample was fixed. The imaging force for phase separated PS-PEO was 6 nN in the surrounding area and 50 nN in the square shown in Figure 5.6. Scratches are noticed on both PS and PEO areas when imaging force was increased to 50 nN. Crystallized PEO should exhibit spiral or layered structures, which means taller structures in Figure 5.6a are PS and shorter features are PEO. The corrugation amplitude is 15 nm for PS and 15-30 nm for PEO. Outside of the central area in Figure 5.6b, the response of the cantilever is found to be about 7% smaller on PEO than on PS, which means PEO is softer. In the central area, a large elasticity change is noticed that PEO

regions become stiffer after experiencing a large-force scanning and the difference in cantilever response decreased to 1-2 %.

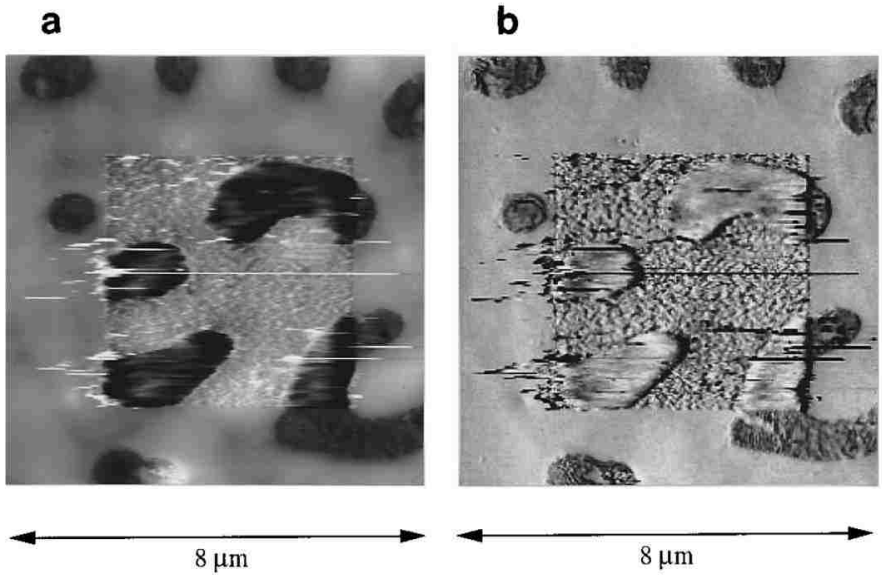

Figure 5.6 Phase separated PS-PEO blend film studied with FMM with imaging force 6 nN and modulation frequency of 5 kHz. The central area of 5 μm^2 was scanned with force of 50 nN. (a) Topography and (b) elasticity images. Reprinted with permission.[62] Copyright 1995 IEEE Xplore.

Molecular chain imaging of poly(vinylidenefluoride-trifluoroethylene) crystal under an amorphous layer was the first report on high resolution imaging of polymer lamella structures using FMM by Kimura and Matsushige et al.[233] A 6 nm x 5 nm scan with lamella stripes spaced at 0.53 nm in the FMM amplitude image was achieved. One year later, the same researchers published work on submolecular resolution viscoelastic imaging of a poly(p-toluene-sulfonate) single crystal using FMM.

5.6 Probing Biological and Inorganic Samples Using FMM

Biological samples such as protein-lipid aggregates,[65] phase separated lipid monolayers,[234] bovine serum albumen,[235] wood cells and fibroblasts,[66-68] magnetotactic bacteria, and live human platelets,[69, 236] were studied with FMM. Inorganic samples such as porous silicon,[70] ion tracks,[237]

nickel-based superalloy,[76] hybrid materials,[238-239] and Gd_2O_3 or SiO_2 optical thin films,[71] were also probed with FMM to acquire the surface elastic and viscoelastic information.

An example of structural organization of surfactant protein B containing lipid monolayers imaged with FMM is shown in Figure 5.7. Surfactant protein B with a molecular weight of 18 kDa and saturated phospholipids dipalmitoylphosphatidylcholine and dipalmitoylphosphatidylglycerol (4:1 with protein content 1 mol%) were transferred on mica. For FMM, a contact-mode probe with a spring constant of 0.12 N/m was used. The probe was oscillated by a biomorph piezo at 9 kHz and indented slightly into the sample. The z scale for the topography image of Figure 5.7 is 25 nm and 2 nm for the amplitude image. The amplitude image gives much sharper contrast as compared to the topograph. The author claimed that the darker contrast in the amplitude channel indicated materials with higher elastic modulus, which is a stiffer material. The lighter contrast area in Figure 5.7b are protein-enriched phase which has lower Young's modulus.

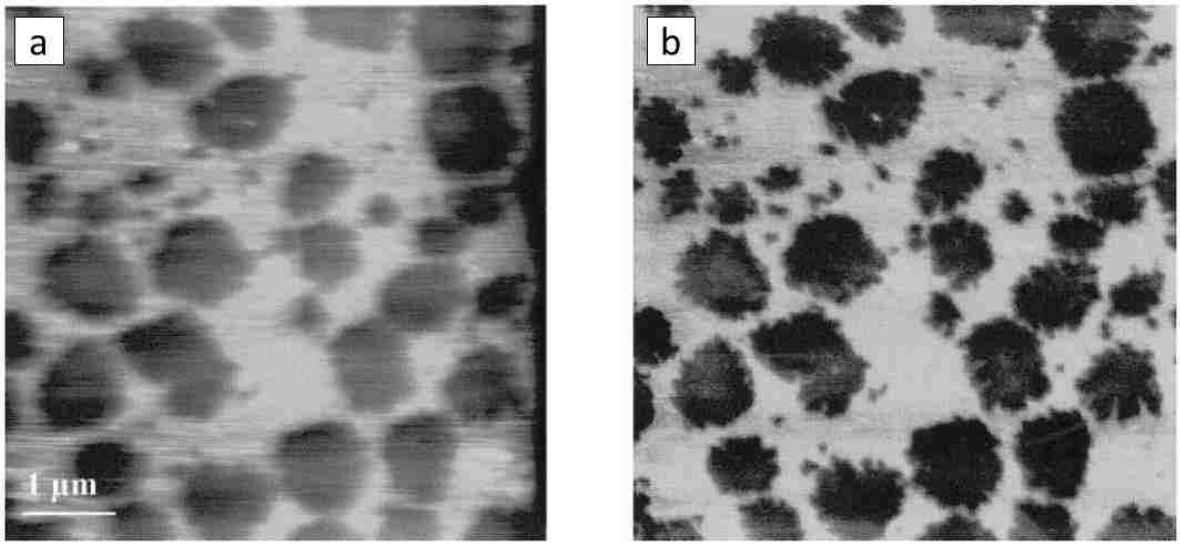

Figure 5.7 Surfactant protein B containing lipid monolayers imaged with FMM. (a) Topography image with the z scale of 25 nm. (b) Amplitude image with the z scale of 2 nm. Reprinted with permission.[65] Copyright 2000 Elsevier.

5.7 Conclusions

Force modulation microscopy is a powerful mode of AFM to acquire surface topography and mechanical information simultaneously. Four FMM set-ups which were commonly used in the literature were discussed in this review. Visualized AFM images containing the elastic and viscoelastic differences about surface features can be shown in FMM amplitude and phase images. Quantitative information such as Young's modulus and elasticity can be calculated based on amplitude channel of FMM. Application of FMM in self-assembled monolayer systems and polymeric materials were summarized and discussed. The FMM mode was also applied in inorganic and biological system to study the mechanical property of samples. Factors such as the vibrational frequency, imaging media, and the shape and stiffness of the tip may influence the contrast in FMM amplitude and phase images. However, it is possible to operate FMM in regions that the image contrast reflects the relative elasticities of different components by tuning the experimental conditions.

CHAPTER 6. SAMPLE STAGE DESIGNED FOR FORCE MODULATION MICROSCOPY USING A TIP-MOUNTED AFM SCANNER

6.1 Introduction

Force modulation microscopy (FMM) can be used to identify and map differences in stiffness or elasticity,[79, 84] evaluate the composition of materials,[85] and to study variations in crystallinity,[6] polymer phase separation, surface arrangement and distribution.[80, 215-217] Materials that have been studied with FMM include protein-lipid aggregates,[65] patterned self-assembled monolayers (SAMs),[60] as well as polymer blends and resins.[61-64] Molecularly resolved images of polymer crystals have been acquired with FMM.[233, 240] Quantitative measurements can be evaluated using FMM for the Young's modulus and the elasticity of samples. [75-76, 79, 213]

For FMM mode the scanner is operated in contact-mode while the sample stage is driven to vibrate. The AFM probe is scanned in continuous contact with the surface as the sample is driven to vibrate at selected frequency and amplitude. Information of the topography, elastic response and surface adhesion can be acquired concurrently. There are two instrument configurations that have been used to accomplish FMM imaging, either the sample or tip can be driven to vibrate with pressure applied at the area of tip-sample contact. Most commonly FMM has been done using an instrument configuration with the sample placed directly on top of an xyz scanner. Actuation of the z piezoelement causes the sample to vibrate for tip displacements of a few nm in the z-direction.[62, 77-80] Studies have been done using a cantilever holder equipped with bimorph piezoelements to accomplish force modulation, which can actuate the tip as it is pressed against the sample.[63, 84] A magnetic field has been used to drive the vibration of a tip or tip-holder assembly to accomplish force modulation imaging. [16, 85, 87] The driving frequency,[225] imaging media,[89, 226] tip-sample contact area,[221] amplitude of oscillation,[227] and the shape and stiffness of the tip[72, 217] influence the resolution of FMM amplitude and phase images. A systematic study of

the factors which influence the contrast in FMM was previously reported by Jourdan, et al. for nanopatterns inscribed within a film of organosilane.[89]

With the wide implementation of commercial scanning probe instruments designed to have the tip mounted on the piezotube scanner, it would be practical to develop a sample stage to facilitate sample modulation for FMM experiments. An accessory stage for FMM studies was constructed with machined polycarbonate using an insulated coaxial cable connection to apply current to an actuator element. The operation of the sample stage was evaluated by characterizing three test samples with nanoscale dimensions. Test structures of nanoholes within a film of octadecyltrichlorosiloxane (OTS) provide two distinct surface regions as the simplest platform for FMM studies. Ring-shaped nanostructures prepared on Si(111) with 2-[methoxy (polyethyleneoxy)propyl]trichlorosilane (PEG-silane) provide three domains for evaluating FMM data. Finally, a complex sample consisting of a cyclic gel polymer of poly(*N*-methyl glycine)$_{100}$-*b*-poly(*N*-decyl glycine)$_{10}$ containing fibrils was selected for FMM studies. Experiments were accomplished in ambient conditions using conventional soft cantilevers.

6.2 Experimental Section

6.2.1 Materials and Reagents

Anhydrous toluene from Sigma-Aldrich (St. Louis, MO) was used as a solvent. Ethanol used for cleaning samples was acquired from Pharmco-AAPER (Boucherville, Quebec). Octadecyltrichlorosilane (OTS) and 2-[methoxy(polyethyleneoxy)propyl]trichlorosilane (PEG-silane) were purchased from Gelest (Morrisville, PA) and used without further purification. Pieces (5 × 7 mm) of polished Si(111) doped with boron (Ted Pella, Inc., Redding, CA) were used as substrates for preparing nanopatterned films. Substrates were cleaned by immersion in piranha solution for 1.5 h. Piranha solution is a mixture of sulfuric acid (Sigma-Aldrich) and hydrogen peroxide (30%, Sigma-Aldrich) at a ratio of 3:1 (v/v). This solution is highly corrosive and should

be handled with caution. Silicon substrates were then rinsed copiously with water (Milli-Q, Millipore, Bedford, MA) and dried with argon. Monodisperse polystyrene (496 ± 8.1 nm) and silica (0.49 ± 0.02 μm) solutions were purchased from Duke Scientific (Palo Alto, CA). The mesospheres were washed with deionized water by centrifugation to remove contaminants such as charge stabilizers or surfactants. To prepare the cyclic gel sample for FMM, the polymer sample was dissolved in methanol at 1% wt and formed a flow gel after 30 min. A drop of the flow gel (10 μL) was deposited on a piece of freshly cleaved mica(0001), then dried in air before imaging with FMM-AFM.

6.2.2 Atomic Force Microscopy

A Keysight model 5500 scanning probe microscope (SPM) equipped with a multipurpose scanner was used for AFM characterizations (Keysight Technologies, Tempe, AZ). The scanner has interchangeable nosecones for selected imaging modes. An empty plastic nosecone assembly (the contact-mode nosecone) without metal components was used for force modulation experiments. Silicon nitride cantilevers with an average force constant of 0.1 N m^{-1} were used for FMM-AFM imaging (MSCT, Bruker, Camarillo, CA). Picoview v1.12 software was used for data acquisition. Images were processed with Gwyddion (version 2.31) open software supported with Czech Metrology Institute, which is freely available online.[241]

6.3 Results and Discussion

6.3.1 Design of the FMM Sample Stage

The sample stage was made with machined polycarbonate with a shape that was designed for operation with a Keysight 5500 SPM. A photograph of the stage is shown in Figure 6.1, indicating the location of the piezoactuator and the BNC cable connection. The essential component of the FMM stage is the piezoactuator element (dimensions: 1 × 1 × 0.2 cm), which enables a z-displacement of 2.2 μm in the range of 0-100 V input and has an axial resonance

frequency of 600 kHz (Physik Instrumente, Auburn, MA). For FMM studies, the voltages applied to the piezoactuator ranged from 0.05-0.5 V. The black and red wires connect the piezoactuator to the BNC cable which enables input of an AC signal to the stage to induce the vibration of the piezoelement. With the Keysight 5500 instrument, a MAC box was used as an AC source by connecting with the AAC output channel. There are three round flat magnets to attach the sample stage to the scanner housing. Two alignment tracks were machined into the polycarbonate sample holder for translating the sample stage in the x and y direction. A small magnet was embedded within the center of the stage above the piezoactuator to attach samples. Samples for FMM studies can either be magnetically clamped, taped or glued to the center of the stage. Further technical details of the physical dimensions of the stage are provided in Appendix Figure D1.

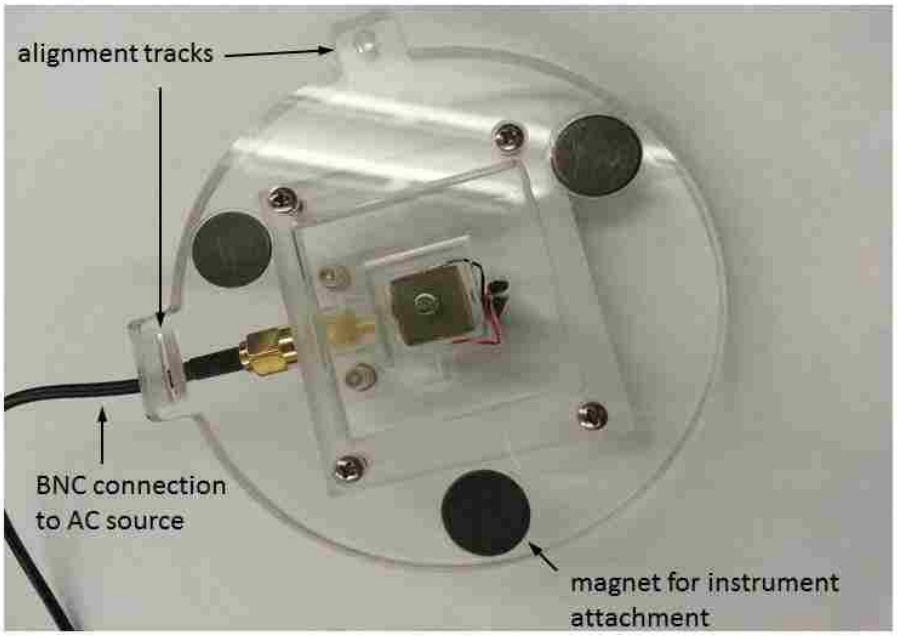

Figure 6.1 Photograph of the polycarbonate FMM sample stage. The square piece at the center of the stage is the piezoactuator, with a small circular magnet placed at the center for attaching samples.

6.3.2 Characterization of Nanopatterns within an OTS Film using the FMM Sample Stage.

A test sample of OTS nanopatterns formed on Si(111) was used to evaluate the operation and sensitivity of the FMM sample stage. Details of the procedure for preparing samples using particle lithography with OTS were previously reported and are presented in Appendix Figure D2.[228] Experiments were designed to test the effect of turning the drive on or off as well as evaluating changes in images for selected frequencies. Simultaneously acquired channels for topography, amplitude, and phase are shown in Figure 6.2 for the sample of OTS nanopores. The

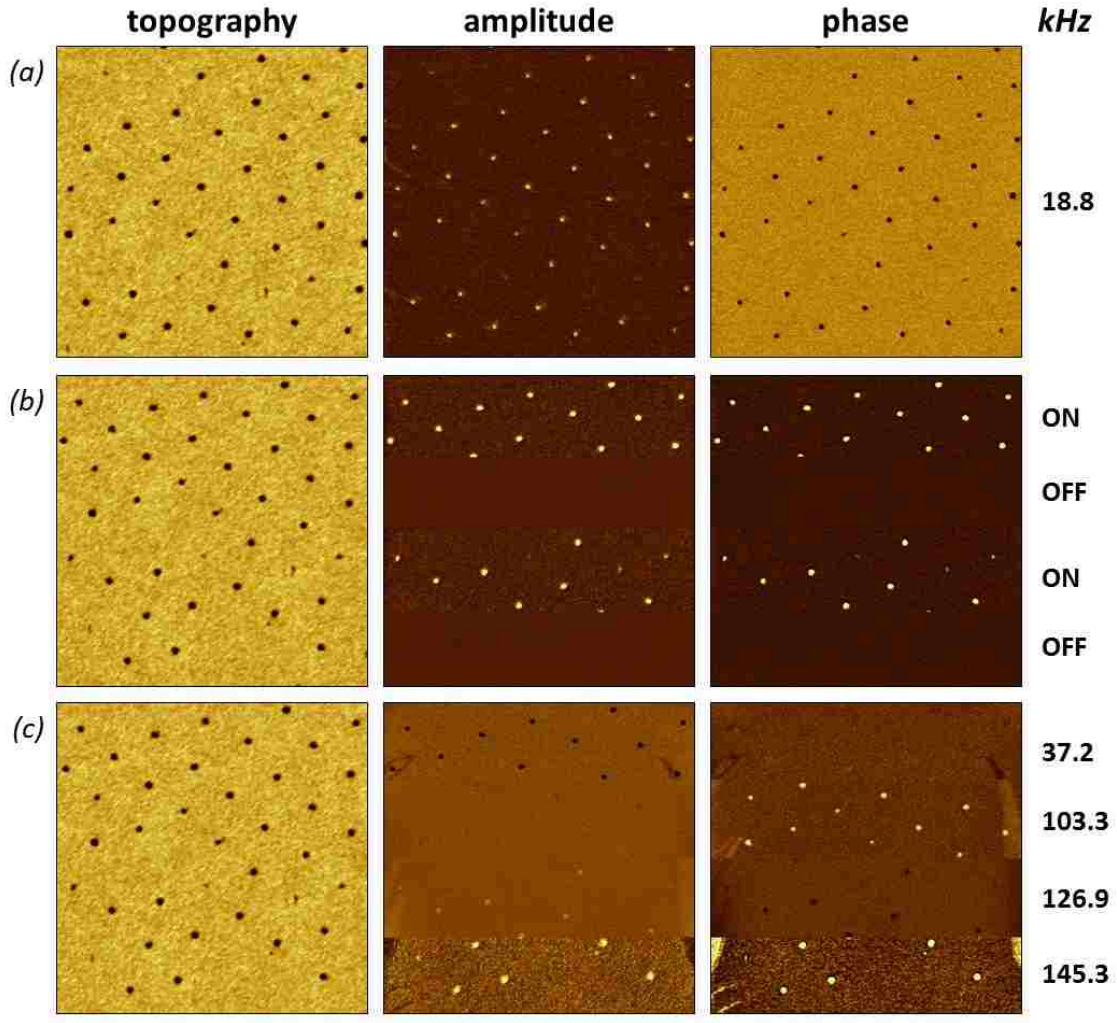

Figure 6.2 Sample of nanopores within a thin film of OTS characterized with the FMM sample stage. (a) Images acquired at frequency of 18.8 kHz. (b) Image acquired with the drive turned on or off at a frequency of 145.3 kHz. (c) Dynamic FMM study with ramping of the frequency parameters during a single scan. The size of the images are 3×3 μm^2.

same area was scanned using selected parameters for sample modulation. A hexagonal arrangement of nanopores is visible in the topography frames, where the dark spots are areas of uncovered substrate and the brighter areas are the matrix film of OTS. The distance between adjacent nanopores measures 490 ± 44 nm. The depth and diameter of the nanopores measured 2.0 ± 0.2 nm and 110 ± 10 nm respectively. Changes in the bright or dark contrast of the areas of the nanopores are reversed for the amplitude versus phase channels in Figure 6.2a, when imaging at frequency of 18.8 kHz. The bright or dark regions are highly sensitive to the driving frequency of the sample stage. The phase images do not necessarily correlate with hardness of the samples. When the drive is turned off, no features are distinguishable in amplitude and phase images as demonstrated in Figure 6.2b. Note that by changing the frequency to 145.3 kHz the harder regions of the substrate have bright contrast in both the amplitude and phase channels. In a dynamic FMM study, the results of selectively ramping the frequency are displayed in Figure 6.2c without interruption of data acquisition during a scan. The changes in color contrast for amplitude frames can be interpreted by conducting a frequency sweep experiment, an example spectrum is shown in Figure 6.3. The areas of the nanopores reveal exposed silicon substrate which is harder compared with the surrounding film of OTS, thus greater amplitude or bright contrast is expected for nanopore areas. However, the results shown in Figure 6.2c exhibit a reversal in contrast depending sensitively on the frequency that was selected.

Clear differences in color contrast between areas of the nanopores and the matrix OTS film are evident in the amplitude and phase images, however using these results to interpret the hardness or softness of the areas can be complicated. For this example, the larger resonance peaks at 18.8 and 145.3 kHz gave the predicted amplitude response showing bright dots for the locations

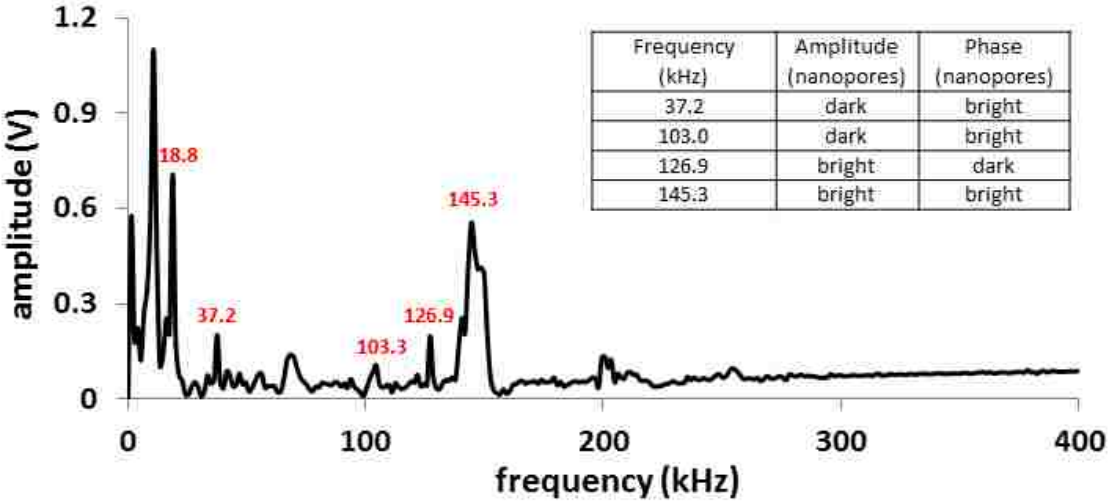

Frequency (kHz)	Amplitude (nanopores)	Phase (nanopores)
37.2	dark	bright
103.0	dark	bright
126.9	bright	dark
145.3	bright	bright

Figure 6.3 Frequency sweep experiment with the sample of OTS nanopores.

of the nanopores. The frequency or amplitude chosen for driving the tip vibration, determine whether the tip is operated in the attractive or repulsive regime for FMM imaging.

A further test of the FMM stage was accomplished by zooming-in to acquire surface views with higher magnification (Figure 6.4). At this size scale the irregular outline of a single nanopore becomes apparent. The texture of the OTS film can be resolved, showing a clustered morphology. This example demonstrates the high resolution capabilities that can be achieved with the home-constructed FMM sample stage.

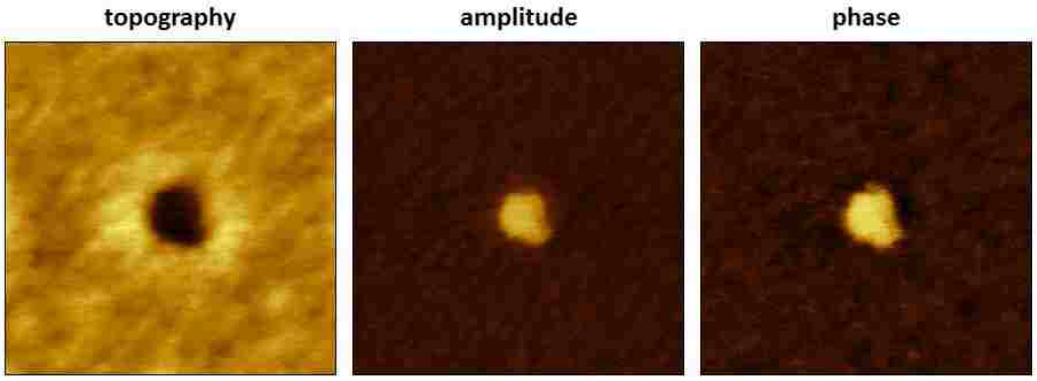

Figure 6.4 Details of a single nanopore revealed with FMM. Images were acquired at 145.3 kHz for an area measuring $0.4 \times 0.4\ \mu m^2$.

6.3.3 FMM Characterization of Nanorings of PEG-silane

Nanopatterns of PEG-silane rings prepared on Si(111) were characterized with FMM-AFM as shown in Figure 6.5. For this example, there are three distinct regions visible in the images. There are uncovered areas of the substrate at the centers of the nanorings, the regions of the nanorings are multilayers of PEG-silane, and the areas in between the rings are a relatively homogeneous and compact film of PEG-silane. The sample was prepared using particle lithography combined with heated vapor deposition, as previously described.[242] (Details for sample preparation are also provided in Appendix Figure D3.) The areas of the taller nanorings have

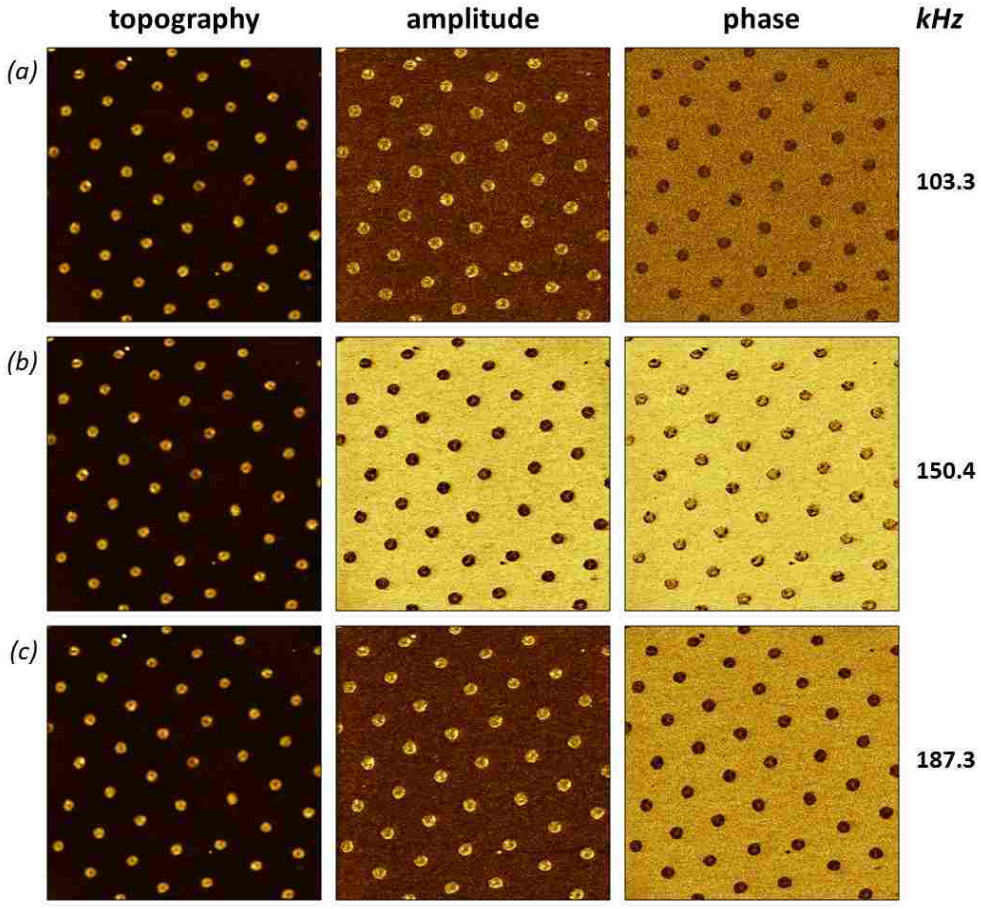

Figure 6.5 Images of PEG-silane nanorings acquired with the FMM sample stage at driving frequencies of (a) 103.3 kHz, (b) 150.4 kHz and (c) 187.3 kHz. Images are 3 × 3 μm^2 scan sizes.

brighter contrast in the topography images indicating the areas of a multilayer of PEG-silane. The thickness of the nanorings measures 5.9 ± 1.3 nm (Appendix Figure D4). The areas between the nanorings contain a film of PEG-silane. Areas of exposed substrate are located at the very center of the nanorings. The distance between nanorings measured 490 ± 45 nm, which corresponds to the diameter of the latex mesospheres (500 nm) that were used as a surface mask for particle lithography. The same area was scanned with selected frequencies to evaluate the changes for images shown in amplitude and phase channels (Figure 6.5).

Three frequencies (103.3, 150.4, and 187.3 kHz) were selected for Figure 6.5 to study the changes for PEG-silane nanorings with FMM-AFM. We would predict that areas of the nanorings with a multilayer film of PEG-silane would have the darkest color for the amplitude frames, as shown in the center amplitude image acquired at a driving frequency of 150.4 kHz. The nanoring structure is made of multilayers of PEG-silane which is a softer material compared with the surrounding matrix areas and the center of the rings, which leads to a smaller amplitude for tip indentation. The center amplitude image acquired at 150.4 kHz also sensitively reveals a tiny bright spot at the center of each nanoring for the region of exposed hard substrate. The images in Figures 6.5a and c disclose brighter contrast for the PEG-silane nanorings, which does not follow our prediction. Examples of contrast reversal have been previously reported for nanopatterns within an organosilane film.[89] The contrast observed for amplitude and phase images depends sensitively on the modulation parameters of frequency and amplitude and indicate the viscoelasticity of the sample.

The frequency spectrum acquired for the sample is presented in Figure 6.6, which shows the highest amplitude response of the selected frequencies occurs at 150.4 kHz. As with the example of Figure 6.2, the optimal frequency for FMM imaging are at the resonance peaks with a

higher amplitude response. Brighter contrast for the nanorings was observed for the amplitude channel in Figures 6.5a and c, suggesting that the selected frequencies of 103.3 and 187.3 kHz were not optimal parameters for resolving differences in elasticity. In these examples, the edge effects and surface adhesion predominate tip-sample interactions rather than differences in hardness. In the phase channels for all three frequencies viewed in Figure 6.6, dark rings and lighter background can be clearly resolved to indicate the relative differences in viscoelasticity between the nanorings and surrounding matrix film of PEG-silane.

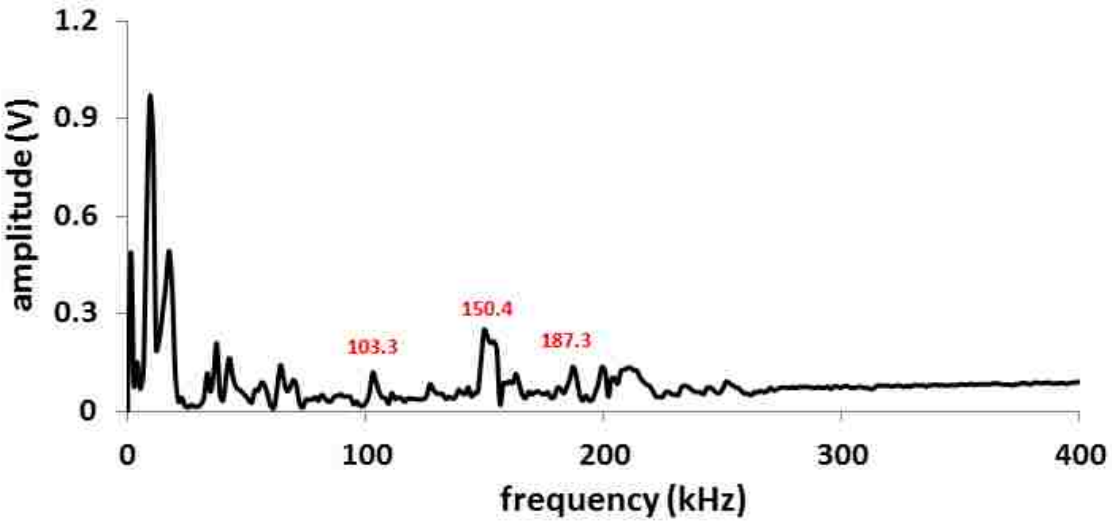

Figure 6.6 Frequency sweep acquired with FMM for the sample of PEG-silane nanorings.

6.3.4 Characterization of a Cyclic Gel Sample with FMM

A block copolymer poly(*N*-methyl glycine)$_{100}$-*b*-poly(*N*-decyl glycine)$_{10}$, or *c*-PNMG$_{100}$-*b*-PNDG$_{10}$ can form free-standing gels at 5-10 wt% in methanol at room temperature.[232] The gel system contains entangled fibrillar structures that are difficult to resolve with conventional topography images. Synthesis and characterization of the cyclic gel sample was previously reported using tapping-mode AFM.[232] The gel sample is more complex than the previous examples of nanopatterns, it contains both large aggregates and small-embedded fibrils within the gel system.

Topography, amplitude and phase channels obtained with FMM at four selected frequencies are shown in Figure 6.7. The same area of the sample was scanned (8×8 μm^2) with changes of the frequency parameter. For the topography frames the details of the small microfibrils within the sample cannot be clearly resolved, however the phase and amplitude images sensitively detect the fine details of the fibril shapes and locations.

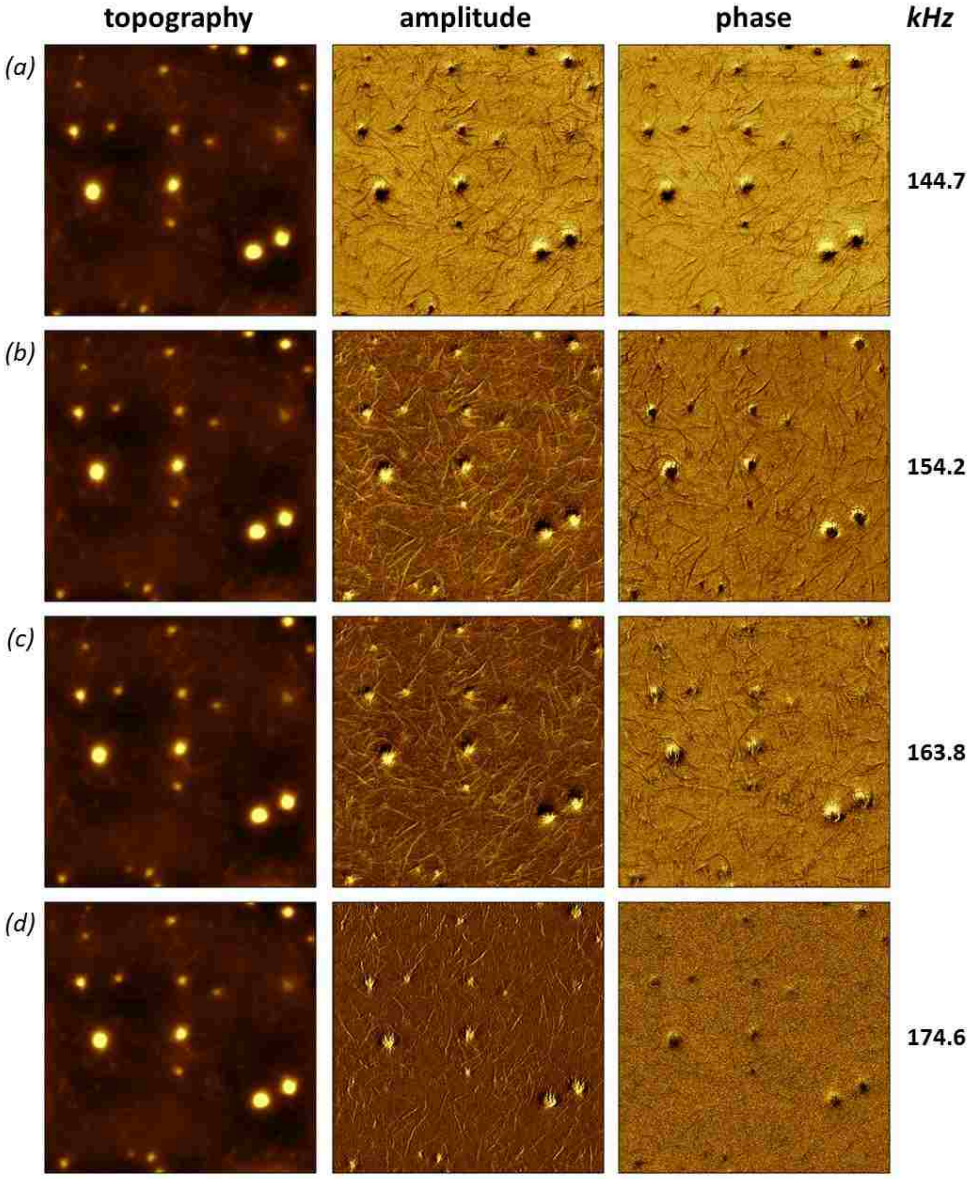

Figure 6.7 Images of the cyclic gel sample obtained with FMM at driving frequencies of (a) 144.7, (b) 154.2, (c) 163.8, and (d) 174.6 kHz. The frames are 8×8 μm^2 scans.

The fibrils are harder materials compared with the surrounding gels, therefore larger amplitude or bright contrast is expected for the fibrils as revealed in the amplitude frames of Figures 6.7b-d. Contrast reversal is shown in Figure 6.7a, where the fibrils are darker in color for the amplitude frame. The phase images of Figures 6.7a-c have excellent resolution, revealing exquisite details of the fibril morphology. However at a frequency of 174.6 (Figure 6.7d) the locations of the fibrils are not distinguishable in the phase image. These results suggest that for tuning the optimized parameters for FMM experiments selected for the amplitude channel are not necessarily the same frequency chosen for optimizing the phase images. The frequency sweep when imaging the cyclic gel sample is shown in Figure 6.8. The poorest resolution found at frequency of 174.6 kHz correlates with the smallest amplitude response. At this frequency the

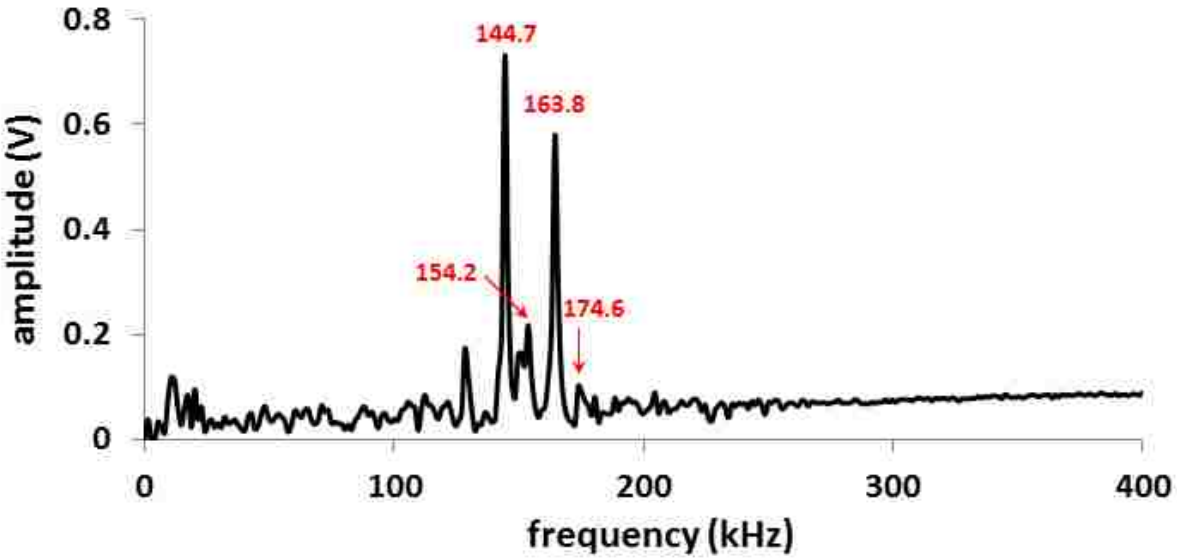

Figure 6.8 Frequency spectrum acquired with the FMM sample stage for the cyclic gel sample (*c*-PNMG$_{100}$-*b*-PNDG$_{10}$).

vibration amplitude is not sufficient to fully reveal differences in elastic response. However, for the other three frequencies tested with FMM, sufficient energy is supplied to acquire high resolution images for both phase and amplitude channels.

Both the driving frequency and the amplitude of the resonance peak determine the resolution of the FMM amplitude and phase channels. Weaker resonance peaks were shown to display a contrast reversal for elastic response. For the sample of OTS nanopores and the nanorings of PEG-silane, strong resonance peaks were found at frequencies below 25 kHz. The voltages applied to the piezoactuator of the stage were 0.4 V for the OTS nanopores and 0.5 V for PEG-silane nanorings. For the nanopatterned surfaces of OTS and PEG-silane the overall z scale measured less than 10 nm, while the cyclic gel sample had taller features of 160 nm (Appendix Figure D5). For the complicated system of the cyclic gel sample, which has larger aggregates along with micron-sized fibrils embedded in the gel system, stronger resonance peaks were detected in the frequency range of 120-180 kHz using 0.05 V applied to the piezoactuator.

6.4 Conclusions

Excellent resolution can be achieved when using the home-constructed FMM sample stage with a tip-mounted scanner, even for complex surfaces or multi-component samples. The FMM stage is suitable for imaging samples in ambient conditions and exhibited high resolution when experimental parameters were optimized. Interpretation of FMM amplitude frames is complicated for acquiring quantitative measurements of elastic response, the parameters for driving frequency and amplitude require optimization. Knowledge of the sample composition is critical for correctly interpreting information from amplitude images. Future studies will incorporate a liquid cell for the design of the FMM stage to enable FMM characterizations in liquids. Machined glass components will be used for constructing a sample stage to enable studies in solvents.

CHAPTER 7: DIRECT COMPARISON OF SAMPLE ACTUATION VERSUS TIP VIBRATION CONFIGURATION FOR FORCE MODULATION AFM

7.1 Introduction

Force modulation microscopy (FMM) was invented in 1991 and has since been used by researchers in many fields.[14, 77, 79-80, 82, 215, 220, 235] This mode of atomic force microscopy (AFM) is used to measure the dynamic response of the sample while applying pressure to the surface during contact-mode imaging, providing elasticity and viscoelasticity measurements of the sample.[81] The most common instrument set up is to mount the sample on a piezoelectric xyz scanner and apply a sinusoidal voltage to the vertical piezoceramic material, which will cause the sample to vibrate in the z direction.[62, 77-81] Another common setup for FMM is to use a cantilever holder equipped with bimorph piezo.[63, 83-84] The bimorph piezo oscillates the cantilever near its resonance frequency during tapping and slightly presses the tip into the sample during force modulation. Therefore, tapping-mode and force modulation images can be acquired using this design. Mechanical vibration is not the only way to modulate the tip or sample for FMM. In some cases, a solenoid is placed around the scanner tube, where the sample is attached, to generate an oscillating magnetic field. A magnetically coated cantilever or a small spherical magnetic particle glued to the back of the cantilever can be indirectly modulated by the oscillation of the magnetic field.[85, 87-88, 213]

Force modulation microscopy is able to acquire topographical information along with the mechanical properties (elasticity and viscoelasticity) of samples at the same time.[6] It has great applications in a variety of fields, especially soft materials such as polymers and biological systems.[63, 236] Polymeric systems such as toughened polypropylene resins,[61] polystyrene-polyethyleneoxide and polyvinyl chloride-polycarbonate blends[62, 64] have been probed with FMM for viscoelastic information.[209, 230] Biological systems such as magnetotactic bacteria,[69] human platelets,[69] living fibroblasts[67-68] have been investigated for elastic properties using FMM.[65-66]

Other systems such as hybrid materials,[238-239] patterned or phase separated self-assembled monolayers,[60, 216] Gd_2O_3 or SiO_2 optical thin films,[71] have also been studied with FMM.[70, 237]

Our group has developed two methods for investigating the mechanical properties of samples. We have recently designed a sample stage capable of sample modulated FMM. Several samples have been evaluated to test the abilities of this stage. This polycarbonate sample stage can be easily reshaped to fit other models of AFM. Indirect magnetic modulation (IMM), which invented in our group earlier, is an alternative way to do force modulation microscopy by indirectly modulating the nosecone assembly.[16] The soft, nonmagnetic cantilever is driven to vibrate with the motion of the nosecone containing ferromagnetic materials. The nosecone is induced to vibrate with the flux of an external electromagnetic field, which is generated by the solenoid beneath the MAC-mode sample stage. The goal of this study is to use nanoring patterns of 4-(chloromethyl)phenyltrichlorosilane (CMPS) as a test platform to compare FMM using the newly-designed sample stage and IMM using the MAC-mode stage. The organosilane, CMPS, is highly reactive to itself and easily forms multilayers on surfaces. The multilayers provide soft surfaces suitable for force modulation studies. In addition, four regions (CMPS monolayer, multilayers and hard surfaces) are formed by patterning CMPS with particle lithography, which makes this sample a good candidate for elasticity studies on surfaces. Additionally, the influence of driving frequency and vibration amplitude on FMM and IMM imaging are systematically studied in this Chapter for the very first time.

7.2 Experiment Section

7.2.1 Materials and Reagents

Single-side polished Si(111) doped with boron (Ted Pella, Inc., Redding, CA) was used as substrates. Monodisperse latex mesoparticles (496 ± 8.1 nm) were purchased from Duke Scientific (Palo Alto, CA). Nanopatterns were fabricated using 4-(chloromethyl)phenyltrichlorosilane

(Gelest, Morrisville, PA) without further purification. Toluene, sulfuric acid, and hydrogen peroxide (30%) were obtained from Sigma-Aldrich (St. Louis, MO). Ethanol was used to clean the substrate, which was purchased from Pharmco-AAPER (Boucherville, Quebec).

7.2.2 Atomic Force Microscopy

A Keysight 5500 SPM (Keysight Technologies, Tempe, AZ) was used for FMM and IMM studies. The scanner can incorporate interchangeable nosecones for selected imaging modes. A contact-mode nosecone assembly without metal components was used for the FMM study. An AAC nosecone, which has two metal pins, was used for the IMM study. Picoview v1.12 software was used for data acquisition. Images were processed with Gwyddion (version 2.31) open software supported with Czech Metrology Institute, which is freely available online.[241] A nonmagnetic silicon nitride probe with force constant of 0.1 N m^{-1} was used for FMM and IMM imaging (MSCT, Bruker, Camarillo, CA).

7.2.3 Preparation of CMPS Nanorings

The Si(111) substrates were immersed in piranha solution for 2 h to remove organic contaminants. Piranha solution is a mixture of sulfuric acid and hydrogen peroxide at a ratio of 3:1 (v/v). This solution is highly corrosive and should be handled carefully. Substrates were then rinsed with copious of water (Milli-Q, Millipore, Bedford, MA) and dried with argon. The mesospheres were washed three times with deionized water to remove charge stabilizers and surfactants. Immediately after drying the substrate, 10 μL of the latex mesosphere suspension was deposited. The sample was dried in air for 4 h to produce surface masks. Next, the sample was placed in a sealed cup containing 300 μL of neat CMPS silane. The cup was placed in an oven at 70 C for 18 h. The CMPS silane was vaporized to react with Si substrate where the mesospheres do not contact the substrate. After cooling, the sample was rinsed with water and toluene. To

remove the mesoparticles, the substrate was sonicated for 15 min in ethanol and toluene successively. The sample was dried under argon before characterization with FMM and IMM.

7.2.4 Characterization of CMPS Nanorings with Stage-driven FMM.

The polycarbonate sample stage is designed for a Keysight 5500 AFM and can be manufactured for other SPM models. A 1 cm × 1 cm × 0.2 cm piezoactuator (Physik Instrumente, Auburn, MA) is embedded inside the sample stage and has a maximum displacement of 2.2 μm in the input range of 0-100 V. The outside AC source, which is the MAC box, can input an AC signal to the stage via a BNC cable connection; this signal induces the z-axis vibration of the piezoelement. As shown in Figure 7.1a of the FMM logo, only the center part of the stage (1.4 cm × 1.4 cm square area) vibrates during FMM. The driving frequency and vibration amplitude can be tuned based on the frequency spectra.

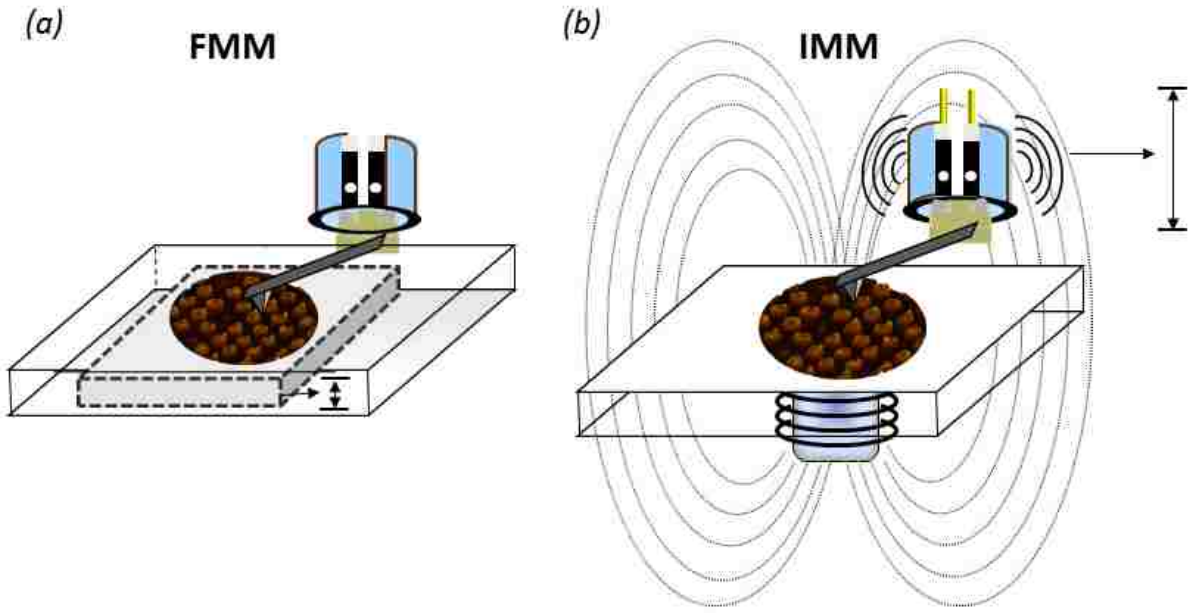

Figure 7.1 Comparison of the instrumental configuration of (a) stage-driven force modulation microscopy (FMM) and (b) tip-driven indirect magnetic modulation (IMM).

7.2.5 Characterization of CMPS Nanorings with Tip-driven IMM

The invention of IMM mode was introduced by our group previously.[16] The entire tip holder assembly is indirectly modulated through the flux of an external ac electromagnetic field generated with a wire coil solenoid located underneath the sample stage Figure 7.1b (IMM logo). The metal pins inside the nosecone are vibrating in the magnetic field to indirectly vibrate the AFM tip.

Both stage-driven FMM and tip driven IMM are operated in contact-mode. Height (topography channel), elasticity (amplitude channel), and viscosity/viscoelasticity (phase channel) information can be acquired at the same time. Tips with a low spring constant (< 1 N m^{-1}) are suggested for use with both methods.

7.3 Results

7.3.1 Nanorings of CMPS Studied with FMM and IMM with and without Sample/Tip Modulation

The shape and hexagonal pattern of CMPS nanorings on a silicon surface prepared by particle lithography combined with chemical vapor deposition can be viewed in Figure 7.2. The periodicity of the CMPS nanopatterns is ~500 nm, which is determined by the diameter of the latex mesospheres used to fabricate the patterned sample. The shapes of the nanorings are not identical due to a variation in the volume of water at the meniscus of the mesospheres which affects the polymerization reaction of CMP. Brighter contrast in the topograph corresponds to the polymerized CMPS nanorings, while the darker background consists of a CMPS monolayer or nanopillars in between the nanorings. Individual dark points can be viewed in the amplitude image in the areas between nanorings, which is CMPS nanopillars (several layers of CMPS). The centers of the nanorings are the bare silicon substrates, which are the lowest point on the surface.

When manually turning on and off the vibration of the sample stage during FMM imaging, clear contrast changes can be seen from the FMM amplitude and phase channels (Figure 7.2a). Topographs will not be influenced by the vibration of the stage since the AFM is operated in contact-mode and the tip keeps in constant contact with sample surface.[83] There is no signal present in the amplitude channel when the sample stage vibration is turned off. Some contrast can be seen in the phase channel when the vibration is turned off which is attributed to edge effects. Therefore, without the vibration of the sample stage, AFM system is operated in contact-mode; while with the vibration of the stage, the system is operated in force modulation so that there will be contrast in the amplitude and phase channel. The vibration frequency of the stage is on the order of hundreds of kilohertz, which is much faster than the feedback loop. Thus, topographical information can be isolated from the local differences in the sample's elasticity.

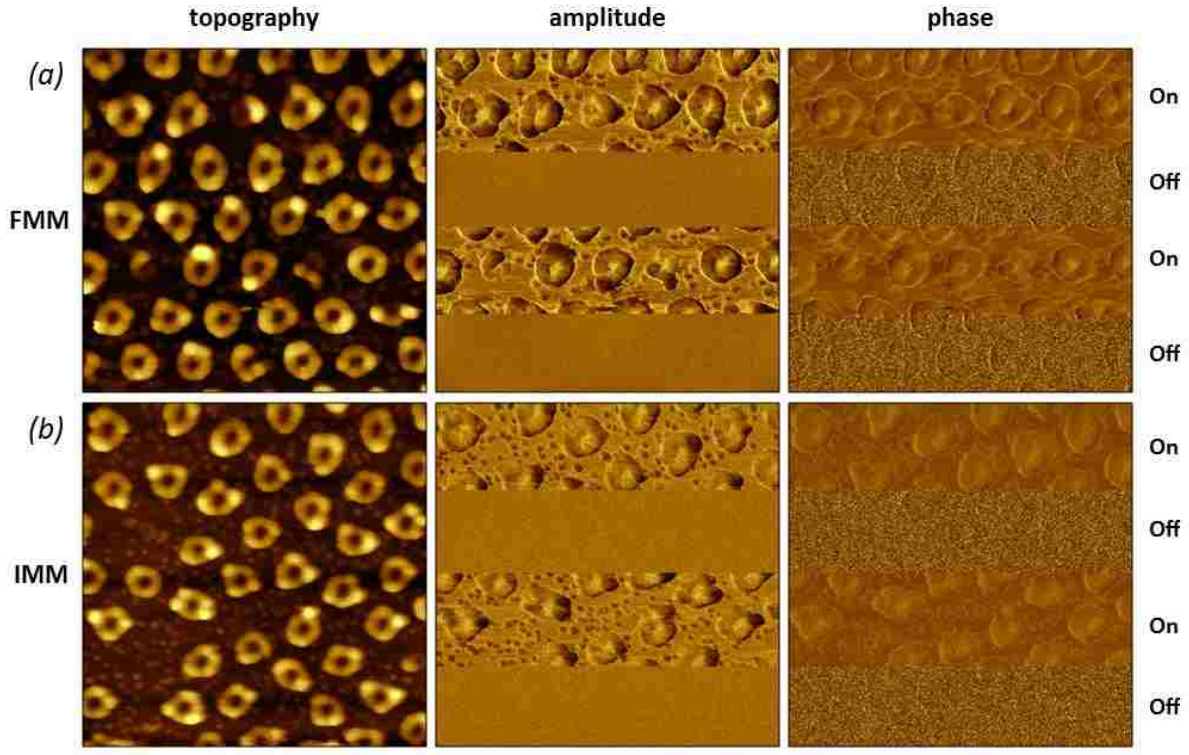

Figure 7.2 Force modulation imaging of (a) sample shaking vs. (b) tip shaking with the field turning on and off. The selected "on" frequencies for FMM and IMM are 16.3 kHz and 37.6 kHz, respectively. Image sizes are $3 \times 3\ \mu m^2$.

Polymerization of the organosilane on the sample surface occurs due to water forming a meniscus at the base of the mesospheres. This meniscus and the volume of water it contains is necessary to initiate the polymerization reaction and leads to the nanoring formations of CMPS that were observed. In the spaces between the nanorings, individual nanopillars formed because the existence of clustered water molecules on surface. The rest of the area between nanorings is a single monolayer of CMPS. The result is a sample that contains several differing elastic regions to be compared by stage-driven FMM and tip-driven IMM. The harder the surface is, the larger the amplitude AFM tip response will be. Therefore, the lighter contrast of the center of the nanorings should be seen in the amplitude channel, as shown in the amplitude image which was acquired at a frequency of 16.3 kHz. Even though the color contrast in the phase image is not distinct, the difference of the viscoelasticity between the nanorings, the center of the nanorings and the surrounding is still obvious.

To compare with stage-driven FMM, the nanoring patterns on Si(111) surface were characterized by tip-driven IMM with the magnetic field on and off (Figure 7.2b). The nanorings and nanopillars can be seen in the topography image. Switching the magnetic field between on and off does not influence the topography image, while no contrast can be obtained when the magnetic field is off in the amplitude and phase image. The distinct edges can be seen when turning off the field in the amplitude and phase images. The selected driving frequency of 37.6 kHz was used when acquiring Figure 7.2b. The dark contrast of the nanorings and nanopillars along with the light contrast of the center of the nanorings is apparent in the amplitude image. This corresponds well with the elasticity difference of the materials on surface, since softer materials should have lower amplitude. The color contrast of the phase image when field is on is not distinct, but nanoring structures are still visible.

Nanorings of CMPS studied with stage-driven FMM and tip-driven IMM with and without sample/tip modulation have similar results. High resolution AFM images with elasticity information can be acquired for both methods when same amount of voltage was applied to the system (0.8 V).

7.3.2 Nanorings of CMPS Studied with FMM at Selected Driving Frequencies

The frequency-dependence of the tip response to the CMPS nanorings is shown in Figure 7.3. The same area was scanned five times at selected driving frequencies (Figures 7.3a-e). The color scales for the topography frames of Figures 7.3a-e for the height differences remain the same regardless the frequency used. Light contrast of the nanorings and dark contrast of the centers of nanorings in the amplitude frame can be seen at driving frequencies of 35.2, 95.6, and 152.4 kHz (Figures 7.3c-e). Dark nanorings and light center can be viewed in the amplitude channel at a frequency of 16.3 kHz (Figure 7.3b). The contrast at a frequency of 11.5 kHz is not distinct, but the shape still can be seen with clear edges of the nanorings (Figure 7.3a). The viscoelasticity difference of the sample surface can be viewed clearly in the phase frames of Figures 7.3a-c and e, but not d. A clear contrast difference between center of the nanoring (bare substrate) and the surrounding area (CMPS monolayer) can be seen from amplitude channels b, c, and d, and phase channels a, b, c, and e.

In the amplitude channel, the harder material should have a lighter contrast. This means that a frequency of 16.3 kHz is the most representative frequency to show the mechanical differences of the CMPS nanoring sample.

7.3.3 Nanorings of CMPS Studied with IMM at Selected Driving Frequencies

Five driving frequencies of 37.6, 54.6, 76.8, 144.1 and 163.1 kHz were selected based upon the frequency sweep, which will be shown later, to investigate the frequency-dependence of this sample using tip-driven IMM. The same area was scanned five times at selected frequencies as

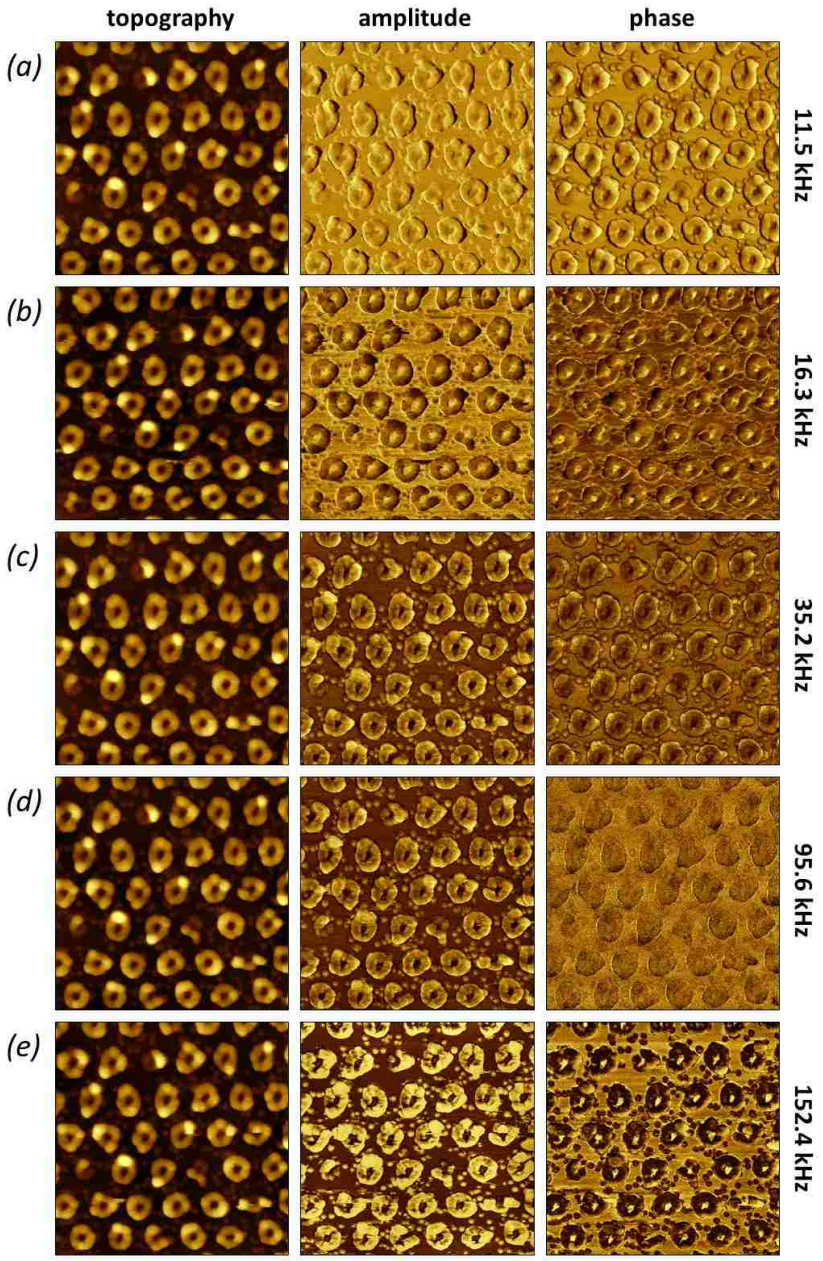

Figure 7.3 Nanorings of CMPS imaged with FMM at selected driving frequencies. Image sizes are 3×3 μm^2.

shown in Figure 7.4. The color contrast of the topography frames (Figures 7.4a-e) stays the same regardless of the driving frequency used. In the amplitude frames, dark contrast of the nanorings and light contrast at the center of the nanorings can be viewed at frequencies of 37.6 and 76.8 kHz, with the opposite effect at frequencies of 54.6 and 163.1 kHz. Therefore, frequencies of 37.6 and

76.8 kHz were chosen to study the mechanical properties of this sample using IMM with this probe. The interesting edge effect can be seen at frequency of 144.1 kHz in the amplitude channel. In the

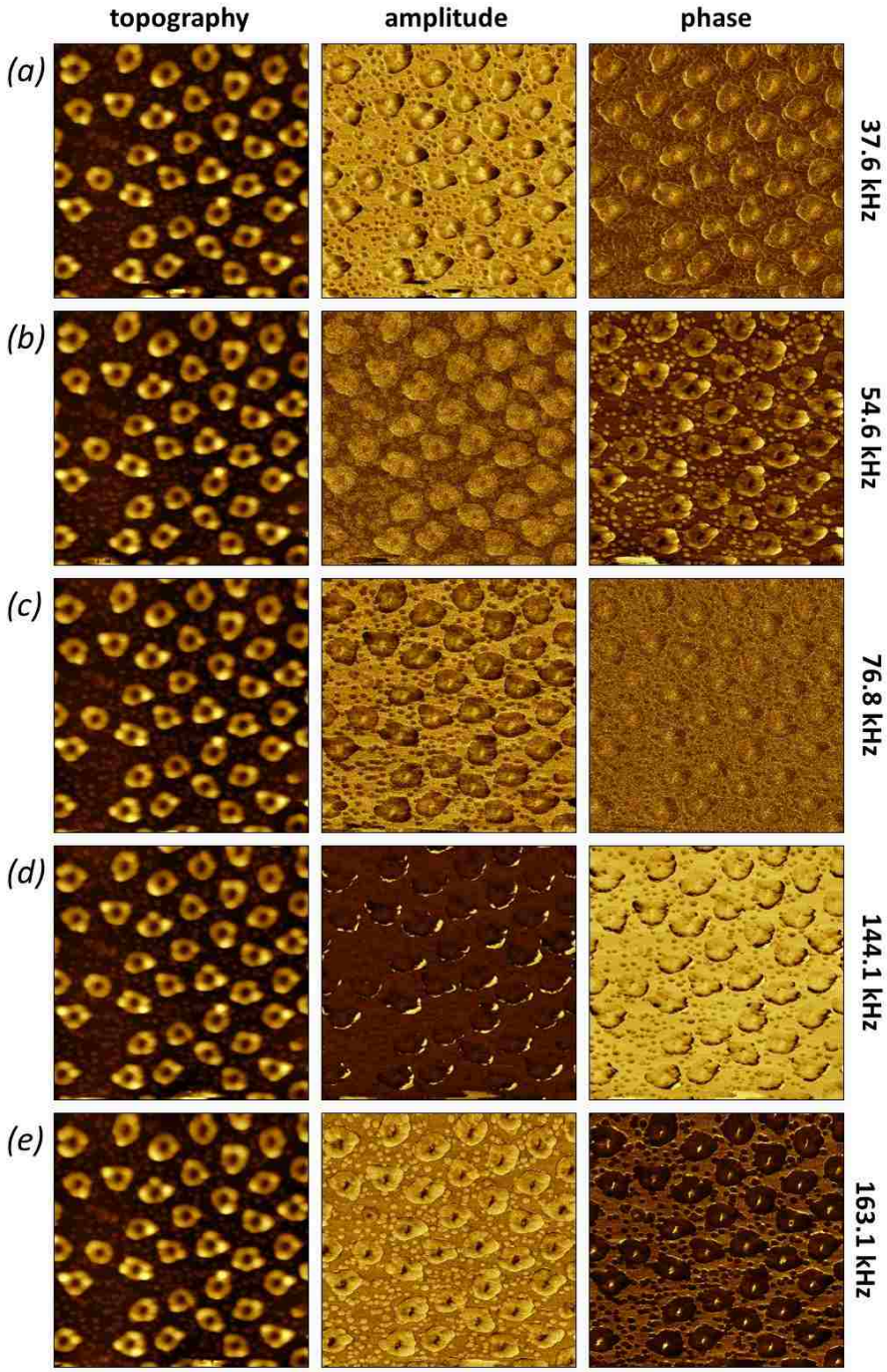

Figure 7.4 Nanorings of CMPS imaged with IMM at selected driving frequencies. Image sizes are 3 x 3 μm^2.

phase images, more clear contrast can be viewed at frequencies of 54.6 and 163.1 kHz than the other three. The difference of the center of the nanoring and the surrounding area can be viewed from amplitude images of a, c, e and phase images of b and e.

7.3.4 High Resolution Stage-driven FMM and Tip-driven IMM Images of CMPS Nanorings

Three individual CMPS nanorings were imaged with FMM in the 800 × 800 nm^2 scan area (Figure 7.5a). The morphology of the nanorings can be seen from the topograph, while the small nanopillars cannot be resolved clearly due to the significant difference in heights between the nanopillars and the nanorings. The high resolution amplitude frame gives more details about this sample surface. First, each nanoring structure is not homogeneous. Instead, slight height and morphology differences can be seen along a single nanoring. Second, the individual CMPS nanopillars beside the nanorings can be seen clearly. Third, light contrast in the center of the nanoring and dark contrast of the nanorings proves that the multilayer of CMPS nanoring is the softest area on the surface and the center of the nanoring is the hardest. The viscoelasticity difference can be viewed in the phase image with sharp contrast. The height difference of the nanoring, the center of the nanoring, and the nanopillars is shown by the cursor profile (white line in the topograph). The CMPS nanoring is 24.2 nm tall, which corresponds to more than 30 layers of the CMPS silane. The center of the nanoring is 1.8 nm lower than the surrounding area, which suggests there is a monolayer or double layer in the areas between the nanorings.

Three individual CMPS nanorings are viewed in the 800 × 800 nm^2 area acquired with tip-driven IMM (Figure 7.5b) in comparison with stage-driven FMM. The shape of the nanorings and the nanopillars in the surrounding area can be seen from the topograph. The center of the nanoring has a darker color contrast because it is the bare silicon substrate, which is the lowest point on surface. The morphology of each individual nanoring is not homogeneous which is determined by the local difference of the silane reaction. The amplitude frame does not give a clear elasticity

difference of the features on surface compared with FMM images. The nanorings and the nanopillars do have a slightly darker contrast than the center of the nanoring and the surrounding area, which indicates a softer nature of the material. However, the difference is not as distinct as zoom-in images of FMM. The difference in viscoelasticity between nanorings and nanopillars, with center of the nanoring and the surrounding area are clearly viewed in the phase frame. However, some dark edge effects can be seen in this phase frame beside the features, which cannot be seen from the zoom-in images of FMM. The height of the nanoring is shown in the cursor profile of the white line in topograph. The CMPS nanoring is 33.4 nm tall. The center of the nanoring is 2.5 nm deeper than the surrounding area, which indicates there are CMPS silanes binding on the silicon substrate in the areas between the nanorings during the vapor deposition step.

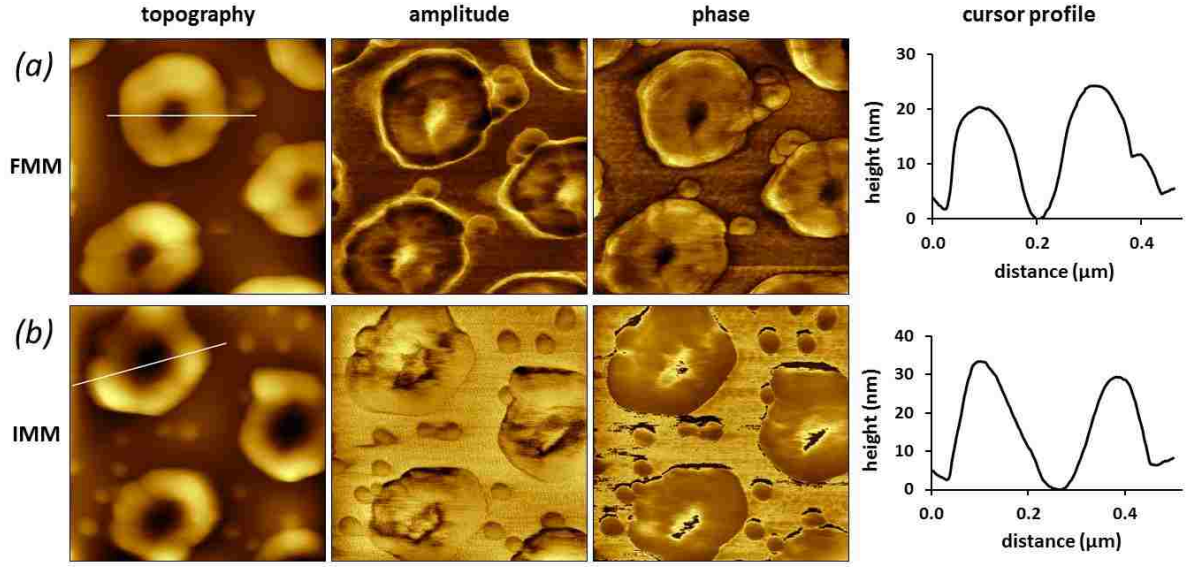

Figure 7.5 Close-up view of three CMPS nanorings (800 × 800 nm^2) scanned by (a) FMM and (b) IMM at frequencies of 14.5 kHz and 155.2 kHz, respectively, with corresponding cursor profiles.

7.3.5 Frequency Sweeps of FMM at Selected Regions of the Sample Surface

Four regions have been selected to conduct a frequency scan to gather information about tip-sample interactions as a function of induced vibrational frequency. Four regions are labeled in Figure 7.6a as: 1) CMPS nanorings (multilayers of CMPS), 2) the center of the nanoring (bare

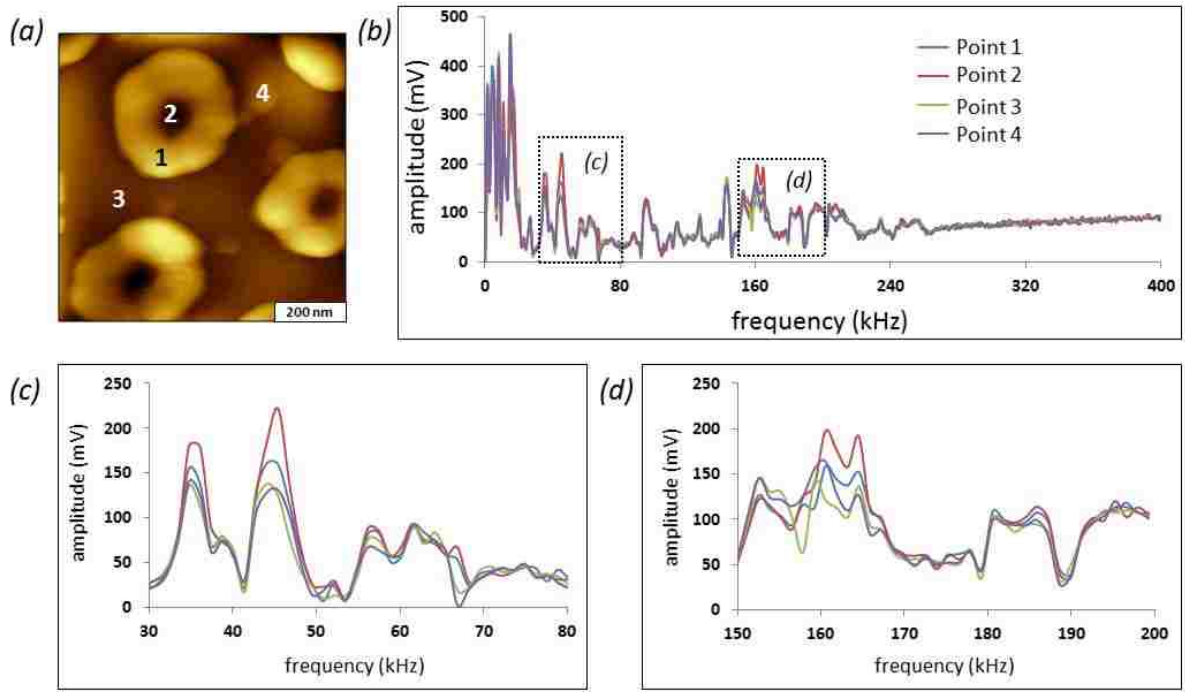

Figure 7.6 Frequency-dependent study with stage-driven FMM at selected regions of the sample surface. (a) Topograph view with four regions labeled, (b) full spectrum of the frequency sweep and two zoom-in spectra of (c) and (d).

silicon substrate), 3) areas between nanorings (monolayer of CMPS), and 4) CMPS nanopillars (couple layers). The AFM tip was placed on the four regions to acquire the frequency sweeps. The reflection of the local mechanical differences of the four points is shown in the amplitude-frequency plot of Figure 7.6. The frequency sweeps were acquired when the sample stage vibration was on. In the frequency range of 0-400 kHz, most areas of the four frequency spectra are overlapping except in the range between 30-80 kHz and around 160 kHz as shown in the two zoom-in frequency sweeps (Figures 7.6c and d). The resonance peaks from the frequency sweeps

come from the natural resonance of the piezoactuator embedded in the stage, the tip-holder assembly, and the vibration of the sample. This is why most of them are overlapping between the four frequency sweeps. At the frequency between 30-80 kHz and around 160 kHz, there is a slightly frequency shift and an amplitude difference between the four points measured. The amplitude of point 2 is the largest within the four spectrum because point 2 is the stiffest region of the four. The differences between the four frequency sweeps is due to the local elasticity differences of the sample surface as it interacts with the tip. When the sample stage is vibrating, the interaction difference is amplified and shown in the frequency sweeps.

7.3.6 Frequency Sweeps of IMM at Selected Regions of the Sample Surface

To compare with the FMM study, four similar regions were chosen to conduct the frequency scans on. Four regions are labeled in Figure 7.7a as the same way as Figure 7.6a: 1) CMPS nanorings, 2) the center of the nanoring, 3) areas between nanorings, and 4) CMPS nanopillars. The AFM tip was placed on the four regions separately to acquire frequency plots. The tip-sample interactions of the four regions are shown in the amplitude-frequency plot of Figure 7.7b. In the frequency range of 0-400 kHz, similar to FMM, most areas of the four frequency spectra are overlapping except around the frequency of 160 kHz as shown in the large-view plot (Figure 7.7b) and the zoom-in frequency sweep (Figure 7.7d). In the selected region of frequency 30-90 kHz (Figure 7.7c), the spectrum overlapping can be clearly seen. The resonance peaks from the frequency sweeps are coming from the natural resonance of the tip-holder assembly, the metal pins in the nosecone and the AFM probe. At frequency around 160 kHz, there is a clear frequency shift within the four regions measured. The differences between the four frequency sweeps around 160 kHz is due to the difference of the material's local elasticity so that the AFM tip dampened differently. When the AFM tip is vibrating along with the nosecone in the flux of magnetic field, the interaction difference is amplified and shown in the frequency sweeps. The amplitude of point

1 is the largest between the four at frequency ~160 kHz, not point 2 in FMM. To our understanding, point 2 should have largest amplitude since it is the stiffest region within the four. Therefore, we

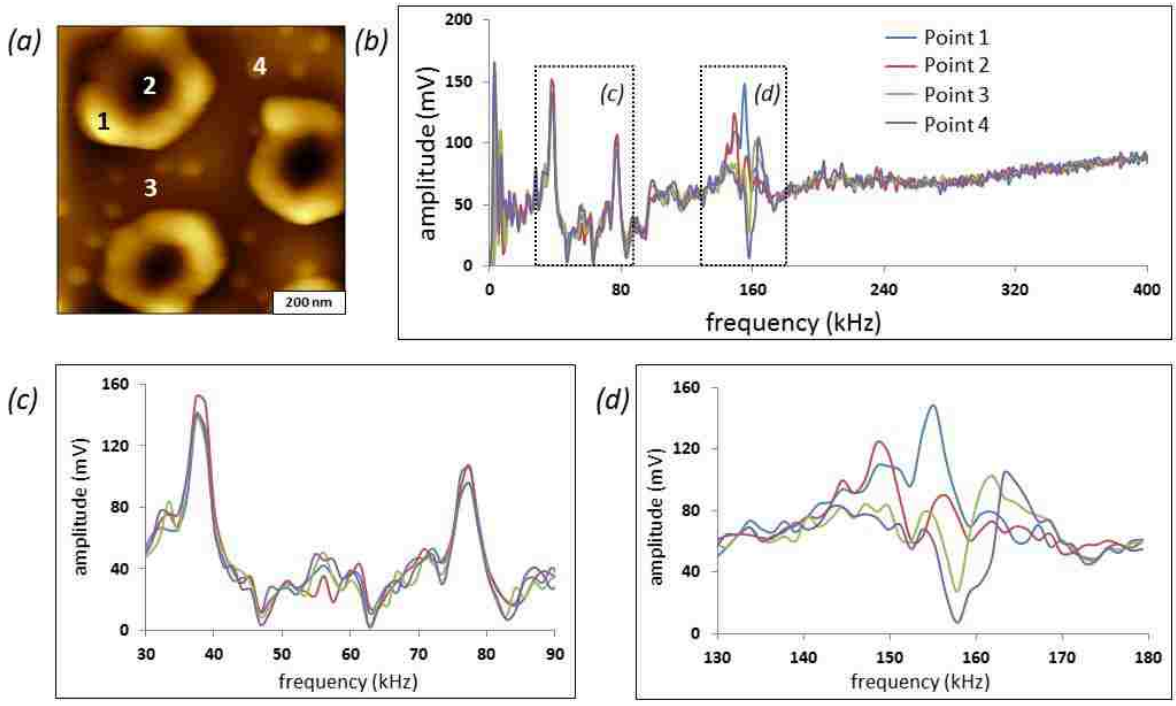

Figure 7.7 Frequency-dependent study with tip-driven IMM at selected regions of the sample surface. (A) Topograph view with four regions labeled, (B) full spectrum of the frequency sweep and two zoom-in spectra of C and D.

think stage-driven FMM is a more reliable way to test the mechanical differences on surface compared with tip-driven IMM.

7.3.7 Dynamic Stage-driven FMM and Tip-driven IMM Studies

A dynamic FMM study has been done by successfully changing the driving frequency without interruption of the data acquisition (Figure 7.8a). The dynamic study has no influence on the topography image, but distinct color changes can be seen in the amplitude and phase frames, especially when changing the frequency from 11.5 to 16.3 kHz and 95.6 to 152.4 kHz. The contrast

at frequency of 16.3 kHz is not as clear as in Figure 7.3, which is because the color magnitude change during imaging processing for the five frequencies in one single AFM image.

A dynamic study of the CMPS nanorings sample using IMM is shown in Figure 7.8b. Frequency was changed without the interruption of data acquisition. The changing of the frequency

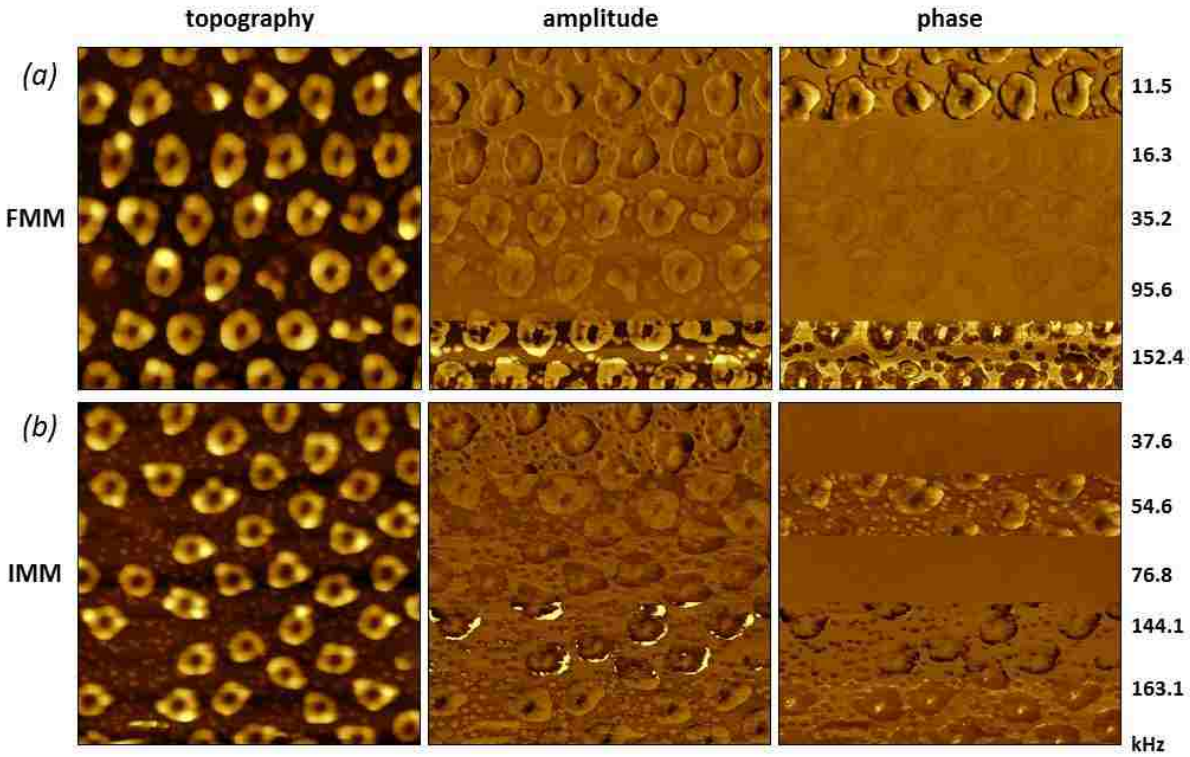

Figure 7.8 Dynamic (a) stage-driven FMM and (b) tip-driven IMM study of CMPS nanorings by incrementally changing the driving frequency during a single scan. Image sizes are 3 × 3 μm^2.

has no influence on the topography image, while clear edges can be viewed at the point when frequency changed in the amplitude and phase frames. Again, due the dynamic nature of this study, there is a decrease in contrast quality in both the amplitude and phase images. Dynamic FMM and IMM studies are efficient ways to find out best frequencies for force modulation microscopy.

7.3.8 Side-by-side Comparison of FMM and IMM at the Same Driving Frequencies.

Comparison of FMM and IMM at fourteen frequencies was done, with three sets of data displayed in Figure 7.9 while the other eleven are shown in the Appendix E as individual figures. Topography, amplitude and phase frames are all displayed separately. Frequencies of 16.3, 40.1, and 143.5 kHz were chosen to show the frequency-dependent property of this sample in Figure 7.9. The exact same AFM tip was used to acquire AFM images of both FMM and IMM at the fourteen selected frequencies. The difference in the shape of the nanorings between FMM images and IMM images is because different areas of the sample surface were scanned. The exact same area on sample surface cannot be imaged for both IMM and FMM because two sample stages are required for each method. In general, for amplitude and phase frames, FMM has a more distinct color contrast when compared with IMM (Figure 7.9). Nanorings of CMPS are softer than the background; therefore, darker contrast of the nanorings in the amplitude channel is expected. Within the three selected driving frequencies, the results from frequencies of 16.3 and 143.5 kHz of FMM are reasonable (amplitude frames), while none of them in IMM are corresponding with theoretical expectations. For the phase images, the frequency of 40.1 kHz for FMM gives the best contrast to show the difference in the viscoelasticity of components on the sample surface.

The frequency sweeps for the side-by-side comparison of stage-driven FMM and tip-driven IMM are shown in Figure 7.10. The same amount of voltage (0.5 V) was applied to the newly-designed force modulation sample stage for FMM and MAC-mode sample stage for IMM. Smaller resonance peaks can be seen from Figure 7.10 for IMM frequency sweep. This is because in FMM, the voltage is directly applied to the force modulation sample stage to generate the vibration of the piezoactuator; while in IMM, the ac current was applied to the solenoid underneath the MAC-mode sample stage to generate an external electromagnetic field to indirectly modulate the nosecone assembly. A series of frequencies listed in the plot were used to acquire the FMM and

IMM images. The reason to display FMM and IMM images of frequencies at 16.3, 40.1, and 143.5 kHz in Figure 7.9 is because: resonance peaks shown up at 16.3 kHz for both method; no resonance

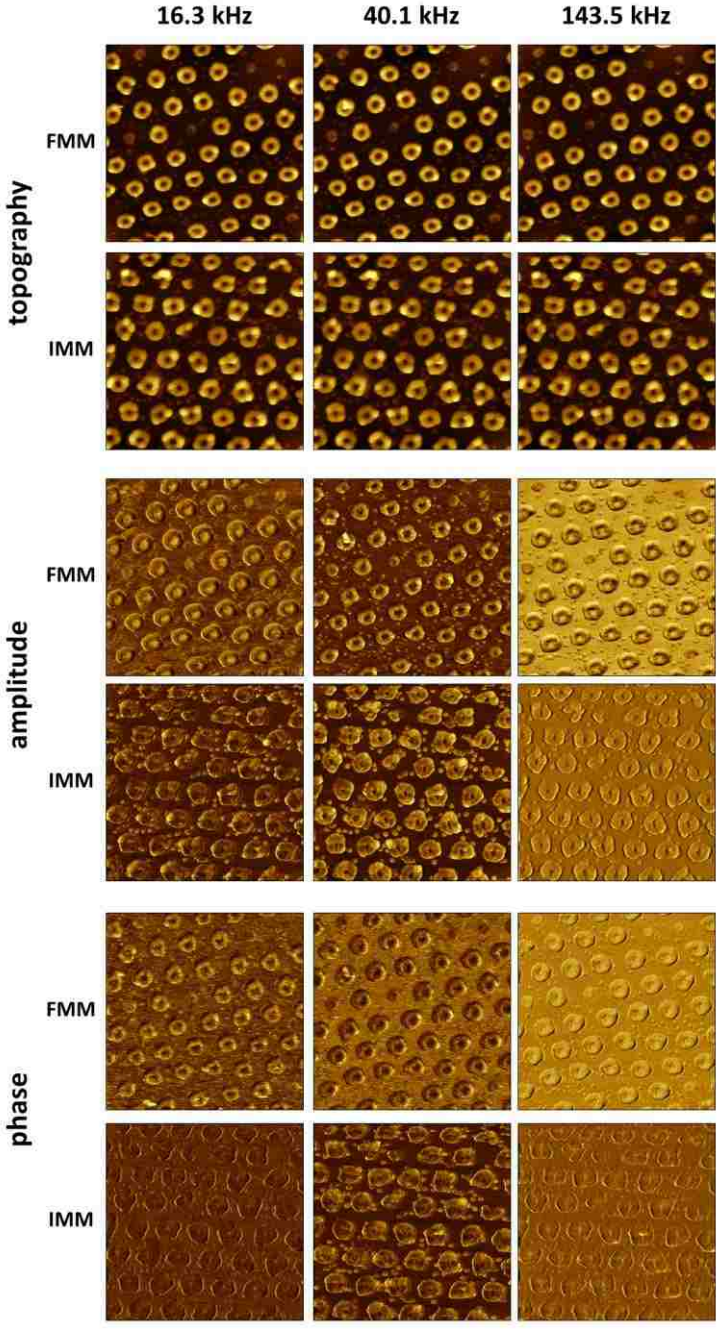

Figure 7.9 Comparison of stage-driven FMM and tip-driven IMM: (top) topography, (middle) amplitude, and (bottom) phase, of CMPS nanorings at matching driving frequencies. Image sizes are 3×3 μm^2. Images were obtained and compared at frequencies of 16.3 kHz, 40.1 kHz, and 143.5 kHz.

peaks shown up at 40.1 kHz; only resonance peak shown up for FMM at 143.5 kHz. There is not necessary to acquire force modulation images at frequencies of resonance peak areas since at frequency of 40.1 kHz clear contrast still show up.

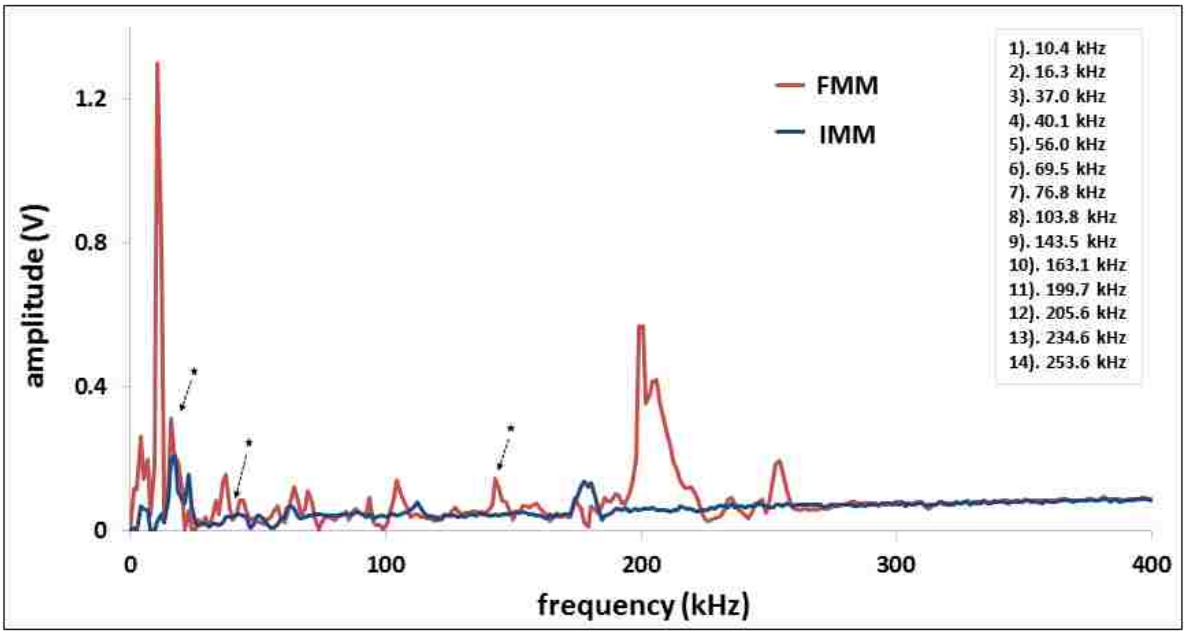

Figure 7.10 Overlay of frequency spectra obtained with (red) stage-driven FMM and (blue) tip-driven IMM. Stars indicate frequencies from Figure 7.9 that were used to compare the two types of modulation.

7.4 Discussion

To compare the difference of two force modulation methods, FMM and IMM, the exact same AFM tip was used from Figure 7.2 to Figure 7.8, another tip for Figures 7.9-7.10 and all figures shown in supporting information. The reason we have to switch to the second tip is because tip broadening was noticed after multiple uses of the previous tip. However, both of the AFM tips are the same type and have the same spring constant of 0.1 N m^{-1}.

To acquire frequency sweeps for both FMM and IMM at selected regions of the surface to compare the mechanical responses, close-up views were required so that the tip can be accurately placed on distinct surface features. Multiple regions have been used to acquire the frequency

sweeps to prove that the differences in the elasticity of the sample cause a frequency shift around 160 kHz for this sample. Based on the previous discussion in this paper, more reliable information can be obtained from the frequency sweep from stage-driven FMM.

By inputting same amount of voltage to the sample stage, more amplitude response in FMM than IMM was detected. This is because the current applied to the FMM piezoactuator is directly vibrating the sample stage, while the current for IMM stage is to generate magnetic field, then the nosecone is vibrated by the flux of the magnetic field. Higher resolution images were acquired using FMM than IMM (Figures 7.5). More surface details can be found from this zoom-in view of FMM than IMM. Based on our experience, it is easier to acquire data using FMM because IMM is more sensitive to the environment noise and vibration and usually takes longer time for the AFM to stabilize.

7.5 Conclusion

Nanoring patterns of 4-(chloromethyl)phenyltrichlorosilane (CMPS) were prepared with particle lithography combined with silane vapor deposition. This test platform is a good candidate for force modulation studies because of the range of elasticities present in the features of the surface. The influences of modulation and non-modulation, driving frequency, and vibrational response have been studied for both force modulation microscopy (FMM) and indirect magnetic modulation (IMM). The images of FMM and IMM at the exact same driving frequencies have been compared and discussed. The method of FMM using the newly-designed sample stage proved to be an easier, more efficient way to obtain high resolution AFM images that can be used to compare local mechanical differences on a sample.

CHAPTER 8. CONCLUSIONS AND FUTURE PROSPECTUS

Nanopores within a film of organosilane were used as miniature containers for depositing initiators for surface initiated polymerization. Nanostructures of poly(*N*-allyl glycine) were generated on Si(111) using particle lithography. Experimental results were characterized step-by-step with high resolution AFM. The nanostructured surface platform has potential application in smart coatings, drug delivery, and bioseparations due to the biocompatibility, backbone degradability and thermal processability of the polymer. For future studies, other polymeric materials can be patterned on surfaces using the protocols developed in this dissertation.

Thermo-responsive copolypeptoids were pre-synthesized and attached onto patterned organosilanes using thiol-ene click reaction. The polymer has a narrower distribution of heights when using the "graft to" approach. Phase transitions of the polymer nanostructures were investigated using *in situ* AFM at the molecular level. Experimental results were compared with a turbidity assay for the aqueous solution of the bulk material. Higher sensitivity was observed with the *in situ* AFM study of the shrinkage and entanglement of the polymer chain. The phase transition of other systems can be studied with this approach for future studies. Further investigations of this platform in biosensor applications should be promising because of the excellent biocompatibility of polypeptoids.

Force modulation microscopy (FMM) is commonly used to acquire mechanical properties of samples concurrent with topographic information. The FMM mode is particularly useful for studying polymer samples and organic thin films. A sample stage for FMM constructed of machined polycarbonate was designed and tested. The designed FMM sample stage is compatible with a tip-mounted AFM configuration. A piezoactuator was mounted within the sample stage to drive the vibration of the sample in the z-direction. Information of elastic or viscoelastic properties of samples can be acquired with FMM. Three samples with increasing complexity were selected

to test the capabilities of the FMM stage design. High resolution AFM results concurrent with sample elasticity can be acquired. Future studies will incorporate a liquid cell for the design of the FMM stage to enable characterizations in liquids. Machined glass components will be used for constructing a sample stage to enable studies in solvents.

REFERENCES

1. Binnig, G.; Quate, C. F.; Gerber, C., Atomic force microscope. *Phys. Rev. Lett.* **1986,** *56,* 930-933.

2. Hansma, H. G., Surface biology of DNA by atomic force microscopy. *Annu. Rev. Phys. Chem.* **2001,** *52,* 71-92.

3. Hansma, P. K.; Elings, V. B.; Marti, O.; Bracker, C. E., Scanning tunneling microscopy and atomic force microscopy - application to biology and technology. *Science* **1988,** *242,* 209-216.

4. Hoh, J. H.; Hansma, P. K., Atomic force microscopy for high-resolution imaging in cell biology. *Trends cell biol.* **1992,** *2,* 208-213.

5. Zhong, Q.; Inniss, D.; Kjoller, K.; Elings, V. B., Fractured polymer silica fiber surface studied by tapping mode atomic-force microscopy. *Surf. Sci.* **1993,** *290,* L688-L692.

6. Magonov, S. N.; Reneker, D. H., Characterization of polymer surfaces with atomic force microscopy. *Annu. Rev. Mater. Sci.* **1997,** *27,* 175-222.

7. Bar, G.; Thomann, Y.; Brandsch, R.; Cantow, H. J.; Whangbo, M. H., Factors affecting the height and phase images in tapping mode atomic force microscopy. Study of phase-separated polymer blends of poly(ethene-co-styrene) and poly(2,6-dimethyl-1,4-phenylene oxide). *Langmuir* **1997,** *13,* 3807-3812.

8. Mativetsky, J. A.; Palma, M.; Samori, P., Exploring electronic transport in molecular junctions by conducting atomic force microscopy. In *STM and AFM Studies on (bio)molecular systems: Unravelling the nanoworld,* Samori, P., Ed. 2008; Vol. 285, pp 157-202.

9. Mueller, D. J.; Dufrene, Y. F., Atomic force microscopy as a multifunctional molecular toolbox in nanobiotechnology. *Nature Nanotech.* **2008,** *3,* 261-269.

10. Archakov, A. I.; Ivanov, Y. D., Analytical nanobiotechnology for medicine diagnostics. *Mol. Biosyst.* **2007,** *3,* 336-342.

11. Goksu, E. I.; Vanegas, J. M.; Blanchette, C. D.; Lin, W.-C.; Longo, M. L., AFM for structure and dynamics of biomembranes. *BBA-Biomembranes* **2009,** *1788,* 254-266.

12. Fang, F. Z.; Venkatesh, V. C., Diamond cutting of silicon with nanometric finish. *CIRP Annals - Manuf. Technol.* **1998,** *47,* 45-49.

13. Binnig, G.; Gerber, C.; Stoll, E.; Albrecht, T. R.; Quate, C. F., Atomic resolution with atomic force microscope. *Europhys. Lett.* **1987,** *3,* 1281-1286.

14. Maivald, P.; Butt, H. J.; Gould, S. A. C.; Prater, C. B.; Drake, B.; Gurley, J. A.; Elings, V. B.; Hansma, P. K., Using force modulation to image surface elasticities with the atomic force microscope *Nanotechnology* **1991,** *2,* 103-106.

15. Lu, L., Xu, S., Zhang, D., Garno, J. C., Sample stage designed for force modulation microscopy using a tip-mounted AFM scanner. *Anal. Chem.* **2015**, in submission.

16. Li, J.-R.; Garno, J. C., Indirect modulation of nonmagnetic probes for force modulation atomic force microscopy. *Anal. Chem.* **2009,** *81*, 1699-1706.

17. Caron, A.; Rabe, U.; Reinstadtler, M.; Turner, J. A.; Arnold, W., Imaging using lateral bending modes of atomic force microscope cantilevers. *Appl. Phys. Lett.* **2004,** *85*, 6398-6400.

18. Lehmani, A.; Durand-Vidal, S.; Turq, P., Surface morphology of Nafion 117 membrane by tapping mode atomic force microscope. *J. Appl. Poly. Sci.* **1998,** *68*, 503-508.

19. Prior, M.; Makarovski, A.; Finkelstein, G., Low-temperature conductive tip atomic force microscope for carbon nanotube probing and manipulation. *Appl. Phys. Lett.* **2007,** *91*,053112/1-053112-3.

20. Saenz, J. J.; Garcia, N.; Grutter, P.; Meyer, E.; Heinzelmann, H.; Wiesendanger, R.; Rosenthaler, L.; Hidber, H. R.; Gunterodt, H. J., Observation of magnetic forces by the atomic force microscope. *J. Appl. Phys.* **1987,** *62*, 4293-4295.

21. Reviakine, I.; Bergsma-Schutter, W.; Brisson, A., Growth of protein 2-d crystals on supported planar lipid bilayers imaged in situ by AFM. *J. Struct. Biol.* **1998,** *121*, 356-362.

22. Beaulieu, L. Y.; Hatchard, T. D.; Bonakdarpour, A.; Fleischauer, M. D.; Dahn, J. R., Reaction of Li with alloy thin films studied by in situ AFM. *J. Electrochem. Soc.* **2003,** *150*, A1457-A1464.

23. Tamada, K.; Hara, M.; Sasabe, H.; Knoll, W., Surface phase behavior of n-alkanethiol self-assembled monolayers adsorbed on Au(111): An atomic force microscope study. *Langmuir* **1997,** *13*, 1558-1566.

24. Wenzler, L. A.; Moyes, G. L.; Raikar, G. N.; Hansen, R. L.; Harris, J. M.; Beebe, T. P.; Wood, L. L.; Saavedra, S. S., Measurements of single-molecule bond rupture forces between self-assembled monolayers of organosilanes with the atomic force microscope. *Langmuir* **1997,** *13*, 3761-3768.

25. Drake, B.; Prater, C. B.; Weisenhorn, A. L.; Gould, S. A. C.; Albrecht, T. R.; Quate, C. F.; Cannell, D. S.; Hansma, H. G.; Hansma, P. K., Imaging crystals, polymers and processes in water with the atomic force microscope. *Science* **1989,** *243*, 1586-1589.

26. Domke, J.; Radmacher, M., Measuring the elastic properties of thin polymer films with the atomic force microscope. *Langmuir* **1998,** *14*, 3320-3325.

27. Rong, W. Z.; Pelling, A. E.; Ryan, A.; Gimzewski, J. K.; Friedlander, S. K., Complementary TEM and AFM force spectroscopy to characterize the nanomechanical properties of nanoparticle chain aggregates. *Nano Lett.* **2004,** *4*, 2287-2292.

28. Hoo, C. M.; Starostin, N.; West, P.; Mecartney, M. L., A comparison of atomic force microscopy (AFM) and dynamic light scattering (DLS) methods to characterize nanoparticle size distributions. *J. Nanopart. Res.* **2008,** *10*, 89-96.

29. Kidoaki, S.; Matsuda, T., Adhesion forces of the blood plasma proteins on self-assembled monolayer surfaces of alkanethiolates with different functional groups measured by an atomic force microscope. *Langmuir* **1999,** *15*, 7639-7646.

30. Fisher, T. E.; Oberhauser, A. F.; Carrion-Vazquez, M.; Marszalek, P. E.; Fernandez, J. M., The study of protein mechanics with the atomic force microscope. *Trends Biochem. Sci.* **1999,** *24*, 379-384.

31. Sen, S.; Subramanian, S.; Discher, D. E., Indentation and adhesive probing of a cell membrane with AFM: Theoretical model and experiments. *Biophys. J.* **2005,** *89*, 3203-3213.

32. Li, Q. S.; Lee, G. Y. H.; Ong, C. N.; Lim, C. T., AFM indentation study of breast cancer cells. *Biochem. Biophys. Res. Commun.* **2008,** *374*, 609-613.

33. Thomson, N. H.; Kasas, S.; Smith, B.; Hansma, H. G.; Hansma, P. K., Reversible binding of DNA to mica for AFM imaging. *Langmuir* **1996,** *12*, 5905-5908.

34. Allen, M. J.; Bradbury, E. M.; Balhorn, R., AFM analysis of DNA-protamine complexes bound to mica. *Nucleic Acids Res.* **1997,** *25*, 2221-2226.

35. Singjai, P.; Zhdan, P. A.; Castle, J. E., Observations on the full honeycomb structure of graphite as imaged by atomic force microscopy. *Philos. mag. A* **2000,** *80*, 2445-2456.

36. Arai, T.; Fujihira, M., Effect of tip shape on force distance curves for AFM in aqueous-electrolytes. *J. Electroanal. Chem.* **1994,** *374*, 269-273.

37. Kraemer, G.; Griepentrog, M.; Bonaccurso, E.; Cappella, B., Study of morphology and mechanical properties of polystyrene-polybutadiene blends with nanometre resolution using AFM and force-distance curves. *Eur. Polym. J.* **2014,** *55*, 123-134.

38. Cappella, B.; Baschieri, P.; Frediani, C.; Miccoli, P.; Ascoli, C., Improvements in AFM imaging of the spatial variation of force-distance curves: On-line images. *Nanotechnology* **1997,** *8*, 82-87.

39. Waltman, R. J.; Guo, X. C., AFM force-distance curves for perfluoropolyether boundary lubricant films as a function of molecular polarity. *Tribol. Lett.* **2012,** *45*, 275-289.

40. Grinevich, O.; Mejiritski, A.; Neckers, D. C., AFM force-distance curve methods for measuring the kinetics of silicon chemical etching and reactions between silylating agents and a silicon surface. *Langmuir* **1999,** *15*, 2077-2079.

41. Cappella, B.; Kaliappan, S. K.; Sturm, H., Using AFM force-distance curves to study the glass-to-rubber transition of amorphous polymers and their elastic-plastic properties as a function of temperature. *Macromolecules* **2005,** *38*, 1874-1881.

42. Kaliappan, S. K.; Cappella, B., Temperature dependent elastic-plastic behaviour of polystyrene studied using AFM force-distance curves. *Polymer* **2005,** *46*, 11416-11423.

43. Cappella, B.; Stark, W., Adhesion of amorphous polymers as a function of temperature probed with AFM force-distance curves. *J. Colloid Interface Sci.* **2006,** *296*, 507-514.

44. Kim, K.-S.; Lin, Z.; Shrotriya, P.; Sundararajan, S.; Zou, Q., Iterative control approach to high-speed force-distance curve measurement using AFM: Time-dependent response of PDMS example. *Ultramicroscopy* **2008,** *108*, 911-920.

45. Ebenstein, Y.; Nahum, E.; Banin, U., Tapping mode atomic force microscopy for nanoparticle sizing: Tip-sample interaction effects. *Nano Lett.* **2002,** *2*, 945-950.

46. Bar, G.; Thomann, Y.; Whangbo, M. H., Characterization of the morphologies and nanostructures of blends of poly(styrene) block-poly(ethene-co-but-1-ene)-block-poly(styrene) with isotactic and atactic polypropylenes by tapping-mode atomic force microscopy. *Langmuir* **1998,** *14*, 1219-1226.

47. Betley, T. A.; Holl, M. M. B.; Orr, B. G.; Swanson, D. R.; Tomalia, D. A.; Baker, J. R., Tapping mode atomic force microscopy investigation of poly(amidoamine) dendrimers: Effects of substrate and pH on dendrimer deformation. *Langmuir* **2001,** *17*, 2768-2773.

48. Stocker, W.; Beckmann, J.; Stadler, R.; Rabe, J. P., Surface reconstruction of the lamellar morphology in a symmetric poly(styrene-block-butadiene-block-methyl methacrylate) triblock copolymer: A tapping mode scanning force microscope study. *Macromolecules* **1996,** *29*, 7502-7507.

49. Moller, C.; Allen, M.; Elings, V.; Engel, A.; Muller, D. J., Tapping-mode atomic force microscopy produces faithful high-resolution images of protein surfaces. *Biophys. J.* **1999,** *77*, 1150-1158.

50. Fritz, M.; Radmacher, M.; Cleveland, J. P.; Allersma, M. W.; Stewart, R. J.; Gieselmann, R.; Janmey, P.; Schmidt, C. F.; Hansma, P. K., Imaging globular and filamentous proteins in physiological buffer solutions with tapping mode atomic-force micrscopy. *Langmuir* **1995,** *11*, 3529-3535.

51. Zhong, Q.; Inniss, D.; Kjoller, K.; Elings, V. B., Fractured polymer/silica fiber surface studied by tapping mode atomic force microscopy. *Surf. Sci.* **1993,** *290*, L688-L692.

52. Hansma, P. K.; Cleveland, J. P.; Radmacher, M.; Walters, D. A.; Hillner, P. E.; Bezanilla, M.; Fritz, M.; Vie, D.; Hansma, H. G.; Prater, C. B.; Massie, J.; Fukunaga, L.; Gurley, J.; Elings, V., Tapping mode atomic force microscopy in liquids. *Appl. Phys. Lett.* **1994,** *64*, 1738-1740.

53. Putman, C. A. J.; Vanderwerf, K. O.; Degrooth, B. G.; Vanhulst, N. F.; Greve, J., Tapping mode atomic-force microscopy in liquid. *Appl. Phys. Lett.* **1994,** *64*, 2454-2456.

54. Schmitz, I.; Schreiner, M.; Friedbacher, G.; Grasserbauer, M., Phase imaging as an extension to tapping mode AFM for the identification of material properties on humidity-sensitive surfaces. *Appl. Surf. Sci.* **1997,** *115*, 190-198.

55. Tamayo, J.; García, R., Deformation, contact time, and phase contrast in tapping mode scanning force microscopy. *Langmuir* **1996,** *12*, 4430-4435.

56. Li, J.-R.; Garno, J. C., Elucidating the role of surface hydrolysis in preparing organosilane nanostructures via particle lithography. *Nano Lett.* **2008,** *8*, 1916-1922.

57. Raghavan, D.; Gu, X.; Nguyen, T.; VanLandingham, M.; Karim, A., Mapping polymer heterogeneity using atomic force microscopy phase imaging and nanoscale indentation. *Macromolecules* **2000,** *33*, 2573-2583.

58. Kapaklis, V.; Grammatikopoulos, S.; Sordan, R.; Miranda, A.; Traversi, F.; von Kanei, H.; Trachylis, D.; Poulopoulos, P.; Politis, C., Nanolithographic templates using diblock copolymer films on chemically heterogeneous substrates. *J. Nanosci. Nanotechnol.* **2010,** *10*, 6056-6061.

59. Schon, P.; Bagdi, K.; Molnar, K.; Markus, P.; Pukanszky, B.; Vancso, G. J., Quantitative mapping of elastic moduli at the nanoscale in phase separated polyurethanes by AFM. *Eur. Polym. J.* **2011,** *47*, 692-698.

60. Wilbur, J. L.; Biebuyck, H. A.; Macdonald, J. C.; Whitesides, G. M., Scanning force microscopies can image patterned self-assembled monolayers. *Langmuir* **1995,** *11*, 825-831.

61. Nysten, B.; Legras, R.; Costa, J. L., Atomic-force microscopy imaging of viscoelastic properties in toughened polyppopylene resins. *J. Appl. Phys.* **1995,** *78*, 5953-5958.

62. Nie, H. Y.; Motomatsu, M.; Mizutani, W.; Tokumoto, H., Local modification of elastic properties of polystyrene-polyethyleneoxide blend surfaces. *J. Vac. Sci. Technol. B* **1995,** *13*, 1163-1166.

63. Galuska, A. A.; Poulter, R. R.; McElrath, K. O., Force modulation AFM of elastomer blends: Morphology, fillers and cross-linking. *Surf. Interface Anal.* **1997,** *25*, 418-429.

64. Gilmore, I. S.; Seah, M. P.; Johnstone, J. E., Quantification issues in ToF-SSIMS and AFM co-analysis in two-phase systems, exampled by a polymer blend. *Surf. Interface Anal.* **2003,** *35*, 888-896.

65. Krol, S.; Ross, M.; Sieber, M.; Kunneke, S.; Galla, H. J.; Janshoff, A., Formation of three-dimensional protein-lipid aggregates in monolayer films induced by surfactant protein B. *Biophys. J.* **2000,** *79*, 904-918.

66. Clair, B.; Arinero, R.; Leveque, G.; Ramonda, M.; Thibaut, B., Imaging the mechanical properties of wood cell wall layers by atomic force modulation microscopy. *Iawa J.* **2003,** *24*, 223-230.

67. Haga, H.; Nagayama, M.; Kawabata, K., Imaging mechanical properties of living cells by scanning probe microscopy. *Curr. Nanosci.* **2007,** *3*, 97-103.

68. Sasaki, S.; Morimoto, M.; Haga, H.; Kawabata, K.; Ito, E.; Ushiki, T.; Abe, K.; Sambongi, T., Elastic properties of living fibroblasts as imaged using force modulation mode in atomic force microscopy. *Arch. of Histol. Cytol.* **1998,** *61*, 57-63.

69. Fritz, M.; Radmacher, M.; Petersen, N.; Gaub, H. E., Visuallization and identification of intracellular structures by force modulation microscopy and drug-induced degradation. *J. Vac. Sci. Technol. B* **1994,** *12*, 1526-1529.

70. Sbrana, F.; Ghulinyan, M.; Pavesi, L., Force modulation microscopy of multilayered porous silicon samples. *Phys. Status Solidi A* **2005,** *202*, 1492-1496.

71. Sahoo, N.; Thakur, S.; Senthilkumar, M.; Das, N. C., Surface viscoelasticity studies of Gd_2O_3, SiO_2 optical thin films and multilayers using force modulation and force-distance scanning probe microscopy. *Appl. Surf. Sci.* **2003,** *206*, 271-293.

72. Resch, R.; Friedbacher, G.; Grasserbauer, M.; Kanniainen, T.; Lindroos, S.; Leskela, M.; Niinisto, L., Lateral force microscopy and force modulation microscopy on SILAR-grown lead sulfide samples. *Appl. Surf. Sci.* **1997,** *120*, 51-57.

73. Wozniak, M. J.; Ryszkowska, J.; Szymborski, T.; Chen, G.; Tateishi, T.; Kurzydlowski, K. J., Application of phase imaging and force modulation mode for description of dispersion of carbon nanotubes in polyol matrix. *Mater. Sci-Poland* **2008,** *26*, 245-253.

74. Schonherr, H.; Tocha, E.; Vancso, G. J., Friction and surface dynamics of polymers on the nanoscale by AFM. In *STM and AFM Studies on (bio)molecular system: unravelling the nanoworld*, Samori, P., Ed. 2008; Vol. 285, pp 103-156.

75. DeVecchio, D.; Bhushan, B., Localized surface elasticity measurements using an atomic force microscope. *Rev. Sci. Instrum.* **1997,** *68*, 4498-4505.

76. Troyon, M.; Wang, Z.; Pastre, D.; Lei, H. N.; Hazotte, A., Force modulation microscopy for the study of stiff materials. *Nanotechnology* **1997,** *8*, 163-171.

77. Radmacher, M.; Tilmann, R. W.; Gaub, H. E., Imaging viscoelasticity by force modulation with the atomic force microscope. *Biophys. J.* **1993,** *64*, 735-742.

78. Overney, R. M.; Takano, H.; Fujihira, M., Elastic compliances measured by atomic-force microscopy. *Europhys. Lett.* **1994,** *26*, 443-447.

79. Akari, S. O.; Vandervegte, E. W.; Grim, P. C. M.; Belder, G. F.; Koutsos, V.; Tenbrinke, G.; Hadziioannou, G., Imaging of signle polymer-chains based on their elasticity. *Appl. Phys. Lett.* **1994,** *65*, 1915-1917.

80. Kajiyama, T.; Tanaka, K.; Ohki, I.; Ge, S. R.; Yoon, J. S.; Takahara, A., Imaging of dynamic viscoelastic properties of a phase-separated polymer surface by forced oscillation atomic-force microscopy. *Macromolecules* **1994,** *27*, 7932-7934.

81. Wang, M.; Miyake, S.; Matsunuma, S., Nanowear studies of PFPE lubricant on magnetic perpendicular recording DLC-film-coated disk by lateral oscillation test. *Wear* **2005,** *259*, 1332-1342.

82. Yang, C.; Chen, Y.; Wang, T.; Huang, W., A comparative experimental study on sample excitation and probe excitation in force modulation atomic force microscopy. *Meas. Sci. Technol.* **2013,** *24*, 025403/1-025403/6.

83. Li, F. B.; Thompson, G. E.; Newman, R. C., Force modulation atomic force microscopy: background, development and application to electrodeposited cerium oxide films. *Appl. Surf. Sci.* **1998,** *126*, 21-33.

84. Beake, B. D.; Leggett, G. J.; Shipway, P. H., Frictional, adhesive and mechanical properties of polyester films probed by scanning force microscopy. *Surf. Interface Anal.* **1999,** *27*, 1084-1091.

85. Yamamoto, S.; Yamada, H., Interpretation of direct and indirect force modulation methods using polymer films. *Langmuir* **1997,** *13*, 4861-4864.

86. Lin, C.-C.; Chang, K.-H.; Lin, K.-C.; Su, W.-F., In situ probe nanophase transition in nanocomposite using thermal AFM. *Compos. Sci. Technol.* **2009,** *69*, 1180-1186.

87. Pietrement, O.; Troyon, M., Quantitative study of shear modulus and interfacial shear strength by combining modulated lateral force and magnetic force modulation microscopies. *Surf. Interface Anal.* **2001,** *31*, 1060-1067.

88. Xu, X.; Koslowski, M.; Raman, A., Dynamics of surface-coupled microcantilevers in force modulation atomic force microscopy - magnetic vs. dither piezo excitation. *J. Appl. Phys.* **2012,** *111*, 054303/1-054303/5.

89. Jourdan, J. S.; Cruchon-Dupeyrat, S. J.; Huan, Y.; Kuo, P. K.; Liu, G. Y., Imaging nanoscopic elasticity of thin film materials by atomic force microscopy: Effects of force modulation frequency and amplitude. *Langmuir* **1999,** *15*, 6495-6504.

90. Popa, A. M.; Angeloni, S.; Buergi, T.; Hubbell, J. A.; Heinzelmann, H.; Pugin, R., Dynamic perspective on the function of thermoresponsive nanopores from in situ AFM and ATIZ-IR investigations. *Langmuir* **2010,** *26*, 15356-15365.

91. Schonherr, H.; Frank, C. W., Ultrathin films of poly(ethylene oxides) on oxidized silicon. 2. In situ study of crystallization and melting by hot stage AFM. *Macromolecules* **2003,** *36*, 1199-1208.

92. Hobbs, J. K., In-situ AFM of polymer crystallization. *Chin. J. Polym. Sci.* **2003,** *21*, 135-140.

93. Hu, Z. J.; Du, B. Y.; Zhang, F. J.; Xie, F. C.; He, T. B., In situ study of nanostructure and morphological development during the crystal-mesophase transition of poly(di-n-hexylsilane) and poly(di-n-butylsilane) by X-ray and hot-stage AFM. *Polymer* **2002,** *43*, 6005-6012.

94. Wiedemair, J.; Serpe, M. J.; Kim, J.; Masson, J.-F.; Lyon, L. A.; Mizaikoff, B.; Kranz, C., In-situ AFM studies of the phase-transition behavior of single thermoresponsive hydrogel particles. *Langmuir* **2007,** *23*, 130-137.

95. Mart, R. J.; Osborne, R. D.; Stevens, M. M.; Ulijn, R. V., Peptide-based stimuli-responsive biomaterials. *Soft Matter* **2006,** *2*, 822-835.

96. Wang, J.; Gibson, M. I.; Barbey, R.; Xiao, S.-J.; Klok, H.-A., Nonfouling polypeptide brushes via surface-initiated polymerization of Nε-oligo(ethylene glycol)succinate-L-lysine N-carboxyanhydride. *Macromol. Rapid Commun.* **2009,** *30*, 845-850.

97. Statz, A. R.; Barron, A. E.; Messersmith, P. B., Protein, cell and bacterial fouling resistance of polypeptoid-modified surfaces: effect of side-chain chemistry. *Soft Matter* **2008,** *4*, 131-139.

98. Lunn, J. D.; Shantz, D. F., Peptide brush-ordered mesoporous silica nanocomposite materials. *Chem. Mater.* **2009,** *21*, 3638-3648.

99. Zhang, D.; Lahasky, S. H.; Guo, L.; Lee, C.-U.; Lavan, M., Polypeptoid materials: Current status and future perspectives. *Macromolecules* **2012**, *45*, 5833-5841.

100. Guo, L.; Zhang, D., Cyclic poly(α-peptoid)s and their block copolymers from N-heterocyclic carbene-mediated ring-opening polymerizations of N-substituted N-carboxylanhydrides. *J. Am. Chem. Soc.* **2009,** *131*, 18072-18074.

101. Schneider, M.; Fetsch, C.; Amin, I.; Jordan, R.; Luxenhofer, R., Polypeptoid brushes by surface-initiated polymerization of N-substituted glycine N-carboxyanhydrides. *Langmuir* **2013,** *29*, 6983-6988.

102. Britland, S.; Perezarnaud, E.; Clark, P.; McGinn, B.; Connolly, P.; Moores, G., Micropatterning proteins and synthetic peptides on solid supports - a novel application for microelectronics fabrication technology. *Biotechnol. Progress* **1992,** *8*, 155-160.

103. Hadjichristidis, N.; Iatrou, H.; Pitsikalis, M.; Sakellariou, G., Synthesis of well-defined polypeptide-based materials via the ring-opening polymerization of alpha-amino acid N-carboxyanhydrides. *Chem. Rev.* **2009,** *109*, 5528-5578.

104. Kratzmuller, T.; Appelhans, D.; Braun, H. G., Ultrathin microstructured polypeptide layers by surface-initiated polymerization on microprinted surfaces. *Adv. Mater.* **1999,** *11*, 555-558.

105. Wang, Y. L.; Chang, Y. C., Patterning of polypeptide thin films by the combination of surface-initiated vapor-deposition polymerization and photolithography. *Adv. Mater.* **2003,** *15*, 290-293.

106. Edmondson, S.; Osborne, V. L.; Huck, W. T. S., Polymer brushes via surface-initiated polymerizations. *Chem. Soc. Rev.* **2004,** *33*, 14-22.

107. Sparks, B. J.; Ray, J. G.; Savin, D. A.; Stafford, C. M.; Patton, D. L., Synthesis of thiol-clickable and block copolypeptide brushes via nickel-mediated surface initiated polymerization of [small alpha]-amino acid N-carboxyanhydrides (NCAs). *Chem. Commun.* **2011,** *47*, 6245-6247.

108. Whitesell, J. K.; Chang, H. K., Directionally aligned helical peptides on surfaces. *Science* **1993,** *261*, 73-76.

109. Chang, Y. C.; Frank, C. W., Grafting of poly(gamma-benzyl-L-glutamate) on chemically modified silicon oxide surfaces. *Langmuir* **1996,** *12*, 5824-5829.

110. Chang, Y.-C.; Frank, C. W., Vapor deposition−polymerization of α-amino acid n-carboxy anhydride on the silicon(100) native oxide surface. *Langmuir* **1998,** *14*, 326-334.

111. Heise, A.; Menzel, H.; Yim, H.; Foster, M. D.; Wieringa, R. H.; Schouten, A. J.; Erb, V.; Stamm, M., Grafting of polypeptides on solid substrates by initiation of N-carboxyanhydride polymerization by amino-terminated self-assembled monolayers. *Langmuir* **1997,** *13*, 723-728.

112. Higuchi, M.; Ushiba, K.; Kawaguchi, M., Structural control of peptide-coated gold nanoparticle assemblies by the conformational transition of surface peptides. *J. Colloid Interface Sci.* **2007,** *308*, 356-363.

113. Higuchi, M.; Koga, T.; Taguchi, K.; Kinoshita, T., Fabrication of vertically and unidirectionally oriented polypeptide assemblies on self-assembled monolayers by stepwise polymerization. *Chem. Commun.* **2002**, 1126-1127.

114. Luijten, J.; Vorenkamp, E. J.; Schouten, A. J., Reversible helix sense inversion in surface-grafted poly(beta-phenethyl-L-aspartate) films. *Langmuir* **2007,** *23*, 10772-10778.

115. Wang, Y. L.; Chang, Y. C., Grafting of homo- and block co-polypeptides on solid substrates by an improved surface-initiated vapor deposition polymerization. *Langmuir* **2002,** *18*, 9859-9866.

116. Zheng, W.; Frank, C. W., Surface-initiated vapor deposition polymerization of poly(γ-benzyl-l-glutamate): Optimization and mechanistic studies. *Langmuir* **2009,** *26*, 3929-3941.

117. Wieringa, R. H.; Siesling, E. A.; Geurts, P. F. M.; Werkman, P. J.; Vorenkamp, E. J.; Erb, V.; Stamm, M.; Schouten, A. J., Surface grafting of poly (L-glutamates). 1. Synthesis and characterization. *Langmuir* **2001,** *17*, 6477-6484.

118. Wieringa, R. H.; Siesling, E. A.; Werkman, P. J.; Angerman, H. J.; Vorenkamp, E. J.; Schouten, A. J., Surface grafting of poly(L-glutamates). 2. Helix orientation. *Langmuir* **2001,** *17*, 6485-6490.

119. Wieringa, R. H.; Siesling, E. A.; Werkman, P. J.; Vorenkamp, E. J.; Schouten, A. J., Surface grafting of poly(L-glutamates). 3. Block copolymerization. *Langmuir* **2001,** *17*, 6491-6495.

120. Wu, J.-C.; Wang, Y.; Chen, C.-C.; Chang, Y.-C., Biomimetic synthesis of silica films directed by polypeptide brushes. *Chem. Mater.* **2008,** *20*, 6148-6156.

121. Wang, Y. L.; Chang, Y. C., Synthesis and conformational transition of surface-tethered polypeptide: Poly(L-lysine). *Macromolecules* **2003,** *36*, 6511-6518.

122. Wang, Y. L.; Chang, Y. C., Synthesis and conformational transition of surface-tethered polypeptide: Poly(L-glutamic acid). *Macromolecules* **2003,** *36*, 6503-6510.

123. Deming, T. J., Transition metal-amine initiators for preparation of well-defined poly(gamma-benzyl L-glutamate). *J. Am. Chem. Soc.* **1997,** *119*, 2759-2760.

124. Deming, T. J.; Curtin, S. A., Chain initiation efficiency in cobalt- and nickel-mediated polypeptide synthesis. *J. Am. Chem. Soc.* **2000,** *122*, 5710-5717.

125. Brzezinska, K. R.; Deming, T. J., Synthesis of ABA triblock copolymers via acyclic diene metathesis polymerization and living polymerization of alpha-amino acid-N-carboxyanhydrides. *Macromolecules* **2001,** *34*, 4348-4354.

126. Witte, P.; Menzel, H., Nickel-mediated surface grafting from polymerization of α-Amino acid-N-carboxyanhydrides. *Macromol. Chem. Phys.* **2004,** *205*, 1735-1743.

127. Zhang, J.; Li, Y.; Zhang, X.; Yang, B., Colloidal self-assembly meets nanofabrication: From two-dimensional colloidal crystals to nanostructure arrays. *Adv. Mater.* **2010,** *22*, 4249-4269.

128. Chen, T.; Amin, I.; Jordan, R., Patterned polymer brushes. *Chem. Soc. Rev.* **2012,** *41*, 3280-3296.

129. Penner, R. M., Rapid, wafer-scale laser nanoprinting of polymer surfaces. *ACS Nano* **2011,** *5*, 690-692.

130. Valsesia, A.; Lisboa, P.; Colpo, P.; Rossi, F., Fabrication of polypyrrole-based nanoelectrode arrays by colloidal lithography. *Anal. Chem.* **2006,** *78*, 7588-7591.

131. Agheli, H.; Sutherland, D. S., Nanofabrication of polymer surfaces utilizing colloidal lithography and ion etching. *Ieee Trans. Nanobiosci.* **2006,** *5*, 9-14.

132. Lu, Y.; Chen, S. C., Micro and nano-fabrication of biodegradable polymers for drug delivery. *Adv. Drug Delivery Rev.* **2004,** *56*, 1621-1633.

133. Schepelina, O.; Zharov, I., PNIPAAM-modified nanoporous colloidal films with positive and negative temperature gating. *Langmuir* **2007,** *23*, 12704-12709.

134. Acikgoz, C.; Ling, X. Y.; Phang, I. Y.; Hempenius, M. A.; Reinhoudt, D. N.; Huskens, J.; Vancso, G. J., Fabrication of freestanding nanoporous polyethersulfone membranes using organometallic polymer resists patterned by nanosphere lithography. *Adv. Mater.* **2009,** *21*, 2064-2067.

135. Ling, X. Y.; Acikgoz, C.; Phang, I. Y.; Hempenius, M. A.; Reinhoudt, D. N.; Vancso, G. J.; Huskens, J., 3D ordered nanostructures fabricated by nanosphere lithography using an organometallic etch mask *Nanoscale* **2010,** *2*, 1455-1460.

136. Santos, L.; Martin, P.; Ghilane, J.; Lacaze, P.-C.; Randriamahazaka, H.; Abrantes, L. M.; Lacroix, J.-C., Electrosynthesis of well-organized nanoporous poly(3,4-ethylenedioxythiophene) by nanosphere lithography. *Electrochem. Commun.* **2010,** *12*, 872-875.

137. Hsiao, Y. S.; Chien, F. C.; Huang, J. H.; Chen, C. P.; Kuo, C. W.; Chu, C. W.; Chen, P. L., Facile transfer method for fabricating light-harvesting systems for polymer solar cells. *J. Phys. Chem. C* **2011,** *115*, 11864-11870.

138. Beryozkina, T.; Boyko, K.; Khanduyeva, N.; Senkovskyy, V.; Horecha, M.; Oertel, U.; Simon, F.; Stamm, M.; Kiriy, A., Grafting of polyfluorene by surface-initiated suzuki polycondensation. *Angew. Chem., Int. Ed.* **2009,** *48*, 2695-2698.

139. Chen, T.; Chang, D. P.; Jordan, R.; Zauscher, S., Colloidal lithography for fabricating patterned polymer-brush microstructures. *Beilstein J. Nanotechnol.* **2012,** *3*, 397-403.

140. Chen, T.; Jordan, R.; Zauscher, S., Polymer brush patterning using self-assembled microsphere monolayers as microcontact printing stamps. *Soft Matter* **2011,** *7*, 5532-5535.

141. Bognar, J.; Szucs, J.; Dorko, Z.; Horvath, V.; Gyurcsanyi, R. E., Nanosphere lithography as a versatile method to generate surface-imprinted polymer films for selective protein recognition. *Adv. Funct. Mater.* **2013,** *23*, 4703-4709.

142. Pernites, R. B.; Foster, E. L.; Felipe, M. J. L.; Robinson, M.; Advincula, R. C., Patterned surfaces combining polymer brushes and conducting polymer via colloidal template electropolymerization. *Adv. Mater.* **2011,** *23*, 1287-1292.

143. Saner, C. K.; Lusker, K. L.; LeJeune, Z. M.; Serem, W. K.; Garno, J. C., Self-assembly of octadecyltrichlorosilane: Surface structures formed using different protocols of particle lithography. *Beilstein J. Nanotechnol.* **2012,** *3*, 114-122.

144. Li, J.-R.; Garno, J. C., Elucidating the role of surface hydrolysis in preparing organosilane nanostructures via particle lithography. *Nano Letters* **2008,** *8*, 1916-1922.

145. Robinson, J. W.; Schlaad, H., A versatile polypeptoid platform based on N-allyl glycine. *Chem. Commun.* **2012,** *48*, 7835-7837.

146. Jones, D. M.; Smith, J. R.; Huck, W. T. S.; Alexander, C., Variable adhesion of micropatterned thermoresponsive polymer brushes: AFM investigations of poly (N-

isopropylacrylamide) brushes prepared by surface-initiated polymerizations. *Adv. Mater.* **2002,** *14*, 1130-1134.

147. Kelley, T. W.; Schorr, P. A.; Johnson, K. D.; Tirrell, M.; Frisbie, C. D., Direct force measurements at polymer brush surfaces by atomic force microscopy. *Macromolecules* **1998,** *31*, 4297-4300.

148. Kitano, K.; Inoue, Y.; Matsuno, R.; Takai, M.; Ishihara, K., Nanoscale evaluation of lubricity on well-defined polymer brush surfaces using QCM-D and AFM. *Colloids Surf. B* **2009,** *74*, 350-357.

149. Lemieux, M.; Usov, D.; Minko, S.; Stamm, M.; Shulha, H.; Tsukruk, V. V., Reorganization of binary polymer brushes: Reversible switching of surface microstructures and nanomechanical properties. *Macromolecules* **2003,** *36*, 7244-7255.

150. Yamamoto, S.; Ejaz, M.; Tsujii, Y.; Matsumoto, M.; Fukuda, T., Surface interaction forces of well-defined, high-density polymer brushes studied by atomic force microscopy. 1. Effect of chain length. *Macromolecules* **2000,** *33*, 5602-5607.

151. Advincula, R.; Zhou, Q. G.; Park, M.; Wang, S. G.; Mays, J.; Sakellariou, G.; Pispas, S.; Hadjichristidis, N., Polymer brushes by living anionic surface initiated polymerization on flat silicon (SiO(x)) and gold surfaces: Homopolymers and block copolymers. *Langmuir* **2002,** *18*, 8672-8684.

152. Kolb, H. C.; Finn, M. G.; Sharpless, K. B., Click chemistry: Diverse chemical function from a few good reactions. *Angew Chem., Int. Ed.* **2001,** *40*, 2004-2021.

153. Hensarling, R. M.; Doughty, V. A.; Chan, J. W.; Patton, D. L., "Clicking" polymer brushes with thiol-yne chemistry: Indoors and out. *J. Am. Chem. Soc.* **2009,** *131*, 14673-14675.

154. Engler, A. C.; Lee, H.-i.; Hammond, P. T., Highly efficient "grafting onto" a polypeptide backbone using click chemistry. *Angew Chem., Int. Ed.* **2009,** *48*, 9334-9338.

155. Nečas, D.; Klapetek, P., Gwyddion: an open-source software for SPM data analysis. *Central European Journal of Physics* **2012,** *10*, 181-188.

156. Belgardt, C.; Sowade, E.; Blaudeck, T.; Baumgartel, T.; Graaf, H.; von Borczyskowski, C.; Baumann, R. R., Inkjet printing as a tool for the patterned deposition of octadecylsiloxane monolayers on silicon oxide surfaces. *Physical Chemistry Chemical Physics* **2013**, *15*, 7494-7504.

157. Fadeev, A. Y.; McCarthy, T. J., Self-assembly is not the only reaction possible between alkyltrichlorosilanes and surfaces: Monomolecular and oligomeric covalently attached layers of dichloro- and trichloroalkylsilanes on silicon. *Langmuir* **2000,** *16*, 7268-7274.

158. Ulman, A., Self-assembled monolayers of alkyltrichiorosilanes: Building blocks for future organic materials. *Adv. Mater.* **1990,** *2*, 573-582.

159. Chen, T.; Ferris, R.; Zhang, J.; Ducker, R.; Zauscher, S., Stimulus-responsive polymer brushes on surfaces: Transduction mechanisms and applications. *Prog. Polym. Sci.* **2010,** *35*, 94-112.

160. Ma, D.; Chen, H.; Shi, D.; Li, Z.; Wang, J., Preparation and characterization of thermo-responsive PDMS surfaces grafted with poly(N-isopropylacrylamide) by benzophenone-initiated photopolymerization. *J. Colloid Interface Sci.* **2009,** *332*, 85-90.

161. Guo, H.; Ulbricht, M., Preparation of thermo-responsive polypropylene membranes via surface entrapment of poly(N-isopropylacrylamide)-containing macromolecules. *J. Membr. Sci.* **2011,** *372*, 331-339.

162. Nagase, K.; Akimoto, A. M.; Kobayashi, J.; Kikuchi, A.; Akiyama, Y.; Kanazawa, H.; Okano, T., Effect of reaction solvent on the preparation of thermo-responsive stationary phase through a surface initiated atom transfer radical polymerization. *J. Chromatogr. A* **2011,** *1218*, 8617-8628.

163. Ayano, E.; Okada, Y.; Sakamoto, C.; Kanazawa, H.; Kikuchi, A.; Okano, T., Study of temperature-responsibility on the surfaces of a thermo-responsive polymer modified stationary phase. *J. Chromatogr. A* **2006,** *1119*, 51-57.

164. Hirose, M.; Yamato, M.; Kwon, O. H.; Harimoto, M.; Kushida, A.; Shimizu, T.; Kikuchi, A.; Okano, T., Temperature-responsive surface for novel co-culture systems of hepatocytes with endothelial cells: 2-D patterned and double layered co-cultures. *Yonsei Med. J.* **2000,** *41*, 803-813.

165. Bullett, N. A.; Talib, R. A.; Short, R. D.; McArthur, S. L.; Shard, A. G., Chemical and thermo-responsive characterisation of surfaces formed by plasma polymerisation of N-isopropyl acrylamide. *Surf. Interface Anal.* **2006,** *38*, 1109-1116.

166. Hu, Z. B.; Chen, Y. Y.; Wang, C. J.; Zheng, Y. D.; Li, Y., Polymer gels with engineered environmentally responsive surface patterns. *Nature* **1998,** *393*, 149-152.

167. Yamato, M.; Konno, C.; Utsumi, M.; Kikuchi, A.; Okano, T., Thermally responsive polymer-grafted surfaces facilitate patterned cell seeding and co-culture. *Biomaterials* **2002,** *23*, 561-567.

168. Pan, K.; Zhang, X.; Cao, B., Surface-initiated atom transfer radical polymerization of regenerated cellulose membranes with thermo-responsive properties. *Polym. Int.* **2010,** *59*, 733-737.

169. Park, J. K.; Kim, K. S.; Yeom, J.; Jung, H. S.; Hahn, S. K., Facile surface modification and application of temperature responsive poly(N-isopropylacrylamide-co-dopamine methacrylamide). *Macromol. Chem. Phys.* **2012,** *213*, 2130-2135.

170. Li, J.; He, W.-D.; Sun, X.-L., Preparation of poly(styrene-b-N-isopropylacrylamide) micelles surface-linked with gold nanoparticles and thermo-responsive ultraviolet-visible absorbance. *J. Polym. Sci., Part A: Polym. Chem.* **2007,** *45*, 5156-5163.

171. Park, H. H.; Lee, T. R., Thermo- and pH-responsive hydrogel-coated gold nanoparticles prepared from rationally designed surface-confined initiators. *J. Nanopart. Res.* **2011,** *13*, 2909-2918.

172. Wu, D.; Liu, X.; Yu, S.; Liu, M.; Gao, C., Modification of aromatic polyamide thin-film composite reverse osmosis membranes by surface coating of thermo-responsive copolymers P(NIPAM-co-Am). I: Preparation and characterization. *J. Membr. Sci.* **2010,** *352*, 76-85.

173. Mizutani, A.; Nagase, K.; Kikuchi, A.; Kanazawa, H.; Akiyama, Y.; Kobayashi, J.; Annaka, M.; Okano, T., Preparation of thermo-responsive polymer brushes on hydrophilic polymeric beads by surface-initiated atom transfer radical polymerization for a highly resolutive separation of peptides. *J. Chromatogr. A* **2010,** *1217*, 5978-5985.

174. de Las Heras Alarcon, C.; Twaites, B.; Cunliffe, D.; Smith, J. R.; Alexander, C., Grafted thermo- and pH responsive co-polymers: surface-properties and bacterial adsorption. *Int. J. Pharm.* **2005,** *295*, 77-91.

175. Laloyaux, X.; Mathy, B.; Nysten, B.; Jonas, A. M., Surface and bulk collapse transitions of thermo responsive polymer brushes. *Langmuir* **2010,** *26*, 838-847.

176. Park, S.; Zhong, M.; Lee, T.; Paik, H.-J.; Matyjaszewski, K., Modification of the surfaces of silicon wafers with temperature-responsive cross-linkable poly oligo(ethylene oxide) methacrylate -based star polymers. *ACS Appl. Mater. Interfaces* **2012,** *4*, 5949-5955.

177. Medel, S.; Manuel Garcia, J.; Garrido, L.; Quijada-Garrido, I.; Paris, R., Thermo- and pH-responsive gradient and block copolymers based on 2-(2-methoxyethoxy)ethyl methacrylate synthesized via atom transfer radical polymerization and the formation of thermoresponsive surfaces. *J. Polym. Sci., Part A: Polym. Chem.* **2011,** *49*, 690-700.

178. Wischerhoff, E.; Zacher, T.; Laschewsky, A.; Rekai, E., Direct observation of the lower critical solution temperature of surface-attached thermo-responsive hydrogels by surface plasmon resonance. *Angew. Chem., Int. Ed.* **2000,** *39*, 4602-4604.

179. Sousa, M. E.; Broer, D. J.; Bastiaansen, C. W. M.; Freund, L. B.; Crawford, G. P., Isotropic "islands" in a cholesteric "sea": Patterned thermal expansion for responsive surface topologies". *Adv. Mater.* **2006,** *18*, 1842-1845.

180. Bulychev, N.; Confortini, O.; Kopold, P.; Dirnberger, K.; Schauer, T.; Du Prez, F. E.; Zubov, V.; Eisenbach, C. D., Application of thermo-responsive poly(methyl vinyl ether) containing copolymers in combination with ultrasonic treatment for pigment surface modification in pigment dispersions. *Polymer* **2007,** *48*, 2636-2643.

181. Dey, S.; Kellam, B.; Alexander, M. R.; Alexander, C.; Rose, F. R. A. J., Enzyme-passage free culture of mouse embryonic stem cells on thermo-responsive polymer surfaces. *J. Mater. Chem.* **2011,** *21*, 6883-6890.

182. Edmondson, S.; Osborne, V. L.; Huck, W. T. S., Polymer brushes via surface-initiated polymerizations. *Chemical Society Reviews* **2004,** *33*, 14-22.

183. Prakash, S.; Long, T. M.; Selby, J. C.; Moore, J. S.; Shannon, M. A., "Click" modification of silica surfaces and glass microfluidic channels. *Anal. Chem.* **2007,** *79*, 1661-1667.

184. Wu, X.-M.; Wang, L.-L.; Wang, Y.; Gu, J.-S.; Yu, H.-Y., Surface modification of polypropylene macroporous membrane by marrying RAFT polymerization with click chemistry. *J. Membr. Sci.* **2012,** *421*, 60-68.

185. Yameen, B.; Ali, M.; Alvarez, M.; Neumann, R.; Ensinger, W.; Knoll, W.; Azzaroni, O., A facile route for the preparation of azide-terminated polymers. "Clicking" polyelectrolyte brushes on planar surfaces and nanochannels. *Polym. Chem.* **2010,** *1*, 183-192.

186. Chen, G.; Tao, L.; Mantovani, G.; Ladmiral, V.; Burt, D. P.; Macpherson, J. V.; Haddleton, D. M., Synthesis of azide/alkyne-terminal polymers and application for surface functionalisation through a [2 + 3] Huisgen cycloaddition process, "click chemistry". *Soft Matter* **2007,** *3*, 732-739.

187. Proks, V.; Jaros, J.; Pop-Georgievski, O.; Kucka, J.; Popelka, S.; Dvorak, P.; Hampl, A.; Rypacek, F., "Click & seed" approach to the biomimetic modification of material surfaces. *Macromol. Biosci.* **2012,** *12*, 1232-1242.

188. Haensch, C.; Erdmenger, T.; Fijten, M. W. M.; Hoeppener, S.; Schubert, U. S., Fast surface modification by microwave assisted click reactions on silicon substrates. *Langmuir* **2009,** *25*, 8019-8024.

189. Ru, X.; Zeng, X.; Li, Z.; Evans, D. J.; Zhan, C.; Tang, Y.; Wang, L.; Liu, X., Bioinspired polymer functionalized with a diiron carbonyl model complex and its assembly onto the surface of a gold electrode via "click" chemistry. *J. Polym. Sci., Part A: Polym. Chem.* **2010,** *48*, 2410-2417.

190. Drockenmuller, E.; Colinet, I.; Damiron, D.; Gal, F.; Perez, H.; Carrot, G., Efficient approaches for the surface modification of platinum nanoparticles via click chemistry. *Macromolecules* **2010,** *43*, 9371-9375.

191. El Habnouni, S.; Darcos, V.; Garric, X.; Lavigne, J.-P.; Nottelet, B.; Coudane, J., Mild methodology for the versatile chemical modification of polylactide surfaces: Original combination of anionic and click chemistry for biomedical applications. *Adv. Funct. Mater.* **2011,** *21*, 3321-3330.

192. Chen, J.; Xiang, J.; Cai, Z.; Yong, H.; Wang, H.; Zhang, L.; Luo, W.; Min, H., Synthesis of hydrophobic polymer brushes on silica nanoparticles via the combination of surface-initiated ATRP, ROP and click chemistry. *J. Macromol. Sci. A, Pure Appl. Chem.* **2010,** *47*, 655-662.

193. Bayraktar, A.; Saracoglu, B.; Golgelioglu, C.; Tuncel, A., Click-chemistry for surface modification of monodisperse-macroporous particles. *J. Colloid Interface Sci.* **2012,** *365*, 63-71.

194. Chen, J. C.; Wang, Y. P.; Wang, H. D.; Wei, S. Y.; Li, H. J.; Yan, X. D., Preparation of polymer brushes on attapulgite surfaces via a combination of CROP and click reaction. *Chin. Chem. Lett.* **2010,** *21*, 496-500.

195. Zhang, T.; Wu, Y.; Pan, X.; Zheng, Z.; Ding, X.; Peng, Y., An approach for the surface functionalized gold nanoparticles with pH-responsive polymer by combination of RAFT and click chemistry. *Eur. Polym. J.* **2009,** *45*, 1625-1633.

196. Li, L.; Zhao, N.; Liu, S., Versatile surface biofunctionalization of poly(ethylene terephthalate) by interpenetrating polymerization of a butynyl monomer followed by "Click Chemistry". *Polymer* **2012,** *53*, 67-78.

197. White, M. A.; Johnson, J. A.; Koberstein, J. T.; Turro, N. J., Toward the syntheses of universal ligands for metal oxide surfaces: Controlling surface functionality through click chemistry. *J. Am. Chem. Soc.* **2006,** *128*, 11356-11357.

198. Zhang, T.; Zheng, Z.; Ding, X.; Peng, Y., Smart surface of gold nanoparticles fabricated by combination of raft and click chemistry. *Macromol. Rapid Commun.* **2008,** *29*, 1716-1720.

199. Ranjan, R.; Brittain, W. J., Combination of living radical polymerization and click chemistry for surface modification. *Macromolecules* **2007,** *40*, 6217-6223.

200. Ranjan, R.; Brittain, W. J., Tandem raft polymerization and click chemistry: An efficient approach to surface modification. *Macromol. Rapid Commun.* **2007,** *28*, 2084-2089.

201. Li, G. L.; Wan, D.; Neoh, K. G.; Kang, E. T., Binary polymer brushes on silica@polymer hybrid nanospheres and hollow polymer nanospheres by combined alkyne-azide and thiol-ene surface click reactions. *Macromolecules* **2010,** *43*, 10275-10282.

202. Slavin, S.; Haddleton, D. M., An investigation into thiol-ene surface chemistry of poly(ethylene glycol) acrylates, methacrylates and CCTP polymers via quartz crystal microbalance with dissipation monitoring (QCM-D). *Soft Matter* **2012,** *8*, 10388-10393.

203. Khire, V. S.; Lee, T. Y.; Bowman, C. N., Synthesis, characterization and cleavage of surface-bound linear polymers formed using thiol-ene photopolymerizations. *Macromolecules* **2008,** *41*, 7440-7447.

204. Goldmann, A. S.; Walther, A.; Nebhani, L.; Joso, R.; Ernst, D.; Loos, K.; Barner-Kowollik, C.; Barner, L.; Mueller, A. H. E., Surface modification of poly(divinylbenzene) microspheres via thiol-ene chemistry and alkyne-azide click reactions. *Macromolecules* **2009,** *42*, 3707-3714.

205. Tedja, R.; Soeriyadi, A. H.; Whittaker, M. R.; Lim, M.; Marquis, C.; Boyer, C.; Davis, T. P.; Amal, R., Effect of TiO2 nanoparticle surface functionalization on protein adsorption, cellular uptake and cytotoxicity: the attachment of PEG comb polymers using catalytic chain transfer and thiol-ene chemistry. *Polym. Chem.* **2012,** *3*, 2743-2751.

206. Saner, C. K.; Lusker, K. L.; LeJeune, Z. M.; Serem, W. K.; Garno, J. C., Self-assembly of octadecyltrichlorosilane: Surface structures formed using different protocols of particle lithography. *Beilstein Journal of Nanotechnology* **2012,** *3*, 114-122.

207. Lahasky, S. H.; Hu, X.; Zhang, D., Thermoresponsive poly(α-peptoid)s: Tuning the cloud point temperatures by composition and architecture. *ACS Macro Lett.* **2012,** *1*, 580-584.

208. Stroup, E. W.; Pungor, A.; Hlady, V., A constant compliance force modulation technique for scanning force microscopy (SFM) imaging of polymer surface elasticity. *Ultramicroscopy* **1996,** *66*, 237-249.

209. Hellgren, A. C., Probing polymer interdiffusion in carboxylated latices with force modulation atomic force microscopy. *Prog. Org. Coat.* **1998,** *34*, 91-99.

210. Yang, N.; Wong, K. K. H.; de Bruyn, J. R.; Hutter, J. L., Frequency-dependent viscoelasticity measurement by atomic force microscopy. *Meas. Sci. Technol.* **2009,** *20*, 025703/1-025703/9.

211. Miyake, S.; Wang, M.; Ninomiya, S., Nanotribological properties of perfluoropolyether-coated magnetic disk evaluated by vertical and lateral vibration wear tests. *Surf. Coat. Tech.* **2006,** *200*, 6137-6154.

212. Mazeran, P.-E.; Loubet, J.-L., Force modulation with a scanning force microscope: an analysis. *Tribol. Lett.* **1997,** *3*, 125-132.

213. Pietrement, O.; Troyon, M., Quantitative elastic modulus measurement by magnetic force modulation microscopy. *Tribol. Lett.* **2000,** *9*, 77-87.

214. Jalili, N.; Laxminarayana, K., A review of atomic force microscopy imaging systems: application to molecular metrology and biological sciences. *Mechatronics* **2004,** *14*, 907-945.

215. Overney, R. M.; Meyer, E.; Frommer, J.; Guntherodt, H. J.; Fujihira, M.; Takano, H.; Gotoh, Y., Force microscopy study of friction and elastic compliance of phase-separated organic thin-films. *Langmuir* **1994,** *10*, 1281-1286.

216. Menke, M.; Kunneke, S.; Janshoff, A., Lateral organization of G(M1) in phase-separated monolayers visualized by scanning force microscopy. *Eur. Biophys. J. Biophys. Lett.* **2002,** *31*, 317-322.

217. Lin, H. N.; Hung, T. T.; Chang, E. C.; Chen, S. A., Force modulation microscopy study of phase separation on blend polymer films. *Appl. Phys. Lett.* **1999,** *74*, 2785-2787.

218. Asif, S. A. S.; Wahl, K. J.; Colton, R. J., Nanoindentation and contact stiffness measurement using force modulation with a capacitive load-displacement transducer. *Rev. Sci Instrum.* **1999,** *70*, 2408-2413.

219. Asif, S. A. S.; Wahl, K. J.; Colton, R. J.; Warren, O. L., Quantitative imaging of nanoscale mechanical properties using hybrid nanoindentation and force modulation. *J. Appl. Phys.* **2001,** *90*, 1192-1200.

220. Overney, R. M.; Bonner, T.; Meyer, E.; Reutschi, M.; Luthi, R.; Howald, L.; Frommer, J.; Guntherodt, H. J.; Fujihara, M.; Takano, H., Elasticity, wear, and friction properties of thin organic films observed with atomic-force microscopy. *J. Vac. Sci. Technol. B* **1994,** *12*, 1973-1976.

221. Bar, G.; Rubin, S.; Parikh, A. N.; Swanson, B. I.; Zawodzinski, T. A.; Whangbo, M. H., Scanning force microscopy study of patterned monolayers of alkanethiols on gold. Importance of tip-sample contact area in interpreting force modulation and friction force microscopy images. *Langmuir* **1997,** *13*, 373-377.

222. Pignataro, B.; Sardone, L.; Marletta, G., Dynamic scanning force microscopy investigation of nanostructured spiral-like domains in Langmuir-Blodgett monolayers. *Nanotechnology* **2003,** *14*, 245-249.

223. Price, W. J.; Leigh, S. A.; Hsu, S. M.; Patten, T. E.; Liu, G. Y., Measuring the size dependence of Young's modulus using force modulation atomic force microscopy. *J. Phys. Chem. A* **2006,** *110*, 1382-1388.

224. Zhang, J.; Parlak, Z.; Bowers, C. M.; Oas, T.; Zauscher, S., Mapping mechanical properties of organic thin films by force-modulation microscopy in aqueous media. *Beilstein J. Nanotech.* **2012,** *3*, 464-474.

225. Kiridena, W.; Jain, V.; Kuo, P. K.; Liu, G. Y., Nanometer-scale elasticity measurements on organic monolayers using scanning force microscopy. *Surf. Interface Anal.* **1997,** *25*, 383-389.

226. Price, W. J.; Kuo, P. K.; Lee, T. R.; Colorado, R.; Ying, Z. C.; Liu, G. Y., Probing the local structure and mechanical response of nanostructures using force modulation and nanofabrication. *Langmuir* **2005,** *21*, 8422-8428.

227. Ling, J. S. G.; Leggett, G. J., Scanning force microscopy of poly(ethylene terephthalate) surfaces: Comparison of SEM with SFM topographical, lateral force and force modulation data. *Polymer* **1997,** *38*, 2617-2625.

228. Overney René, M.; Tsukruk Vladimir, V., Scanning probe microscopy in polymers: introductory notes. In *Scanning Probe Microscopy of Polymers*, American Chemical Society: ACS Symposium Series, 1998; Vol. 694, pp 2-30.

229. Florin, E. L.; Radmacher, M.; Fleck, B.; Gaub, H. E., Atomic-force microscope with magnetic force modulation. *Rev. Sci. Instrum.* **1994,** *65*, 639-643.

230. Friedenberg, M. C.; Mate, C. M., Dynamic viscoelastic properties of liquid polymer films studied by atomic force microscopy. *Langmuir* **1996,** *12*, 6138-6142.

231. Krotil, H. U.; Stifter, T.; Marti, O., Concurrent measurement of adhesive and elastic surface properties with a new modulation technique for scanning force microscopy. *Rev. Sci. Instrum.* **2000,** *71*, 2765-2771.

232. Lee, C.-U.; Lu, L.; Chen, J.; Garno, J. C.; Zhang, D., Crystallization-driven thermoreversible gelation of coil-crystalline cyclic and linear diblock copolypeptoids. *ACS Macro Lett.* **2013,** *2*, 436-440.

233. Kimura, K.; Kobayashi, K.; Yamada, H.; Matsushige, K., High resolution molecular chain imaging of a poly(vinylidenefluoride-trifluoroethylene) crystal using force modulation microscopy. *Nanotechnology* **2007,** *18*, 305504/1-305504/6.

234. Deleu, M.; Nott, K.; Brasseur, R.; Jacques, P.; Thonart, P.; Dufrene, Y. F., Imaging mixed lipid monolayers by dynamic atomic force microscopy. *BBA-Biomembranes* **2001,** *1513*, 55-62.

235. Baselt, D. R.; Clark, S. M.; Youngquist, M. G.; Spence, C. F.; Baldeschwieler, J. D., Digital signal processor control of scanned probe microscopes. *Rev. Sci. Instrum.* **1993,** *64*, 1874-1882.

236. Kasas, S.; Thomson, N. H.; Smith, B. L.; Hansma, P. K.; Miklossy, J.; Hansma, H. G., Biological applications of the AFM: From single molecules to organs. *Int. J. Imaging Syst. Technol.* **1997,** *8*, 151-161.

237. Neumann, R.; Ackermann, J.; Angert, N.; Trautmann, C.; Dischner, M.; Hagen, T.; Sedlacek, M., Ion tracks in mica studied with scanning force microscopy using force modulation. *Nucl. Instrum. Methods Phys. Res. Sect. B* **1996,** *116*, 492-495.

238. Greene, M. E.; Kinser, C. R.; Kramer, D. E.; Pingree, L. S. C.; Hersam, M. C., Application of scanning probe microscopy to the characterization and fabrication of hybrid nanomaterials. *Microsc. Res. Tech.* **2004,** *64*, 415-434.

239. Schiavon, G.; Kuchler, J. G.; Corain, B.; Hiller, W., Force modulation atomic force microscopy as a powerful tool in organic-inorganic hybrid materials analysis. *Adv. Mater.* **2001,** *13*, 310-313.

240. Kimura, K.; Kobayashi, K.; Yamada, H.; Matsushige, K., Submolecular resolution viscoelastic imaging of a poly(p-toluene-sulfonate) single crystal using force modulation microscopy. *Nanotechnology* **2008,** *19*, 065701/1-065701/5.

241. Nečas, D.; Klapetek, P., Gwyddion: an open-source software for SPM data analysis. *Cent. Eur. J. Phys.* **2012,** *10*, 181-188.

242. Li, J.-R.; Lusker, K. L.; Yu, J.-J.; Garno, J. C., Engineering the spatial selectivity of surfaces at the nanoscale using particle lithography combined with vapor deposition of organosilanes. *ACS Nano* **2009,** *3*, 2023-2035.

243. Saner, C. K.; Lusker, K. L.; LeJeune, Z. M.; Serem, W. K.; Garno, J. C., Self-assembly of octadecyltrichlorosilane: Surface structures formed using different protocols of particle lithography. *Beilstein J. Nanotech.* **2012,** *3*, 114-122.

APPENDIX A: PROCEDURE FOR FORCE MODULATION MICROSCOPY (FMM) USING NEWLY-DESIGNED SAMPLE STAGE

Hardware set-up

For FMM operation, connect cables as shown in Figure A1. Connect a BNC cable to the **AUX** of the head electronic box to the **PHASE** input of MAC/AC controller. Connect a second BNC cable from the **AMPLITUDE** output of MAC/AC controller to the **AUX IN** of the PicoSPM II controller. Connect a third BNC cable from the **AAC** output to the BNC cable of the force modulation sample stage.

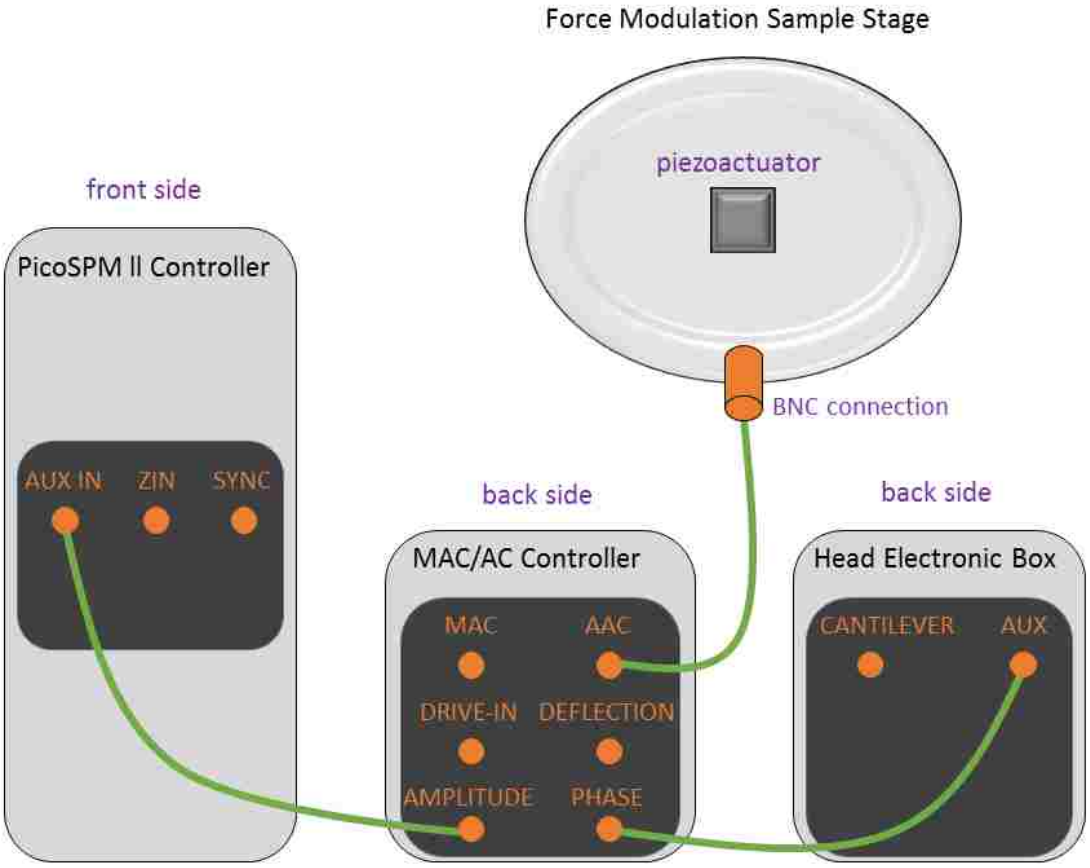

Figure A1 Cable connections for FMM imaging

1. Use the plain nosecone (contact-mode nosecone) with the Keysight 5500 AFM multipurpose scanner for FMM imaging.

2. Connect three cables between the PicoSPM II controller, MAC/AC controller, head electronic box, and the FMM sample stage as shown in Figure A1.
3. Use silicon nitride cantilevers (MSCT, Bruker Probes) with force constants of 0.01-0.6 N/m for FMM imaging.
4. Put a magnet at the center of the FMM sample stage, then use double sided tape to glue the sample on the magnet. Do not directly glue the sample on the sample stage.
5. Install the FMM sample stage and the scanner for FMM operation. Adjust the position of laser and photodiode signal so that **Deflection** at -1 and **LFM** at 0 on the head electronic box.

Software set-up

1. Launch the Picoview v1.12 software. Under **main menu**, select contact mode parameters for Keysight 5500 AFM multipurpose scanner.
2. Create six channels on the second monitor including trace and retrace of topography, Aux BNC (amplitude) and HEB Aux (phase) on the top/bottom row. Choose channels on the top row to represent trace data and those on the bottom row to display retrace data.
3. Open the AFM AC Mode Tune window and set up the frequency range between 0 to 600 kHz.
4. Enter 0 for the **Force Setpoint** and then start to approach.
5. Under Control menu, select “advanced”, choose “AC mode”, Select AAC option in the drive control window. Enable the **Drive On** and start the drive on percentage at 5%.

Frequency sweep

1. After the tip engages the surface, click on the **Manual Tune** button in the **AC Tune** window to acquire a frequency spectrum with the vibration of the force modulation sample stage.
2. Adjust the **Drive On %** until significant, detectable peaks are observed for the frequency sweep (peak amplitude around 1 V). Save the frequency sweep as a *.txt file.
3. Choose the resonance frequencies in the frequency sweep by moving the red dash line on top of the resonance peak maximum.

FMM imaging

1. Start to acquire FMM images and adjust the **Integral (I) Gain**, the **Proportional (P) Gain,** the **driving frequency** and the **Force Setpoint** to tune the images.
2. During experiments, compare images and spectra with and without the field activated. Turn the field on and off by enabling or disenabling the **Drive On**.
3. Try different resonance frequencies in the sweep and compare the FMM results.

APPENDIX B: PROCEDURE FOR TEMPERATURE STUDIES USING THE HEATING STAGE WITH KEYSIGHT 5500 OR 5420

For AFM temperature studies, connect the cables from **HEATER OUT** and **INPUT A** of the back side of the heating stage controller to the heating sample stage as shown in Figure B1. Plug in the power cord. Then put the sample on the heating stage and insert to either Keysight 5500 or 5420. Caution: when using double-sided tape to glue the samples make sure the tape will not melt or influence the study at the temperature range you plan to use. If operating the temperature study in liquid medium, check the boiling point of the solvent and the temperature range you plan to use.

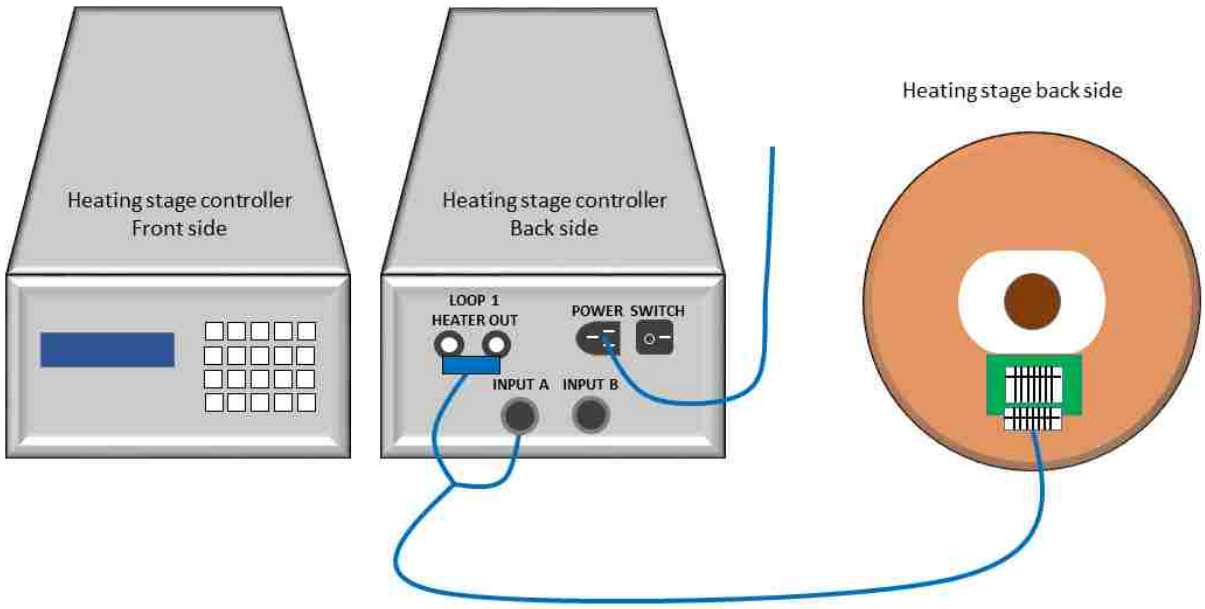

Figure B1 Cable connections for the operation of the heating stage

After cable connections, choose the right settings in the front side of the heating stage controller:

1. Click **set point** and choose the temperature you want to heat the sample to.
2. Click **heater range** and choose between **high**, **low** or **off**. This determines how fast the heating speed is. When choosing "off", the heater will be turned off.

3. Click **Input setup**, choose **input A**, **type 100 Ω Plat/500**, **curve 06 PT-100**, **Filter on**, **Filter points 08** and **filter window 01%**.
4. Click **Display format**, there are four locations we can set displays (two on the top and two at bottom). At **location 1**, choose **Display input A** and **Source Temp C**; at **location 2**, choose **Display input B** and **Source Temp C**; at **location 3**, choose **Display setpoint**; at **location 4**, choose **Display heater out**.
5. Click **Control setup**, choose **selected for loop 1**, **control with Input A**, **SP units Temp C**, **Control mode open**, **power up enable**, **setpoint Ramp on**, **Ramp rate 100 K/m**, and **heater load 50 Ω**.
6. Click **Interface**, choose **Baud 960**, **IEEE Address 12**, and **IEEE Term Cr Lf**.
7. Click **Zone setting**, for loop 1, choose **Zone 01**, **SP limit 0.000K**, **Prop (P) 50.00**, **Inteq (I) 20.000**, **Drive (D) 0.00%**.
8. If you want to turn off the heater during the experiment, click "heater off".

APPENDIX C: SUPPLEMENTAL INFORMATION FOR THERMO-RESPONSIVE BEHAVIOR OF LINEAR COPOLYPEPTOID NANOSTRUCTURES INVESTIGATED WITH ATOMIC FORCE MICROSCOPY

1. Preparation of Nanopores within a Film of Octadecyltrichlorosilane (OTS)

Particle lithography was used to generate organosilane nanopatterns on Si(111) surfaces. The silicon substrates were cleaned by immersion in piranha solution for 1.5 h. Piranha solution, which is a mixture of sulfuric acid and hydrogen peroxide at a ratio of 3:1 (v/v), is highly corrosive and should be handled cautiously. Substrates were then rinsed copiously with deionized water and dried under argon. Monodisperse silica mesospheres (500 nm diameter) were washed with water for three times by centrifugation to remove trace charge stabilizers or surfactants. The pellet of silica mesospheres was resuspended in water by vortex mixing, and a drop (10 μL) was deposited on a clean substrate. The sample was dried in air for 2 h to produce surface masks for further chemical steps. As water evaporated during the drying step, capillary forces pull the mesospheres together to form crystalline layers on flat surface. Next, the substrate was placed in an oven at 140 C for 24 h to temporarily anneal the mesospheres to the surface. After cooling, the sample was immersed in a 0.1% solution of OTS (v/v) in toluene for 5 h. Next the sample was rinsed with water and ethanol. To remove the mesoparticles, the substrate was sonicated for 15 min in ethanol and water successively. The sample was dried under argon and characterized by atomic force microscopy (AFM) with contact-mode in ambient air (Figure C1).

The hexagonal arrangement of the nanopores can be clearly seen in the 10×10 μm^2 topography (Figure C1 a) and lateral force (Figure C1 b) images. The shapes of the nanopores are more discernible is the zoom-in view (Figure C1 c). The chemistry difference of methyl terminated silane and the bare Si substrate is distinguishable in the lateral force image (Figure C1 d). The

depth of the nanopores is ~1.6 nm measured with the cursor profile (Figure C1 e) over 2 nanopores in the zoom-in area (Figure C1 c).

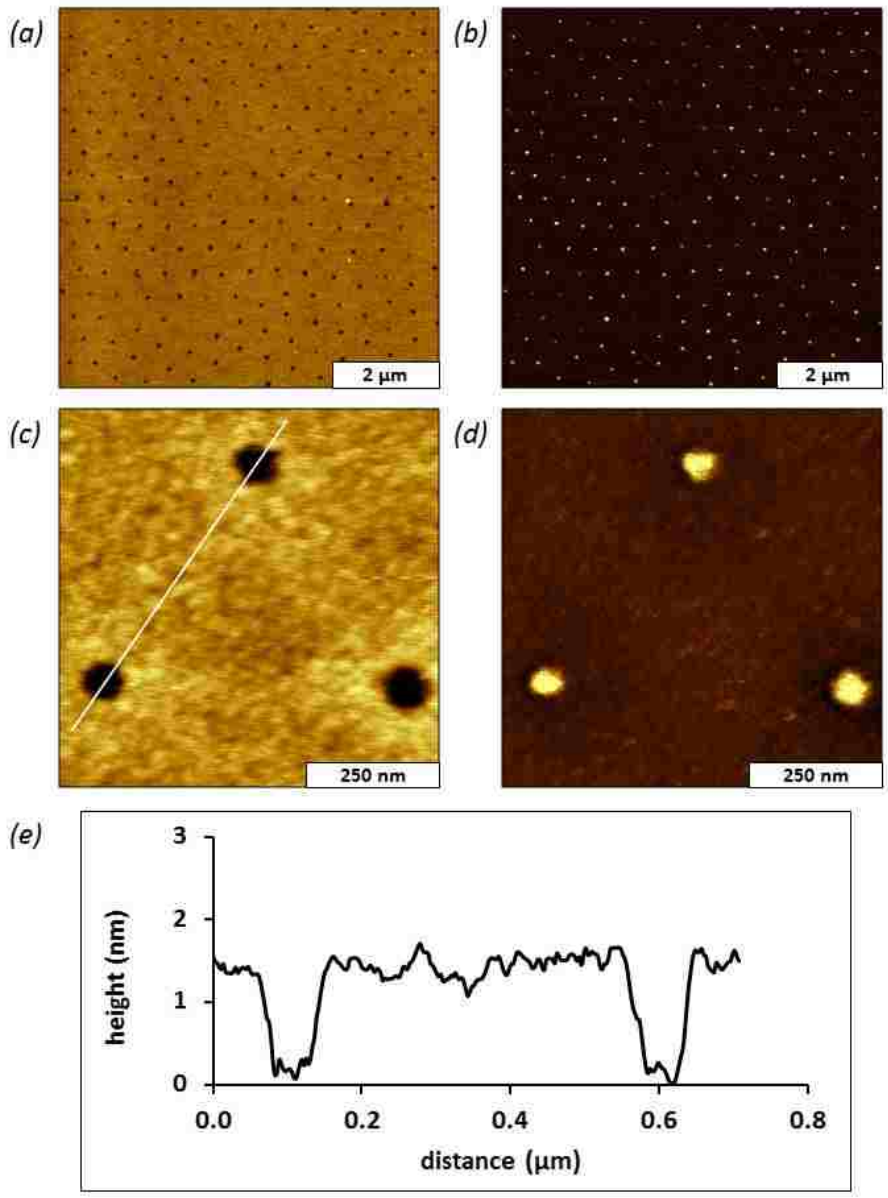

Figure C1 Nanopore patterns within a thin film of OTS acquired by contact-mode AFM. (a) 10 μm^2 topography view. (b) Corresponding lateral force image of a. (c) Zoom-in topograph of a. (d) Simultaneously acquired lateral force image of c. (e) Height profile for the line in c.

2. Thermo-responsiveness Study of Height Changes of Two Polypeptoid Brush Sites

The height changes of polypeptoid brushes are shown in Figure 4.4 at three selected temperatures. The height tracking over two exact same sites under selected temperatures are shown in Figure C2.

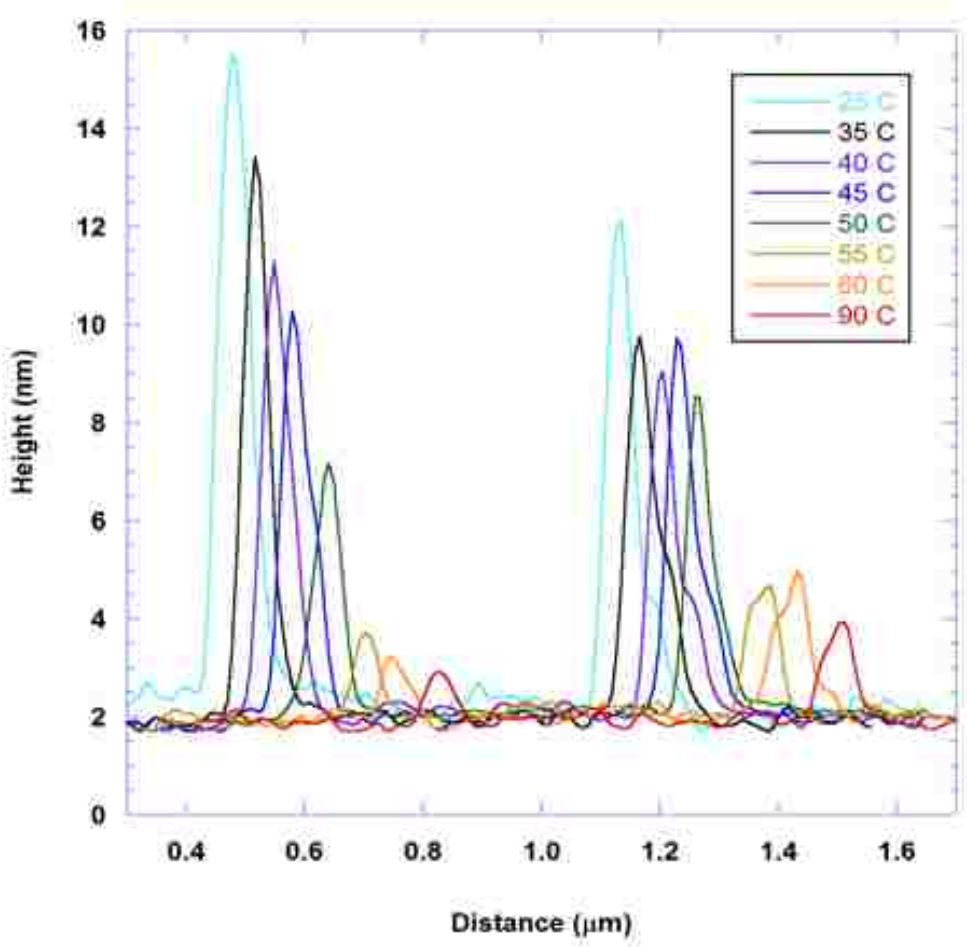

Figure C2 *In situ* temperature study of height changes of two copolypeptoid brush sites. Heights of both sites decreased from 25 C to 90 C.

3. Cloud Point Temperature (T_{cp}) Measurement with Turbidity Assay

Copolypeptoid poly[(*N*-ethyl glycine)$_{32}$-*r*-(*N*-butyl glycine$_{17}$)], or P(NEG$_{32}$-*r*-NBG$_{17}$), was dissolved in distilled water at room temperature. This aqueous solution was then transferred to a vitro-dynamic cell which was sealed at both ends. The Vitrocom cell walls were 1.0 mm in thickness. The polymer solution was then placed in a Mettler heating stage, from which the control of the temperature ramp could be accessed using controller Mettler Fp 80 central processing unit. The heating rate was 1 C/min. An Olympus optical microscope was used to collect the transmittance through the sample on the Mettler heating stage and the intensity was collected by a Mettler photomonitor. This process has been outlined in the Mettler handbook. After transmittance normalization, the onset cloud point temperature (T_{cp}) was determined to be the temperature at 90% transmittance. The measured onset T_{cp} is 45 C in our experiment (Figure C3). The transition window ΔT is 28 C (68 C – 40 C).

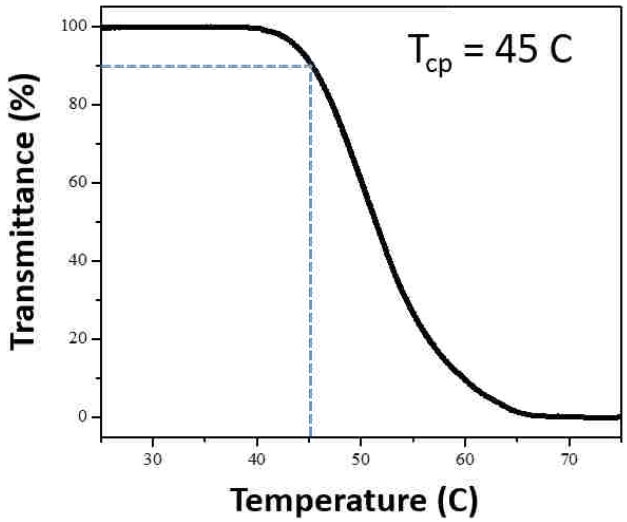

Figure C3 The LCST behavior of the copolypeptoid studied with the turbidity assay collected from the untethered copolymer in aqueous solution. The cloud point temperature (T_{cp}) measured at 50% transmittance is 51.4 C for the copolypeptoid P(NEG$_{32}$-*r*-NBG$_{17}$).

4. ^{1}H NMR Characterization

^{1}H NMR spectrum (Figure C4) was recorded on a Bruker DPX-400 spectrometer, and the chemical shifts in parts per million (ppm) were referenced relative to CD_2Cl_2.

The molar percents of the *N*-ethyl glycine and *N*-butyl glycine were confirmed via the comparative integration of the methyl peak from PNEG (1.2 ppm) and PNBG (0.9 ppm) to the benzyl peaks from the initiator (7.0 ppm).

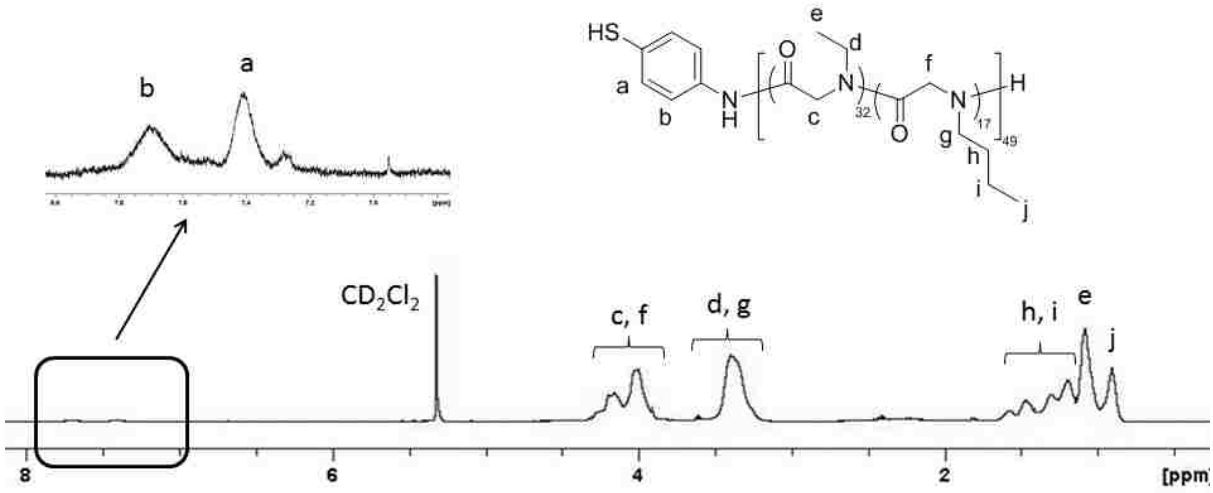

Figure C4 The 400MHz ^{1}H NMR spectrum of copolypeptoid P(NEG_{32}-*r*-NBG_{17}) in CD_2Cl_2.

5. Size Exclusive Chromatography (SEC)

An Agilent 1200 SEC was used to acquire the polymer molecular weight (Mw) and polydispersity index (PDI). A solution of DMF containing 0.1 M LiBr was used as the eluent at a flow rate of 0.5 mL· min^{-1}. All data analyses were performed using Wyatt Astra v5.3 software. The Mw is 14.5 kDa and the PDI is 1.24 by using polystyrene standards (molecular weight Mn = 590 g·mol^{-1} – 1472 kg·mol^{-1}, Polymer Laboratories, Inc.)

APPENDIX D: SUPPLEMENTAL INFORMATION FOR SAMPLE STAGE DESIGNED FOR FORCE MODULATION MICROSCOPY USING A TIP-MOUNTED AFM SCANNER

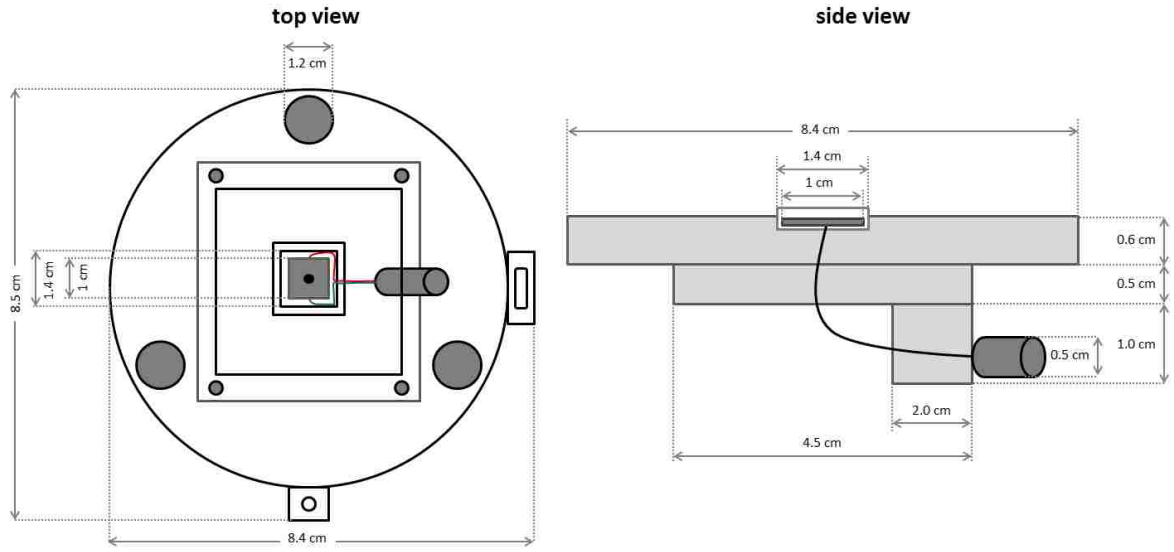

Figure D1 Physical dimensions of the force modulation sample stage. At the center of the stage, a square (1×1 cm^2) piezoactuator is located underneath a polycarbonate plate (1.4×1.4 cm^2). There is a small air gap surrounding and between the polycarbonate pieces and the sample stage so that only the central area is driven to vibrate.

Figure D2 Steps for making nanopores within a thin film of OTS prepared by particle lithography combined with solution immersion.[243] A drop of an aqueous suspension of silica mesospheres in water (10 μL) was deposited on a clean Si(111) substrate. The sample was dried in air for 2 h to produce surface masks. As water evaporated during the drying step, capillary forces pull the mesospheres together to form crystalline layers on flat surfaces. The substrate was placed in an oven at 140 C overnight to temporarily anneal the mesospheres to the surface. After cooling, the sample was immersed in a 0.1% solution (v/v) of OTS in toluene for 5 h to form an OTS film surrounding the surface mask. To remove the mesoparticles, the substrate was sonicated for 15 min in ethanol and water successively. The sample was dried under argon before characterization with FMM-AFM.

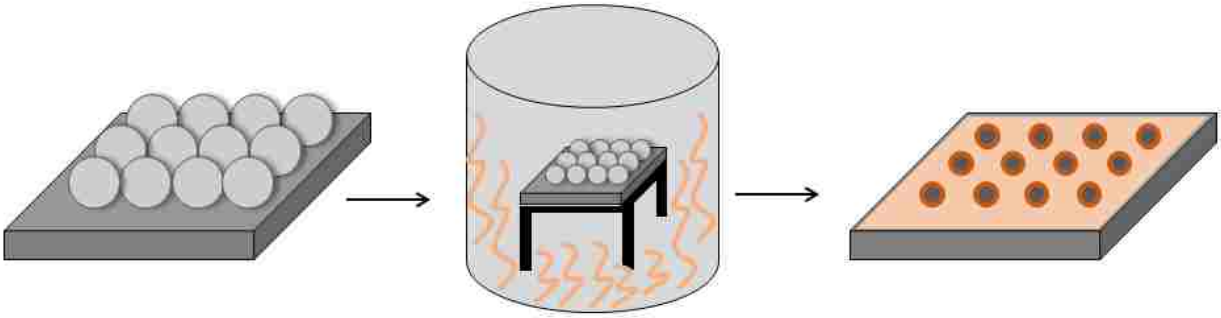

Figure D3 Basic steps to prepare nanorings of PEG-silane using particle lithography combined with heated vapor deposition.[242] A drop of a suspension of 500 nm latex mesospheres (10 μL) in water was deposited on a clean Si(111) substrate. The sample was dried in air for 5 h to produce surface masks. Next, the sample was placed in a vessel containing 300 μL neat PEG-silane. The sealed container was placed in an oven (70 C) overnight. Vapor-phase PEG-silane will attach to the Si substrate except in places where the mesosphere mask has protected the substrate. After cooling, the sample was rinsed with water and ethanol. To remove the mesoparticles, the substrate was sonicated for 15 min in ethanol, toluene, and water successively. The sample was dried under argon before characterization with FMM-AFM.

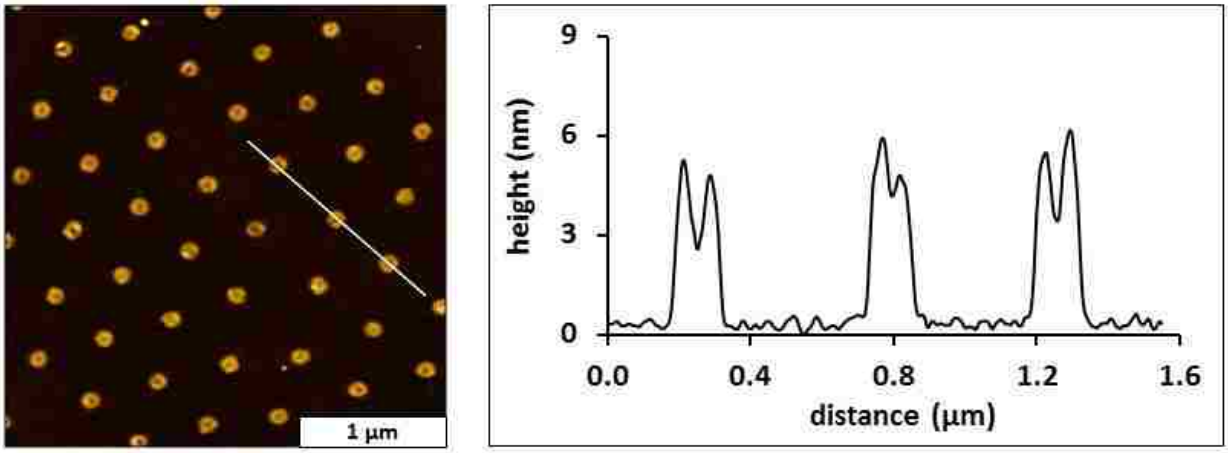

Figure D4 Height measurements of nanorings of PEG-silane. (Left) View of PEG-silane nanorings revealed with a topography frame; (Right) Height profile for the white line drawn across three nanorings.

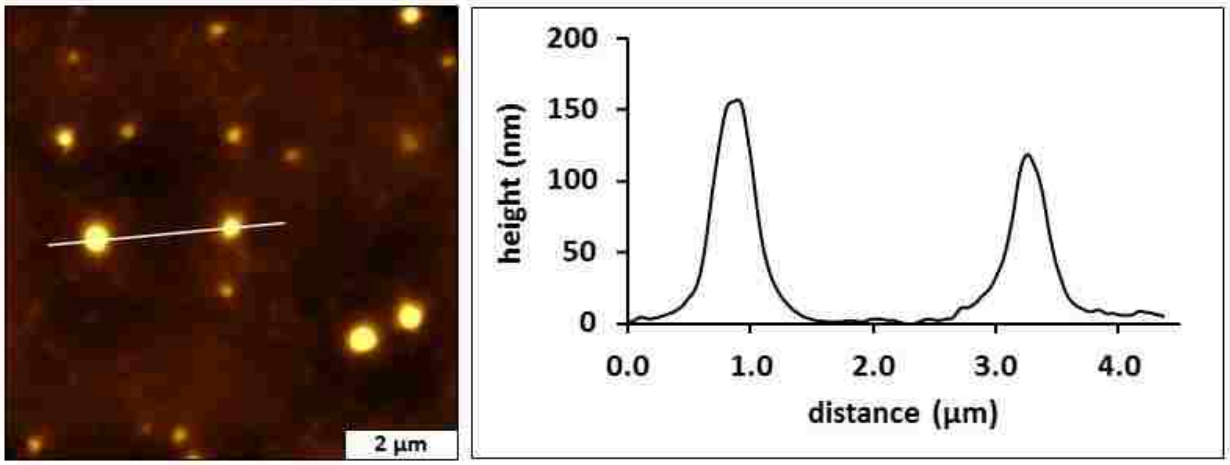

Figure D5 Example height measurements of selected aggregates of the polymer gel. (Left) View of the polymer gel sample disclosed with a topography frame; (Right) Height profile for the white line drawn across an area of the nanoclusters.

APPENDIX E: SUPPLEMENTAL INFORMATION FOR DIRECT COMPARISON OF SAMPLE ACTUATION VERSUS TIP VIBRATION CONFIGURATION FOR FORCE MODULATION AFM

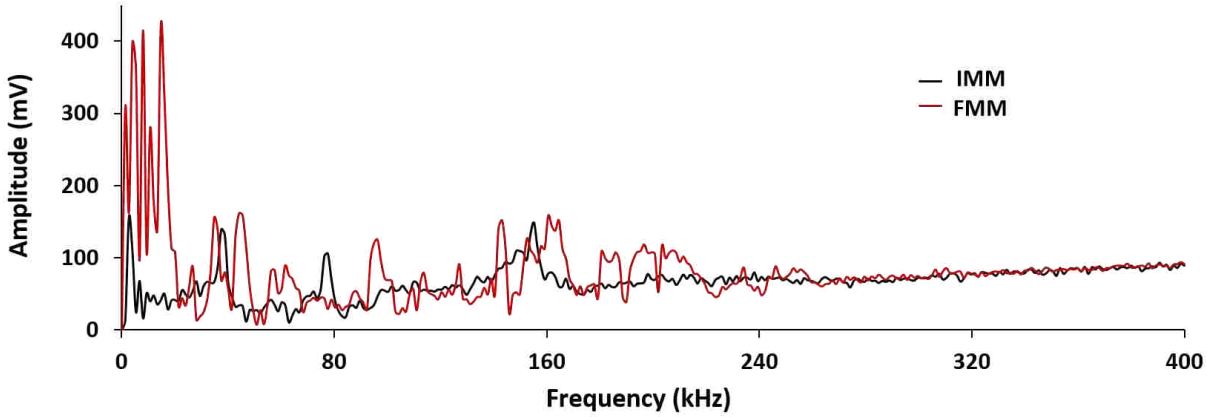

Figure E1 Overlay of the Frequency sweeps of FMM and IMM.

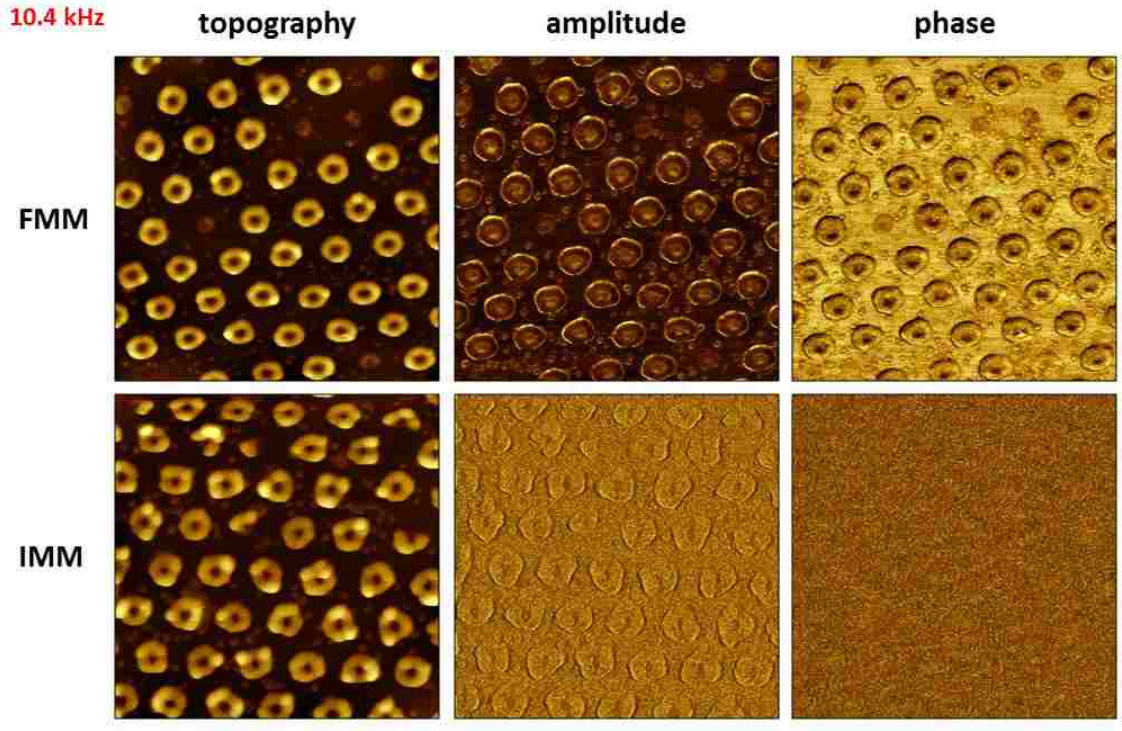

Figure E2 Comparison of stage-driven FMM and tip-driven IMM of CMPS nanorings at frequency 10.4 kHz. Image sizes are 3×3 μm^2.

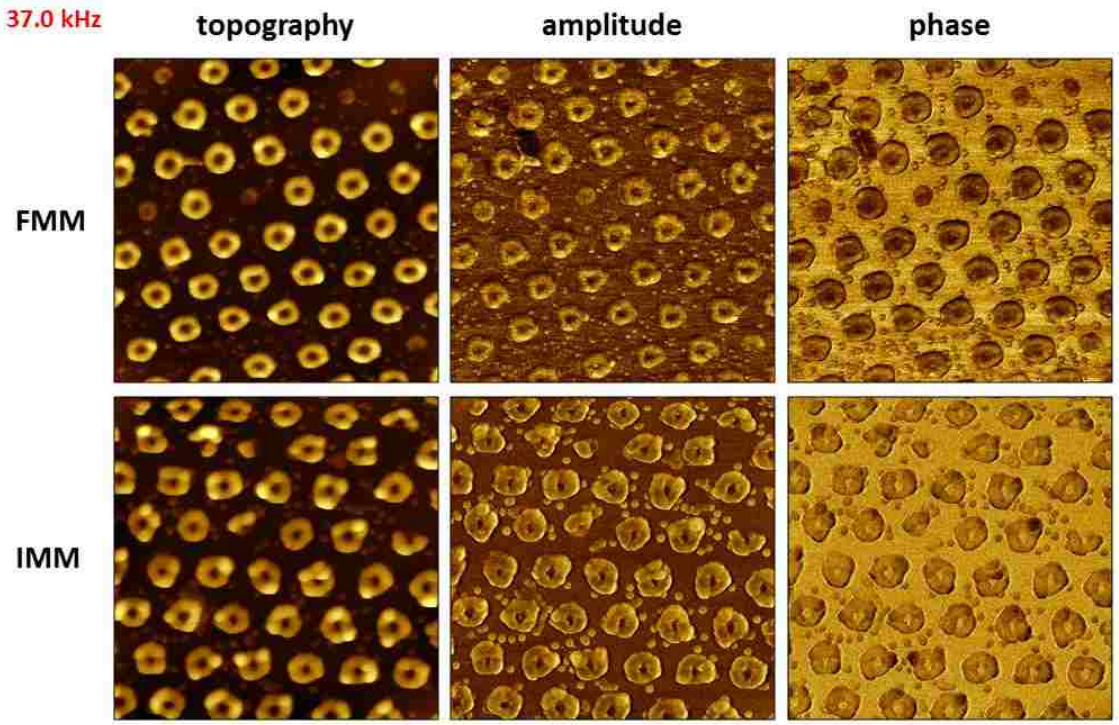

Figure E3 Comparison of stage-driven FMM and tip-driven IMM of CMPS nanorings at frequency 37.0 kHz. Image sizes are 3 × 3 μm^2.

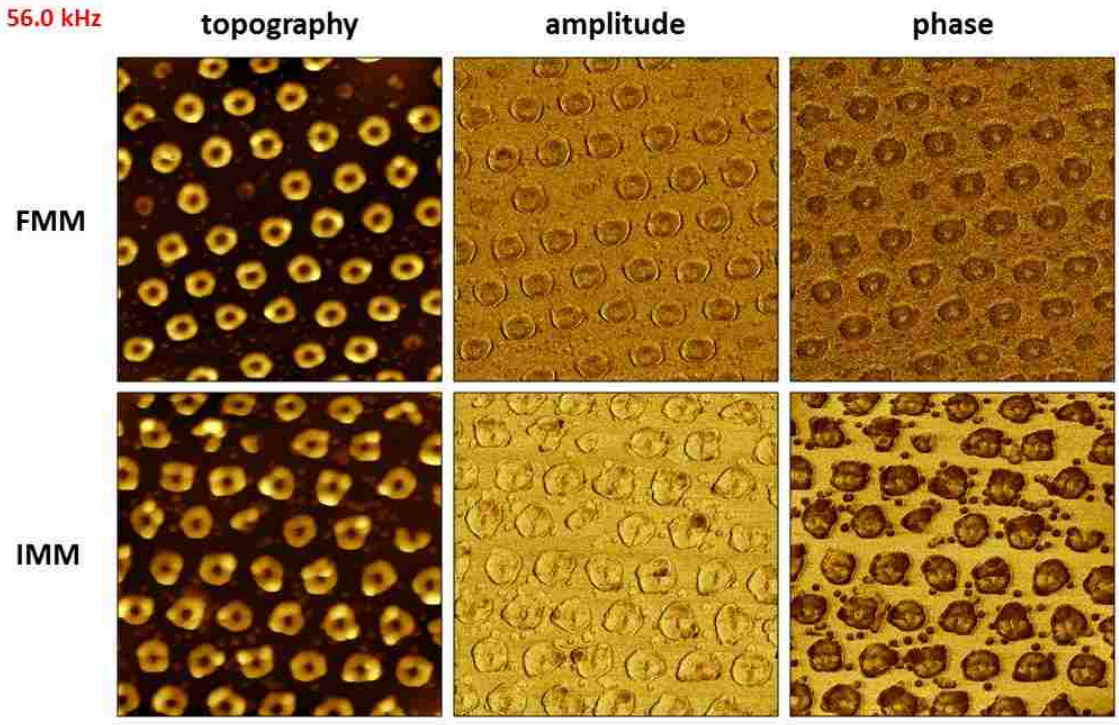

Figure E4 Comparison of stage-driven FMM and tip-driven IMM of CMPS nanorings at frequency 56.0 kHz. Image sizes are 3 × 3 μm^2.

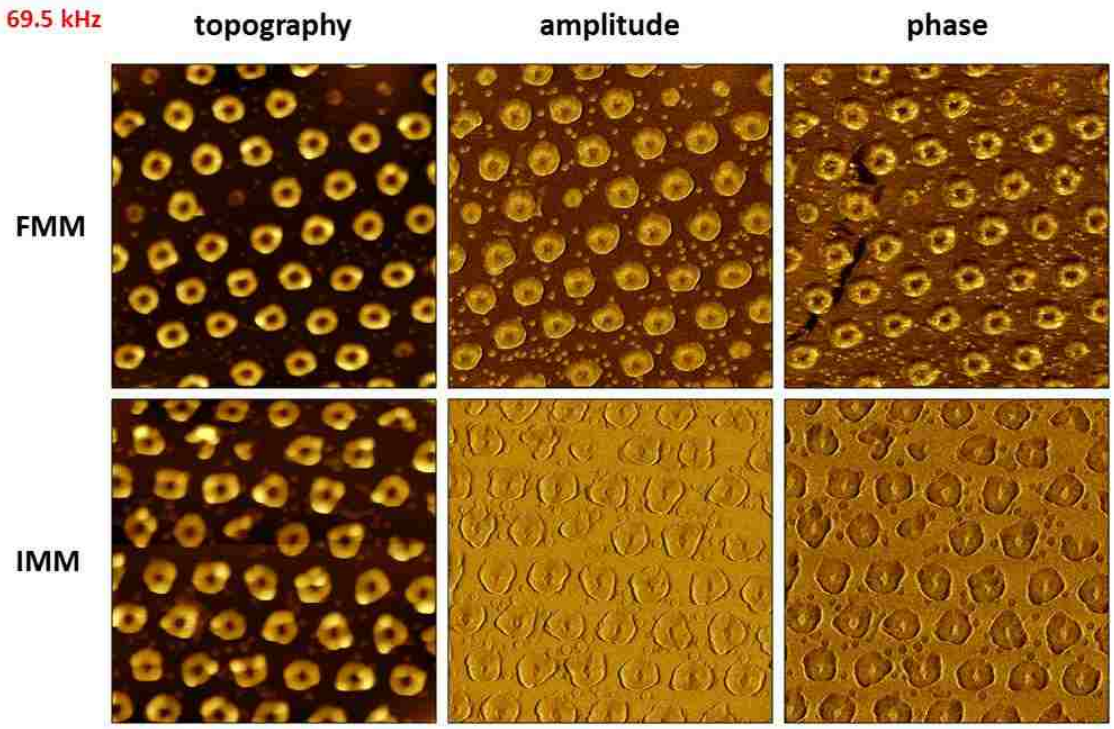

Figure E5 Comparison of stage-driven FMM and tip-driven IMM of CMPS nanorings at frequency 69.5 kHz. Image sizes are 3 × 3 μm^2.

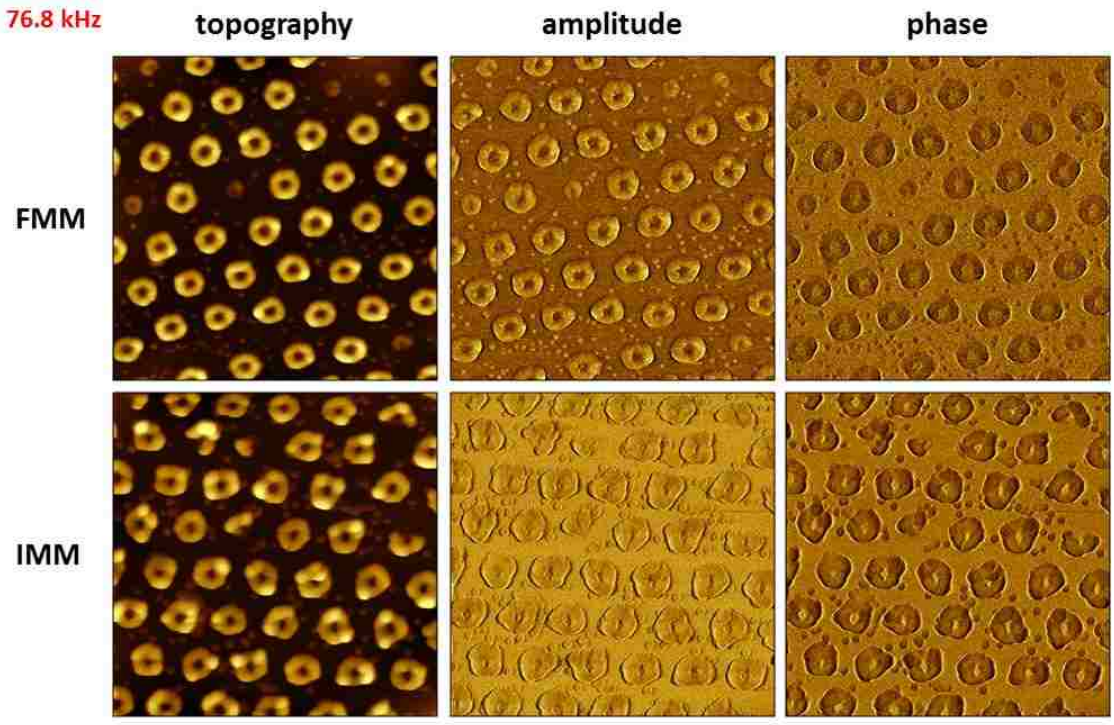

Figure E6 Comparison of stage-driven FMM and tip-driven IMM of CMPS nanorings at frequency 76.8 kHz. Image sizes are 3 × 3 μm^2.

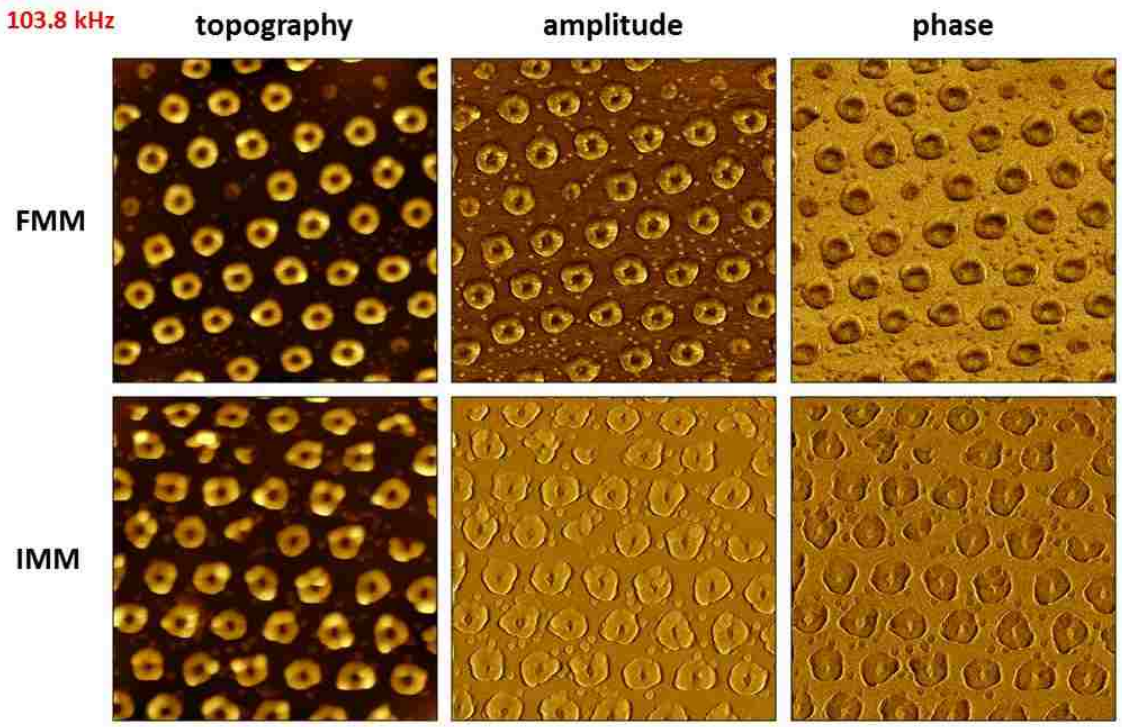

Figure E7 Comparison of stage-driven FMM and tip-driven IMM of CMPS nanorings at frequency 103.8 kHz. Image sizes are 3 × 3 μm^2.

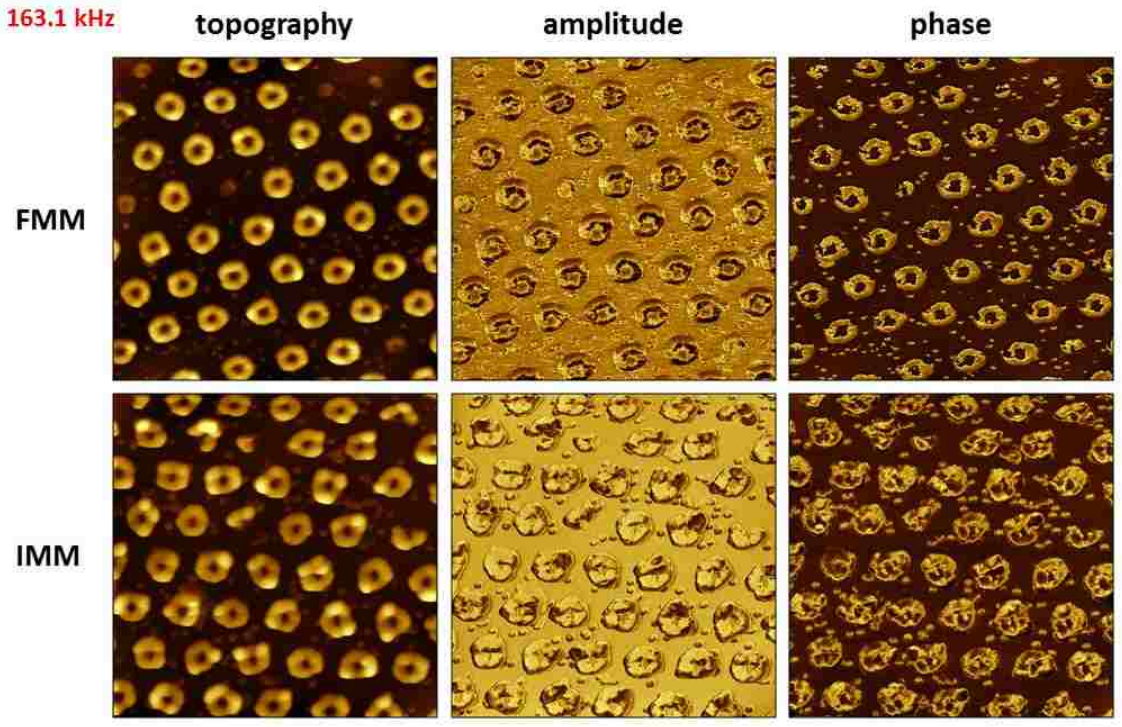

Figure E8 Comparison of stage-driven FMM and tip-driven IMM of CMPS nanorings at frequency 163.1 kHz. Image sizes are 3 × 3 μm^2.

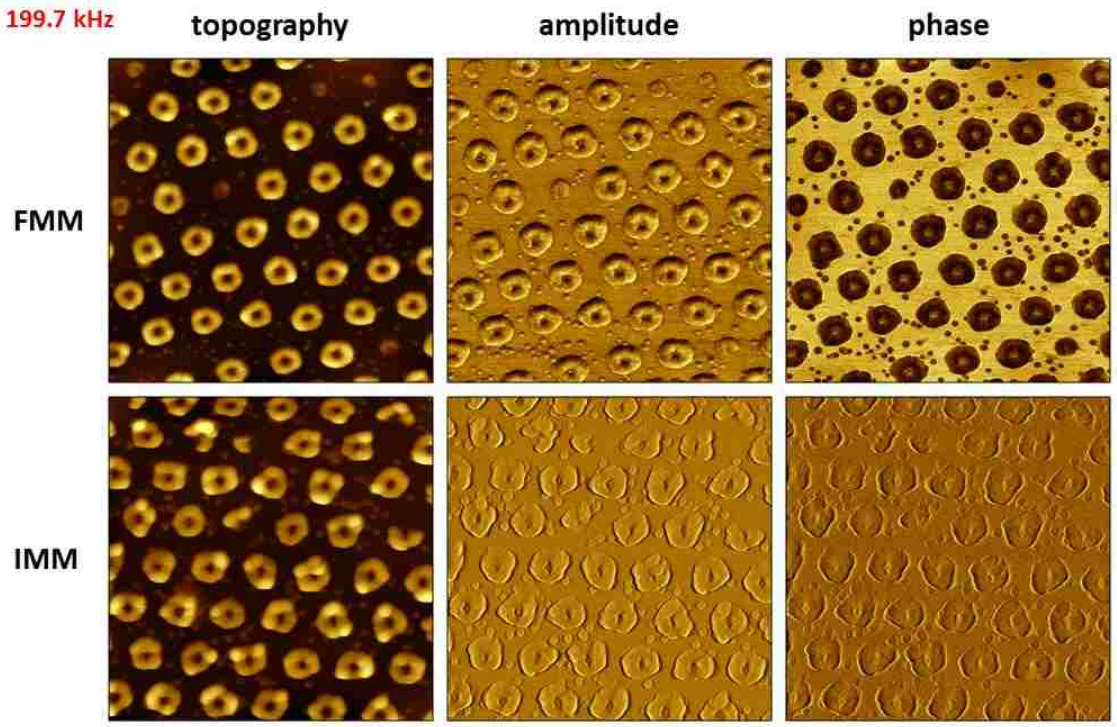

Figure E9 Comparison of stage-driven FMM and tip-driven IMM of CMPS nanorings at frequency 199.7 kHz. Image sizes are 3×3 μm^2.

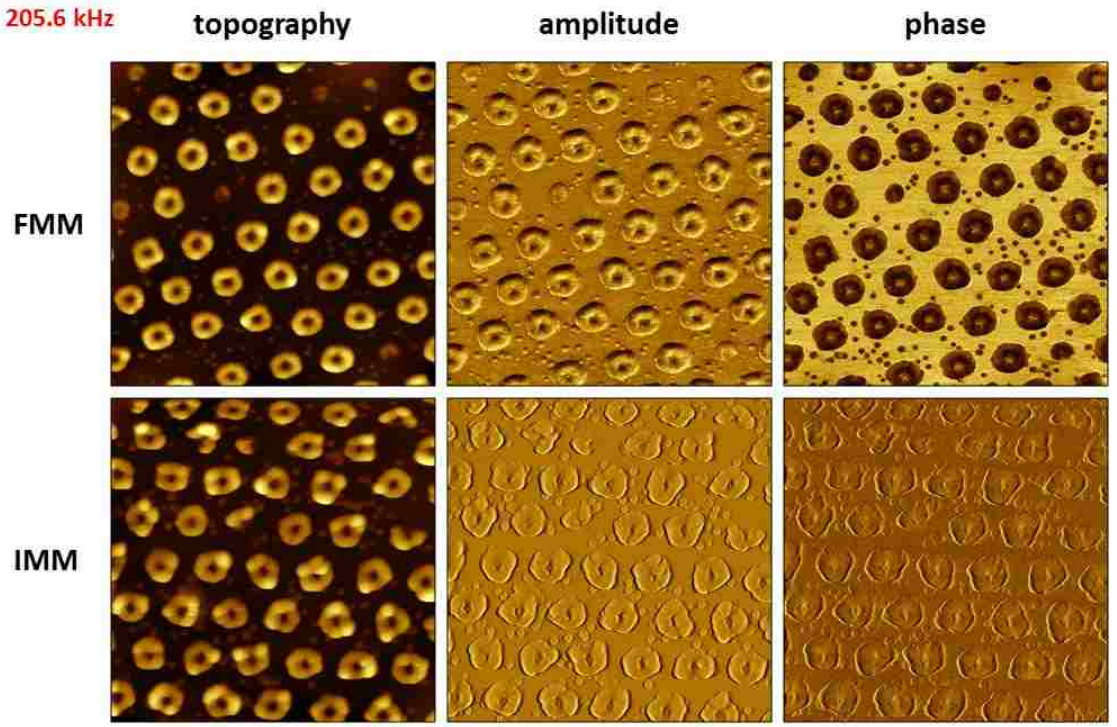

Figure E10 Comparison of stage-driven FMM and tip-driven IMM of CMPS nanorings at frequency 205.6 kHz. Image sizes are 3×3 μm^2.

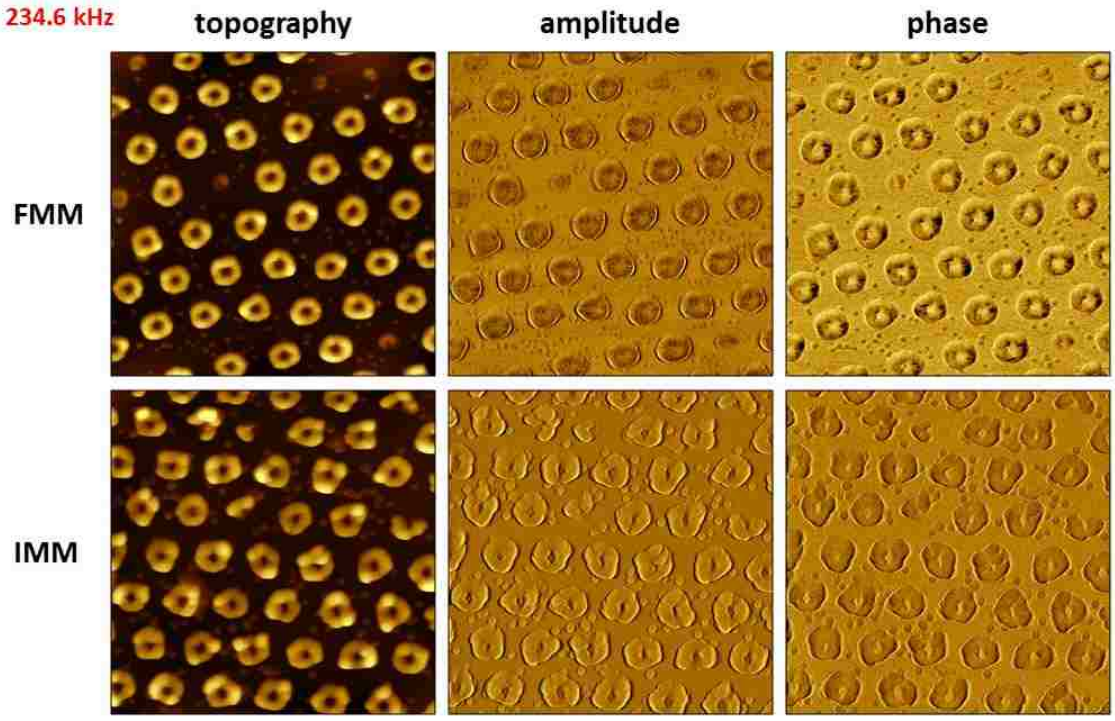

Figure E11 Comparison of stage-driven FMM and tip-driven IMM of CMPS nanorings at frequency 76.8 kHz. Image sizes are 3 × 3 μm^2.

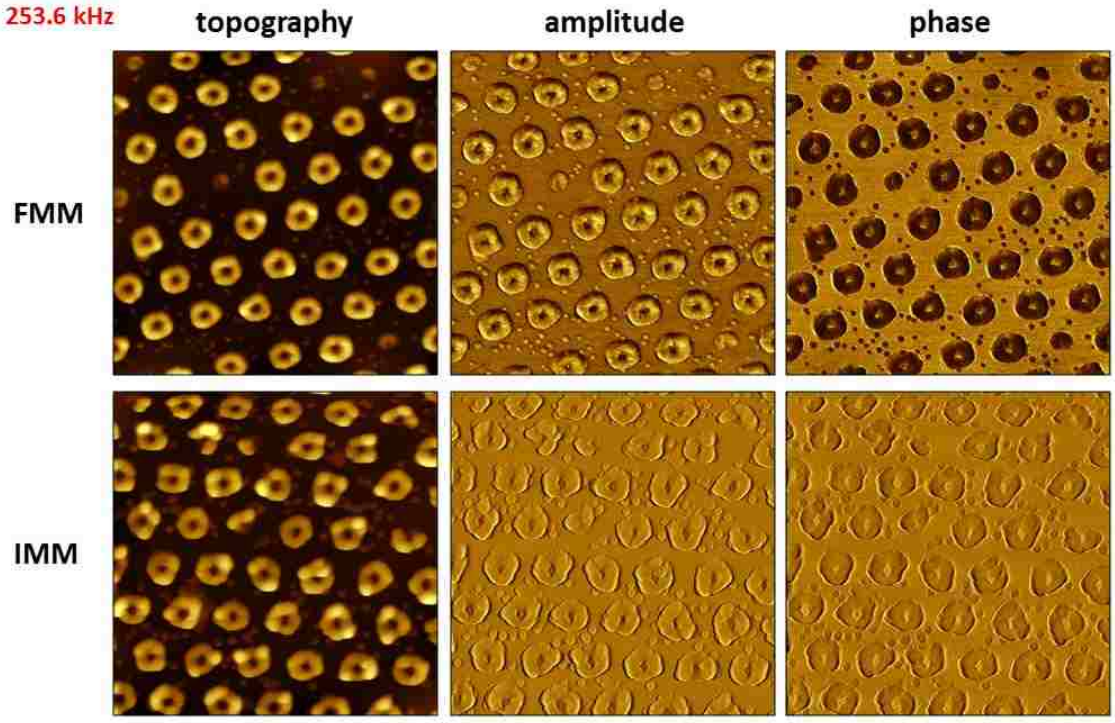

Figure E12 Comparison of stage-driven FMM and tip-driven IMM of CMPS nanorings at frequency 253.6 kHz. Image sizes are 3 × 3 μm^2.

APPENDIX F: IMAGING POLYSTYRENE LATEX MESOSPHERES USING AFM

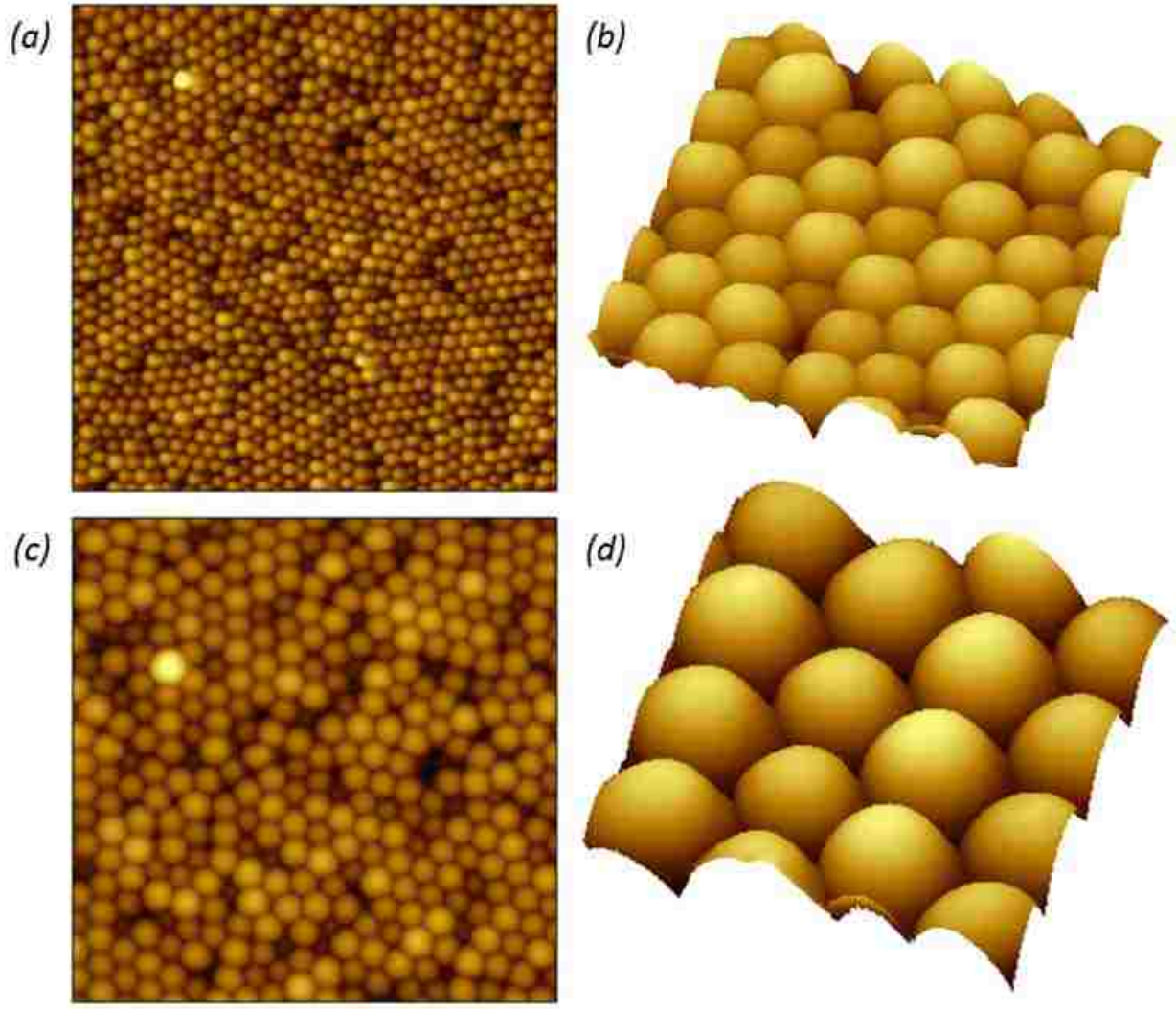

Figure F1 The surface organization of polystyrene latex mesospheres on mica(0001) imaged with tapping mode AFM. (a) Topography view of 300 nm latex, 10 ×10μm^2; (b) topography view of 300 nm latex, 2 ×2 μm^2; (c) topograph of 300 nm latex, 6 × 6 μm^2; (d) view of 500 nm latex, 2 × 2 μm^2.

APPENDIX F: PERMISSIONS

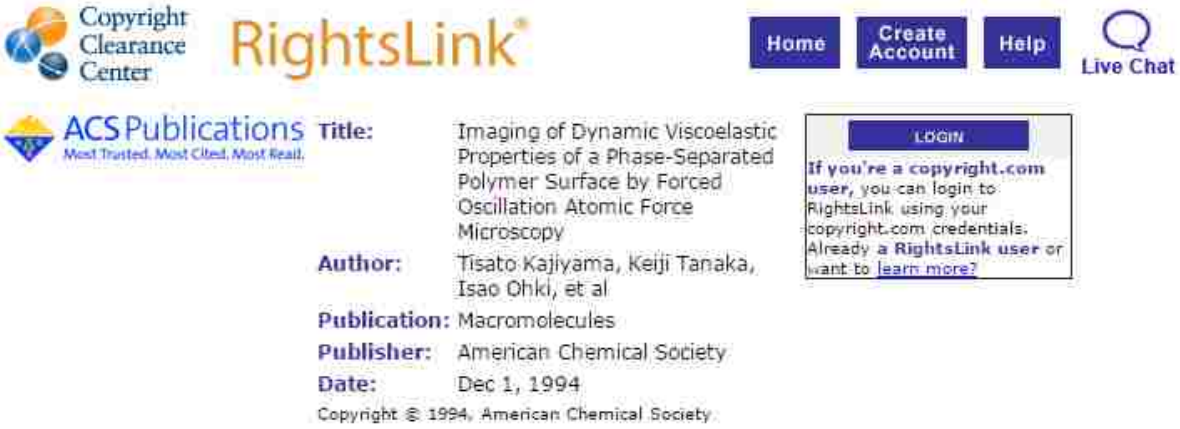

Copyright Clearance Center RightsLink®

Home | Create Account | Help | Live Chat

ACS Publications
Most Trusted. Most Cited. Most Read.

Title: Imaging of Dynamic Viscoelastic Properties of a Phase-Separated Polymer Surface by Forced Oscillation Atomic Force Microscopy

Author: Tisato Kajiyama, Keiji Tanaka, Isao Ohki, et al

Publication: Macromolecules

Publisher: American Chemical Society

Date: Dec 1, 1994

Copyright © 1994, American Chemical Society

LOGIN

If you're a copyright.com user, you can login to RightsLink using your copyright.com credentials. Already a RightsLink user or want to learn more?

PERMISSION/LICENSE IS GRANTED FOR YOUR ORDER AT NO CHARGE

This type of permission/license, instead of the standard Terms & Conditions, is sent to you because no fee is being charged for your order. Please note the following:

- Permission is granted for your request in both print and electronic formats, and translations.
- If figures and/or tables were requested, they may be adapted or used in part.
- Please print this page for your records and send a copy of it to your publisher/graduate school.
- Appropriate credit for the requested material should be given as follows: "Reprinted (adapted) with permission from (COMPLETE REFERENCE CITATION). Copyright (YEAR) American Chemical Society." Insert appropriate information in place of the capitalized words.
- One-time permission is granted only for the use specified in your request. No additional uses are granted (such as derivative works or other editions). For any other uses, please submit a new request.

If credit is given to another source for the material you requested, permission must be obtained from that source.

BACK | CLOSE WINDOW

Copyright © 2015 Copyright Clearance Center, Inc. All Rights Reserved. Privacy statement. Terms and Conditions.
Comments? We would like to hear from you. E-mail us at customercare@copyright.com

Title: Imaging Nanoscopic Elasticity of Thin Film Materials by Atomic Force Microscopy: Effects of Force Modulation Frequency and Amplitude

Author: J. S. Jourdan, S. J. Cruchon-Dupeyrat, Y. Huan, et al

Publication: Langmuir

Publisher: American Chemical Society

Date: Sep 1, 1999

PERMISSION/LICENSE IS GRANTED FOR YOUR ORDER AT NO CHARGE

This type of permission/license, instead of the standard Terms & Conditions, is sent to you because no fee is being charged for your order. Please note the following:

- Permission is granted for your request in both print and electronic formats, and translations.
- If figures and/or tables were requested, they may be adapted or used in part.
- Please print this page for your records and send a copy of it to your publisher/graduate school.
- Appropriate credit for the requested material should be given as follows: "Reprinted (adapted) with permission from (COMPLETE REFERENCE CITATION). Copyright (YEAR) American Chemical Society." Insert appropriate information in place of the capitalized words.
- One-time permission is granted only for the use specified in your request. No additional uses are granted (such as derivative works or other editions). For any other uses, please submit a new request.

If credit is given to another source for the material you requested, permission must be obtained from that source.

BACK | CLOSE WINDOW

Title:	Local modification of elastic properties of polystyrene–polyethyleneoxide blend surfaces
Author:	H.-Y. Nie,M. Motomatsu,W. Mizutani, et al.
Publication:	Journal of Vacuum Science & Technology B
Volume/Issue	13/3
Publisher:	AIP Publishing LLC
Date:	May 1, 1995
Page Count:	4

Order Completed

Thank you very much for your order.

Click here for Payment Terms and Conditions.

Get a printable version for your records.

License Number	3660661335083
Order Date	Jul 02, 2015
Publisher	AIP Publishing LLC
Publication	Journal of Vacuum Science & Technology B
Article Title	Local modification of elastic properties of polystyrene–polyethyleneoxide blend surfaces
Author	H.-Y. Nie,M. Motomatsu,W. Mizutani, et al.
Online Publication Date	May 1, 1995
Volume number	13
Issue number	3
Type of Use	Thesis/Dissertation
Requestor type	University or Educational Institution
Format	Print and electronic
Portion	Figure/Table
Number of figures/tables	1
Title of your thesis / dissertation	SCANNING PROBE INVESTIGATIONS OF NANOPATTERNED AND THERMO-RESPONSIVE POLYPEPTOIDS AND THE INVENTION OF A NEW SAMPLE STAGE FOR FORCE MODULATION MICROSCOPY
Expected completion date	Aug 2015
Estimated size (number of pages)	150
Total	0.00 USD

ORDER MORE... CLOSE WINDOW

Title:	Formation of Three-Dimensional Protein-Lipid Aggregates in Monolayer Films Induced by Surfactant Protein B
Author:	Silke Krol,Michaela Ross,Manfred Sieber,Stephanie Künneke,Hans-Joachim Galla,Andreas Janshoff
Publication:	Biophysical Journal
Publisher:	Elsevier
Date:	August 2000

Order Completed

Thank you very much for your order.

This is a License Agreement between Lu Lu ("You") and Elsevier ("Elsevier"). The license consists of your order details, the terms and conditions provided by Elsevier, and the payment terms and conditions.

Get the printable license.

License Number	3660870096808
License date	Jul 02, 2015
Licensed content publisher	Elsevier
Licensed content publication	Biophysical Journal
Licensed content title	Formation of Three-Dimensional Protein-Lipid Aggregates in Monolayer Films Induced by Surfactant Protein B
Licensed content author	Silke Krol,Michaela Ross,Manfred Sieber,Stephanie Künneke,Hans-Joachim Galla,Andreas Janshoff
Licensed content date	August 2000
Licensed content volume number	79
Licensed content issue number	2
Number of pages	15
Type of Use	reuse in a thesis/dissertation
Portion	figures/tables/illustrations
Number of figures/tables/illustrations	1
Format	both print and electronic
Are you the author of this Elsevier article?	No
Will you be translating?	No
Original figure numbers	figure 9
Title of your thesis/dissertation	SCANNING PROBE INVESTIGATIONS OF NANOPATTERNED AND THERMO-RESPONSIVE POLYPEPTOIDS AND THE INVENTION OF A NEW SAMPLE STAGE FOR FORCE MODULATION MICROSCOPY
Expected completion date	Aug 2015
Estimated size (number of pages)	150
Elsevier VAT number	GB 494 6272 12
Permissions price	0.00 USD
VAT/Local Sales Tax	0.00 USD / 0.00 GBP
Total	0.00 USD

ORDER MORE... CLOSE WINDOW

VITA

Lu Lu was born and grew up in Lanzhou, China. She earned her Bachelor of Science degree in polymer science and engineering department from University of Science and Technology (USTC) of China in 2010. During her time in USTC, she participated in undergraduate research under Dr. Ruke Bai for a year and published a co-authored journal article. She joined Chemistry department at Louisiana State University (LSU) in the Fall of 2010. She is a Ph.D candidate in the fields of analytical and macromolecular chemistry under the supervision of Dr. Jayne C. Garno and Dr. Donghui Zhang. Her research interests include: preparing patterns of polymer brushes on surfaces, studying the thermo-responsive properties of patterned polymer nanobrushes using atomic force microscopy (AFM) and developing sample stage accessories with AFM for force modulation microscopy studies. Thus far at LSU, Lu submitted one first author journal articles and published five collaborative research papers. She had four more first author and several shared manuscripts which are under preparation. Lu presented her research at both regional and national conferences including one talk, five first-author posters and four co-authored posters. Lu also gave a talk in the workshop held by Keysight Technologies at LSU. Lu directed senior thesis research for an undergraduate student at LSU, whose name is Rasheda Gros. Rasheda won a poster award in 2014 Annual Biomedical Research Conference for Minority Students (ABRCMS) for her studies with AFM investigations of nanopatterns prepared with organosilane and nanoparticles.